PhD Thesis

Data analysis, simulations, and reconstruction of antiproton annihilations in a silicon pixel detector

Helga Holmestad

Department of Physics
University of Oslo
June 2018

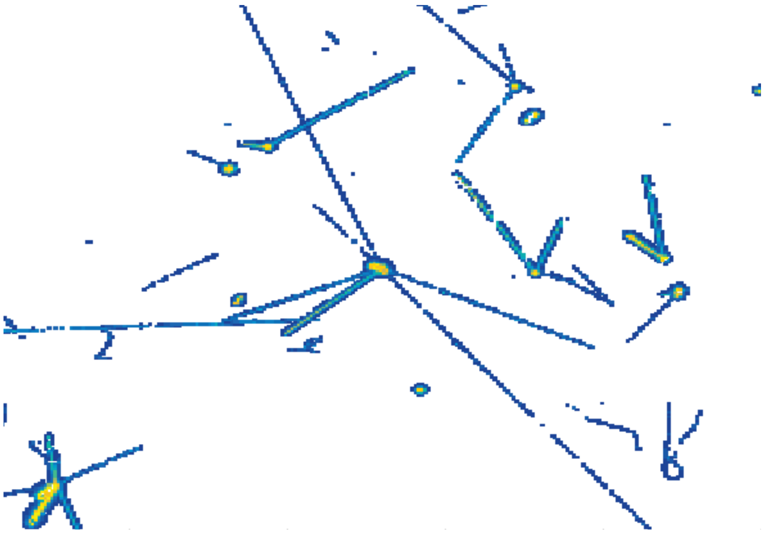

Series of dissertations submitted to the
Faculty of Mathematics and Natural Sciences, University of Oslo
No. 2026

ISSN 1501-7710

Cover: Hanne Baadsgaard Utigard.
Print production: Reprosentralen, University of Oslo.

Abstract

There are strong theoretical arguments in favor of the gravitational acceleration being identical for matter and antimatter, as anything else would violate the weak equivalence principle. The weak equivalence principle is the cornerstone of general relativity, and today there are no experiments contradicting it. However, it has never been experimentally verified that the gravitational acceleration of matter and antimatter is indeed identical.

The AEgIS experiment at CERN aims at measuring the gravitational acceleration of antimatter to a precision of 1% by determining the fall of antihydrogen over the length of around 1 m. The proposed method will make use of a position sensitive detector to measure the annihilation point of antihydrogen. Such a detector must be able to tag an antihydrogen atom, measure its time of arrival, and reconstruct its annihilation point with high precision in the vertical direction.

This thesis presents a detector response model for antiproton annihilations in a silicon detector equipped with the Timepix3 readout, in order to evaluate the possibility of using such a detector in the AEgIS experiment. Antiprotons from the Antiproton Decelerator at CERN were used to obtain data of direct annihilations on the surface of a Timepix3 detector. These data were used to develop and verify the detector response model. The work presented here includes all steps from data collection, simulation, and verification of the simulation. Clear tagging criteria for annihilation clusters were found, and a tagging efficiency of 50 ± 10 % is achieved. By using the annihilation products to reconstruct the annihilation point a position resolution of 22 µm is achieved on a subset of the annihilation clusters.

This thesis also includes a full simulation of the GRACE beam line that was build to improve the experimental conditions for testing detectors. The GRACE beamline can select out only the low energy antiprotons and direct them towards the detector. The simulation of the GRACE beamline evaluates the flux and energy of the antiprotons, and in most cases reproduced the energy distribution and flux within ± 30 %.

Acknowledgments

During the work with this thesis I got help and support from many people. First I would like to thank my three great supervisors; Heidi Sandaker, Steinar Stapnes, and Ole Røhne. I want to thank Heidi for giving me lot of support in my day to day work. Thank you also for reading numerous drafts of the main article and all chapters of my thesis. I appreciate how you always tried to misunderstand what I wrote, that forced me to present my work more clearly.

I want to thank Steinar for always being supportive and believing in me, even when there was no reason to do so. You also helped me maneuver through the bureaucratic mess that I sometimes got stuck in. I want to thank Ole for helping me solve some of the hardest problems I came across in the detector analysis.

At CERN I got to work with Nicola Pacifico and Angela Gligorova. I want to say thank you for all the work you did during test beam and your inputs to the analysis. Without your efforts there would be no data to analyse.

I got a lot of personal support from my two AEgIS colleagues; Lillian Smestad and Ingmari Tietje. Without you my time at CERN would definitely have been more difficult. I also want to thank Alex Read for always being willing to discuss my more or less sensible statistics questions[1]. I want to thank all my friends in Oslo for your moral support, and for always making time to meet me when I have been visiting Oslo.

At the end I want to give a very special thanks to my husband, Kyrre Ness Sjøbæk. Thank you for sharing your your knowledge of beam simulations when I unexpectedly had to set my feet in this area, your inputs to GRACE beam line simulations were very useful. Thank you for proofreading several chapters of my thesis, and for testing the technical documentation[2]. Thank you for always being supportive and helpful, and thank you for making my life so much better.

---

[1] Even after I ran away from being his student.

[2] This confirms that at least a highly competent physicist can get my programs to work.

Contents

Outline of the thesis

The AEgIS experiment at CERN aims at measuring the gravitational acceleration of antimatter, and for this measurement a position sensitive detector that can tag antiprotons and reconstruct their annihilation point is needed. The main topic of this thesis is to investigate the possibility of using a silicon pixel detectors for this purpose.

The first chapter gives the background and physics motivation for measuring the gravitational acceleration of antimatter. Chapter 2 introduces silicon pixel detectors, in particular the Timepix3 detector. Chapter 3 presents antiproton annihilation in theory, in simulations, and in detectors. Description and explanations of different detector effects peculiar to antiproton annihilations are also found in this chapter.

To improve the experimental conditions for detector tests the GRACE beam line was build. This beam line and the simulation of it is presented in chapter 4. Chapter 5 describes the analysis of antiproton data collected with the Timepix3 detector in the GRACE beam line, especially how the data was cleaned and the clusters characterized. Chapter 6 presents the detector response model, while chapter 7 uses the detector response model to investigate different methods of reconstructing the annihilation point.

In general this thesis also aims at demonstrating how the whole pipeline of a detector study of antiproton annihilations in a pixel detector can be carried out. All steps are included from the experimental setup, analyzing the data and then using data to develop and verify a detector response model. In the end the detector response model is used to investigate methods for reconstructing the annihilation point of antihydrogen. In order to make this work reproducible appendix A, B, C, and D contains technical documentation for all the software developed for this thesis.

The work of this thesis also includes three articles that are found in appendix E, F, and G. The first article is *Comparison of planar and 3D silicon pixel sensors used for detection of low energy antiprotons*. Here antiproton annihilations were studied in a 3D pixel detector. This was an ongoing project when I joined AEgIS, and my contribution was to do the simulation of the 3D pixel detector for this article. The second publication, *Study of antiproton annihilation in silicon with a hybrid pixel detector using the TimePix3 readout*, presents the first results of antiproton annihilations in a Timepix3 detector. For this publication I wrote the whole article, did all the analysis and simulations and participated in the data taking. The third publication is the article *Antiproton tagging and vertex fitting in a Timepix3 detector*. For this publications I also wrote the whole article, did all the analysis and simulations and participated in the data taking.

The two first publications are important because they provided the first results of antiproton annihilations in pixel detectors were clear annihilation clusters could be seen. These results made it possible to plan the work that lead to third publication, both in terms of simulation effort and how the data collection should be carried out. The third publication is the most important one, and presents the main results of this thesis.

For this reason the two first publications are put into context and referred to in chapter 3, while chapter 5, 6 and 7 is an extended version of the main publication.

1. Introduction and motivation

The aim of the AEgIS experiment is to measure the gravitational acceleration of antimatter. For achieving this a detector able to tag antiprotons and reconstruct their annihilation point is needed. The aim of this chapter is first to give the motivation for the gravity measurement and qualitatively describe the proposed method. Then the requirements the proposed method sets on the detector is discussed.

1.1. What is an antiparticle?

It is both theoretically predicted and experimentally verified that elementary particles have a corresponding antiparticle [1]. The existence of antiparticles was first predicted by the Dirac equation, which is the relativistic counterpart of the Schrödinger equation, and was derived in 1928 [2]. A particle and its antiparticle are identical except that all their additive quantum numbers (electric charge, baryon number, lepton number and the flavor charges) are opposite [3].

In a particle reaction, the electric charge, baryon number and lepton number is always conserved. The flavor charges are always conserved in strong and electromagnetic interactions, while they are approximately conserved in weak interactions. This is the reason why processes converting energy to mass generates the same amount of antimatter and matter. The opposite is also the case, matter and antimatter will annihilate with each other and create energy [3].

In the same way as all particles are built up of elementary particles, complex antiparticles can be build up from elementary antiparticles. The most complex antiparticle that has been made in the laboratory – and lived for long enough to be studied – is antihydrogen. The record today is held by the ALPHA experiment at CERN when they in 2011 managed to confine antihydrogen atoms for 1000 seconds [4].

1.2. The antiproton decelerator

The antiproton decelerator (AD) at CERN is part of the CERN accelerator complex and is currently the only source of low energy antiprotons in the world [5, 6]. A schematic overview of CERN accelerator complex is found in figure 1.1.

The production of antiprotons is accomplished by firing a beam of high energy protons into an iridium target. The high energy proton beam comes from the CERN accelerator complex. First the protons are accelerated in linac2, then in the booster before they reach an energy of 26 GeV in the PS (Proton Synchrotron). Shots of around 1.5×10^{13} antiprotons are then fired into the iridium target. The kinetic energy of the protons is converted into a shower of different particles, and due to the conservation laws equal amounts of matter and antimatter are produced. For each proton shot around 3.3×10^{7} antiprotons of energy ≈ 3.6 GeV is produced, and these are guided into the AD by means of strong magnets.

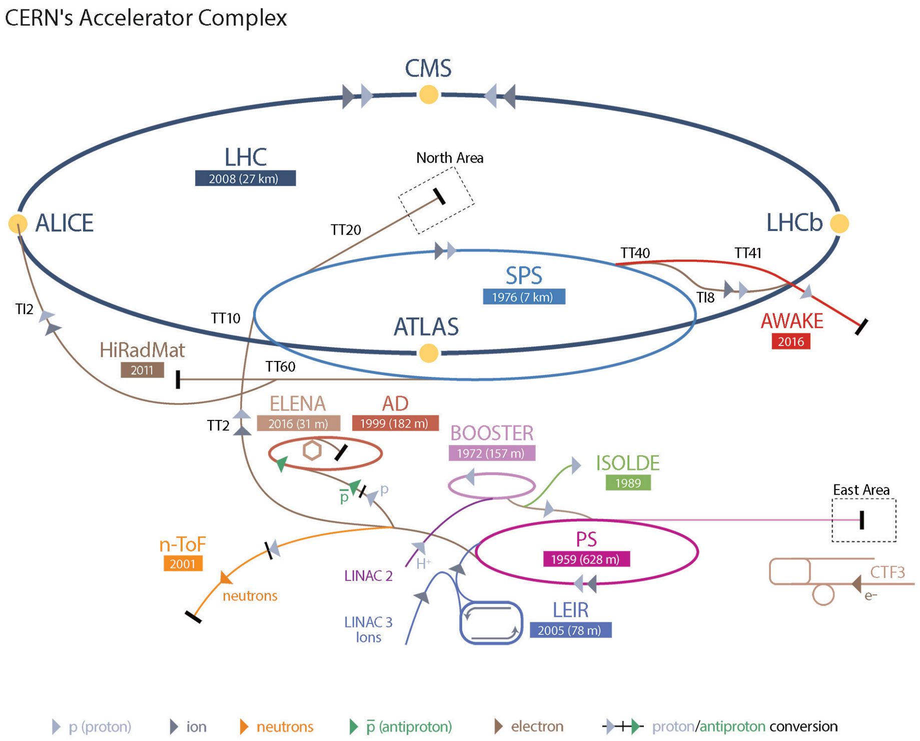

Figure 1.1.: Overview of the CERN accelerator complex. The proton beam that produces the antiprotons is first accelerated in linac2, then in booster and at last in PS before being fired into the iridium target where the antiprotons are produced. Figure from [7].

The antiprotons circulate for around 100 seconds in the AD while their energy is reduced down to 5.3 MeV by ramping down the synchronous energy of the machine. Simultaneously the temperature of the beam, meaning the spread in energy and transverse momentum of the beam particles, is reduced by stochastic cooling and electron cooling. The intensity of the antiproton beam is reduced to around 3.0×10^7 antiprotons due to losses in the cooling processes. Along the AD ring there are four extraction points, corresponding to the four AD experiments (AEgIS, ALPHA, ASACUSA and BASE). At the end of the 100 s cool down process a spill of around 3×10^7 antiprotons is extracted into one of the experiments. The kinetic energy of the antiprotons is 5.3 MeV and the longitudinal spread of the spill is 100–200 ns.

1.3. Antimatter and the weak equivalence principle

The weak equivalence principle is an important building block of general relativity, and states that locally there is no difference between an accelerated reference frame and a gravitational field. The most common way to explain this is by imagine an elevator in space compared to the surface of the earth. If the acceleration of the elevator is the same as the gravitational acceleration on earth, an observer can not tell the difference between these two reference frames. According to the weak equivalence principle this is a general law, meaning that the outcome of all experiments should be the same in the accelerated frame and in the corresponding gravitational field. This has several known and observed predictions, such as the bending of light in a gravitational field and the gravitational red-shift. In the context of the AEgIS experiment, the most important prediction is that the gravitational acceleration is independent of the mass and internal structure of an object in free fall.

The weak equivalence principle has been extensively tested, and today there is no experiments contradicting it [8]. However, it has never been tested for antimatter [9]. The AEgIS experiment plans to perform the first test on antimatter by measuring the gravitational acceleration of antimatter in the gravitational field of the earth, and measure if it is the same as for ordinary matter.

If the weak equivalence principle is proven wrong, the theory of general relativity has to be looked upon with new eyes. Confirming that the weak equivalence principle holds also for antimatter would further strengthen the theory.

1.4. Measuring the gravitational fall on antimatter

The AEgIS collaboration plans to carry out the gravity measurement on antihydrogen, as antihydrogen is the only neutral antiatom that has been produced at low energies today. It is essential to use neutral particles since the electromagnetic forces are far stronger than gravity for microscopic objects.

The plan is to send a beam of low energy antihydrogen through a classical moiré deflectometer [10]. A classical moiré deflectometer consists of two or three equally spaced gratings with a periodicity d. For the gravity measurement the plan is to use two gratings and a position sensitive detector placed at the position of the third. By sending a beam of low energy antihydrogen through these gratings, only certain trajectories are selected and a fringe pattern will appear on the detector. Figure 1.2 show an illustration of this setup and the path of the antihydrogen atoms under the influence of a gravitational field.

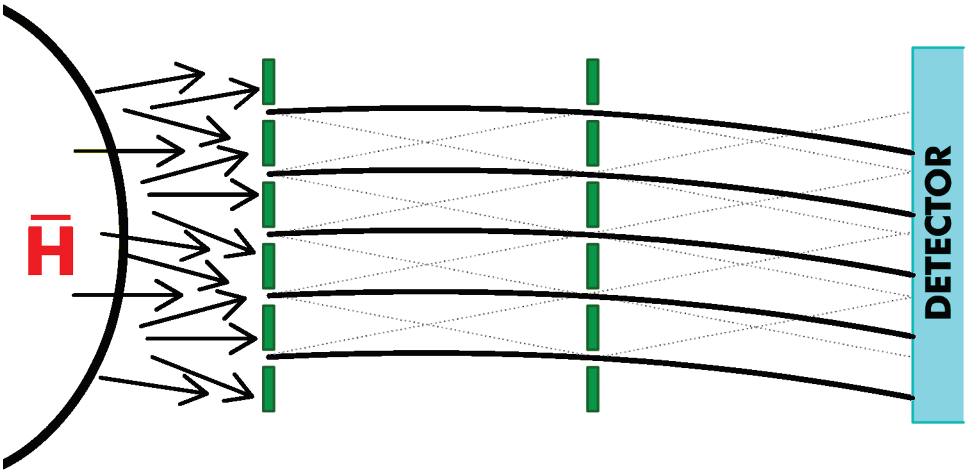

Figure 1.2.: Principle of a classical moiré deflectometer: The paths of the antihydrogen atoms are bent by the gravitational field of the earth. By comparing the fringe pattern created by the antihydrogen to the one created by undeflected paths, the fall due to gravity can be determined.

By comparing the fringe pattern created by the antihydrogen atoms to the pattern created by undeflected paths, for instance from a light source, the shift due to the gravitational acceleration can be determined. The magnitude of the shift is given by

$$\Delta y = \bar{g}\tau^2 , \tag{1.1}$$

where $\bar{g}$ is the gravitational acceleration on antimatter and τ is the time spent by a particle between two gratings.

A moiré deflectometer works in the purely classical regime, and therefore the period of the gratings must be larger than the de Broglie wavelength, which for antihydrogen means that the period must be lager than 20 µm [9]. Space constrains in the AEgIS experiment limits the total length of the gravity experiment to be around 1 m. The exact setup to be used is not completely determined, as it depends on the development and testing of other parts of the experiment, mainly the flux, longitudinal velocity and temperature of the antihydrogen beam.

A proposed setup for the moiré deflectometer is to use 40 cm spacing between the gratings, 60–80 µm grating period and opening fraction of 0.3. As around 90% of the antiprotons will than annihilate in the gratings, also fragments from annihilations in the gratings might reach the detector. With a longitudinal beam velocity of 500 m/s, the shift of the pattern is expected to be 6.3 µm as given by equation (1.1), given that the gravitational acceleration is the same for matter and antimatter. The time it takes for a antihydrogen atom to pass through a moiré deflectometer with a total length of 1 m is around 2 000 000 ns.

An absolute requirement for the position resolution of the detector is to be below the proposed 60–80 µm periodicity of the moiré deflectometer. Since a completely mono-energetic beam is not achievable, the detector must also be able to measure the time of arrival of the antiprotons. The value of τ in equation (1.1) depends on the exact velocity of the antihydrogen atom, and this can be accounted for if the transit time through the moiré deflectometer is known for each individual antihydrogen. As will be discussed in chapter 2 the time resolution of a Timepix3 detector is 1–2 ns, and this value is insignificant compared to the expected transit time.

Simulated results from the AEgIS proposal [9] show that the precision of the gravity measurement as a function of the flux is given by

$$\sigma_{\Phi_g} = \frac{0.4}{\sqrt{N}}\mathrm{rad}, \tag{1.2}$$

where Φ_g is the phase shift in radians and N is the accumulated number of detected antihydrogen atoms. For these simulations it was assumed that the beam had a longitudinal velocity of 500 m/s and a temperature of 100 mK. An infinite detector resolution and exactly known transit time for the antiprotons through the moiré deflectometer was also assumed. The moiré deflectometer had the proposed 40 cm space between the gratings, a grating period of 80 µm, and an opening fraction of 0.3. The results are valid for N in the range N$\simeq 10^3 - 10^5$. If the position resolution is increased to 10.0, 12.5, 15.0 and 17.5 µm, the uncertainty of the phase shift increases respectively with a factor of 2, 2.5, 3 and 4. With a higher position resolution systematic effects became noticeable [9].

In order to measure the $\bar{g}$ to a precision of 1% equation 1.2 predicts that around 2×10^4 antiprotons must be detected, given a position resolution of 10 µm. This amount of antiprotons should be experimentally achievable [9].

In general it should be noted that all predictions for the required position resolution depends upon parameters that are unknown today, for instance the exact velocity, temperature, and flux of the antihydrogen beam. Therefore, these predictions should be seen as rough guidelines for what needs to be achieved, and not absolute requirements or limits.

As a proof of principle a small moiré deflectometer with a grating period of 40 µm and 25 mm distance between the gratings was built [11]. This moiré deflectometer was tested with antiprotons and a magnetic field mimicking the gravitational field. The strength of the magnetic field was $\approx$ 10 Gauss, and the mean velocity of the antiprotons in the longitudinal direction was 4.5×10^6 m/s. The measured shift was estimated to be 9.8 µm $\pm$ 7.3µm (systematic + statistical uncertainty), and this was consistent with what would be expected from the magnetic field. The magnitude of the shift is comparable to the final gravity experiment, and therefore this experiment proved that such a shift can be observed.

An emulsion detector was used for this proof of principle measurement. Such a detector has an excellent position resolution for antiprotons, in the order of a few µm [12]. However, it does not provide time information as the recorded tracks in the detector can only be observed using a microscope. This meant that the mean transit time through the moiré deflectometer had to be assumed instead of the actual transit time for the individual antiprotons. This approximation is the main reason for the large systematic uncertainty. That an emulsion detector has to be moved out of the experimental zone in order to see any signal is also impractical, especially during the testing phases of an experimental setup. For these reasons it is important to look into detector technologies where both time information and online monitoring is available, even though they might posses worse position resolution.

1.5. Conclusion

The AEgIS collaboration plans to measure the gravitational acceleration of antimatter by means of a classical moiré deflectometer, in order to test the weak equivalence principle. The expected shift of the fringe pattern created by the deflectometer will be around 5-10 µm for the proposed experimental setup. It is important that the detector is able to correctly tag antiprotons as other particles might also hit the detector. To be able to measure the gravitational acceleration to an accuracy of 1 %, which is the scientific goal of the AEgIS collaboration, a position resolution around 10 µm is needed. In order to observe a shift of the fringe pattern the position resolution needs to be smaller than the grating period of the moiré deflectometer, which will be in the range of 60–80 µm.

2. Semiconductor detectors

A semiconductor detector is a device that uses a semiconducting material, commonly silicon, to measure the effect of ionizing radiation in a sensitive detector material. This chapter first explains the theory behind creating the sensitive region of the detector by means of a pn-junction. Then follows a description of the signal creation and collection in a detector. The discussion in these two sections is based on [13, 14, 15]. At the end the Timepix3 detector is introduced, as this was the detector used for collecting the majority of the data for this thesis.

2.1. Creating the sensitive region

Silicon is a semiconducting material at room temperature, which means its electric properties falls between that of a conductor and an insulator. Its conducting properties can be explained in terms of a band structure. A band is defined as a range of allowed energies for the electrons. The electrons in a metallic structure can be in the conducting or valence band of the material. The Fermi level, defined as the energy needed to add one electron to the solid, lies between these two bands. Only electrons in the conduction band can transport charge. The band gap is defined as the area between these two bands, and consist of energy levels the electrons are not allowed to populate. The magnitude of the band gap is therefore also the energy needed by an electron in the valence band to jump into the conducting band.

A conductor has no band gap and therefore has no barrier for the electrons to get into the conducting band. An insulator has a large band-gap making it very hard for electrons to get into the conducting band. A semiconductor has a small band gap, so electrons can easily be thermally excited into conducting band. The occupancy of an allowed state i with energy ϵ_i is given as[15]

$$n_i = \frac{1}{e^{(\epsilon_i - \mu)/kT} + 1} \tag{2.1}$$

where n_i is the probability of the state being filled, T is the absolute temperature in Kelvin, k is the Boltzman constant, and μ is the Fermi level. As T goes towards absolute 0 equation (2.1) approaches the step function

$$\lim_{T \to 0} n_i = \begin{cases} 1 & \epsilon_i \leq \mu \\ 0 & \epsilon_i \geq \mu \end{cases} \tag{2.2}$$

such that all levels below the Fermi level (the valence band) is filled and all above (conducting band) is empty. This shows that a semiconductor is an insulator at absolute zero, and its conductivity increases with increasing temperature.

The sensitive area in a detector, also called the depletion region, is placed between electrodes. Current should only flow between the electrodes as a result of particles interacting with the material. Therefore, the electrons populating the conducting band in the sensitive region has to be removed. This can be done with a pn-junction created by putting p-doped material next to n-doped material. A n-doped material contains impurities resulting in extra electrons in the conducting band, while a p-doped material contains impurities giving extra holes in the valence band. In the pn-junction electron and holes diffuse into the oppositely doped area and recombine, creating an non-conducting area without free charges. As the electrons and holes diffuse there is a displacement of charge, resulting in an electric field across the detector, usually called the build-in or equilibrium field. The field in the detector is given by Gauss law

$$\nabla \cdot E = \frac{\rho}{\epsilon_0} \tag{2.3}$$

where ρ is the density of charges and ϵ_0 is the dielectric constant. An illustration of the charge distribution and build-in field in a pn-junction is shown in figure 2.1a.

Applying an external electric field in the same direction as the build-in field will increase the width of the depletion region as more electrons and holes are removed. The voltage required to extend the depletion region across the whole detector is called the depletion voltage (V_d). Increasing the external voltage above this value adds a constant value to the electric field. Figure 2.1b show the field inside the pn-junction when $V = V_d$ and when $V > V_d$. The pn-junction in figure 2.1 is only for illustration purpose and is not realistic. In section 2.3 the field in a more realistic detector will be shown.

2.2. Creation of the signal in the detector

This section explains how free charge carriers are created in the sensitive material and the effect of diffusion as they drift towards the read-out electrodes. In a pixel detector there is one read-out electrode at each pixel.

2.2.1. Charged particle in the detector

As the depletion region is free from charge carriers no current is flowing to the electrodes unless charge carriers are created for instance by an ionizing particle. In silicon around 3.6 eV of deposited energy is required to create one electron/hole pair, and this conversion between deposited energy and charge is used for simulations in this thesis. The free charges drift in the electric field of the detector, and is collected at the read-out electrodes. Figure 2.2a gives an example of the electric field lines in a pixel detector. Figure 2.2b is described in section 2.2.3.

For a heavy ionizing particle the stopping power or the mean ionizing energy loss per length ($\frac{dE}{dx}$) is described by the Bethe-formula in equation 2.4. The parameters used in this formula is described in table (2.1).

$$-\frac{dE}{dx} = Kz^2 \frac{Z}{A} \frac{1}{\beta^2} \left[\frac{1}{2} \ln \frac{2m_e c^2 \beta^2 \gamma^2 W_{max}}{I^2} - \beta^2 - \frac{\delta(\beta\gamma)}{2} \right] \tag{2.4}$$

As seen from equation (2.4) the energy loss varies with α and β which are both given by the velocity of the particle. The Bethe formula is valid for velocities corresponding to $0.1 < \beta\gamma < 1000$. Figure 2.3 shows the mass stopping power for a muon in copper. The mass stopping power is defined as the stopping power divided by the density of the material. As seen the mass stopping power is high for low energies before reaching a minimum

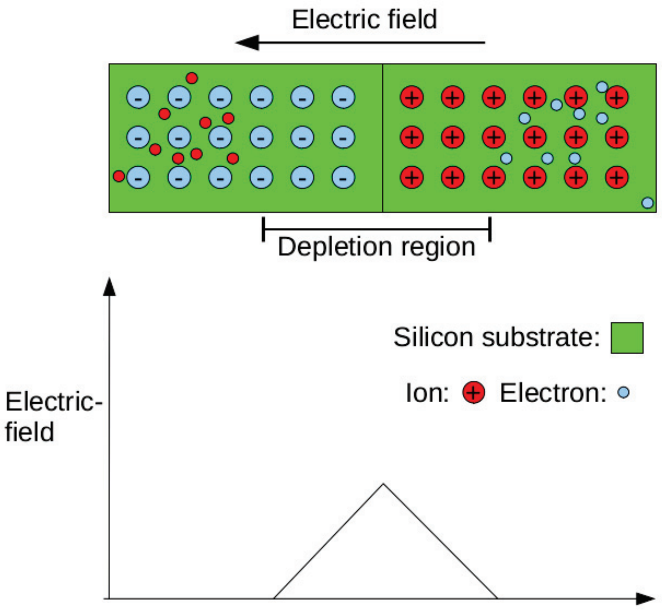

(a) The electron and holes diffuse over the pn-junction until an equilibrium between diffusion and drift is reached. This creates the build-in electric field of the detector.

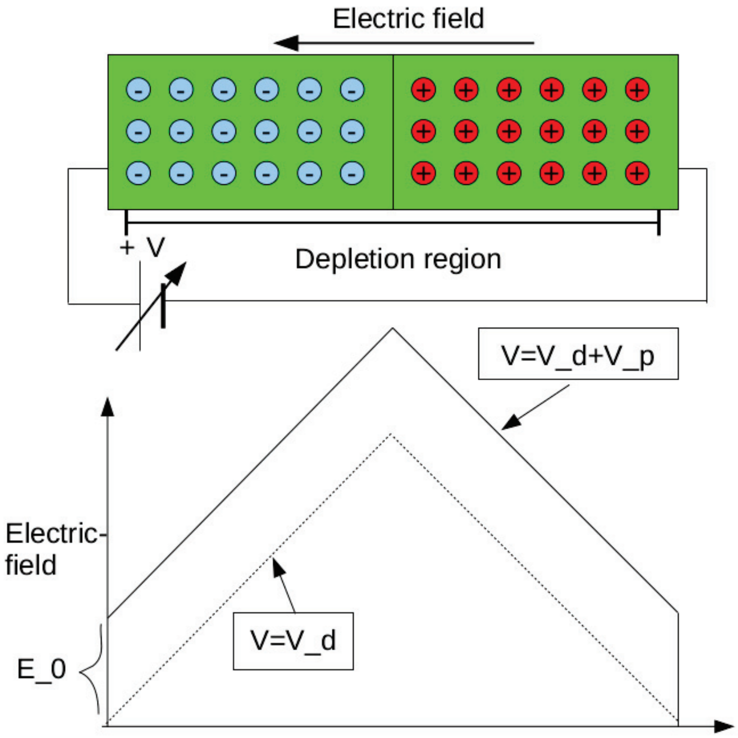

(b) When a external voltage at the depletion voltage (V_d) or above is applied all the free charge carriers are removed. Applying a voltage above the depletion voltage (V_p) adds a constant value to the field inside the detector.

Figure 2.1.: When the free charge carriers are removed from pn-junction, the exposed ions creates an electric field in the detector. Using an external electric field the depletion region can be extended across the whole detector.

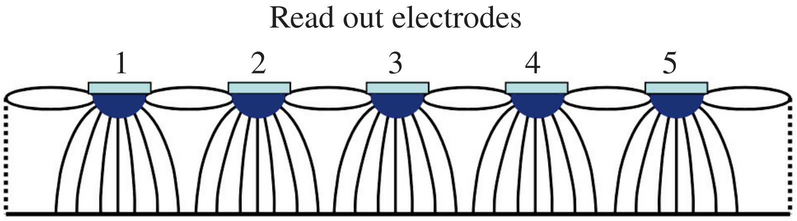

(a) Illustration of the electric field in a pixel detector when a bias voltage is applied.

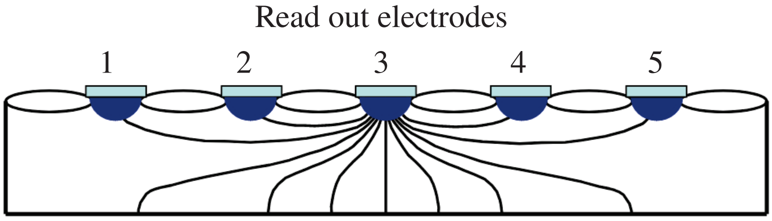

(b) The weighting field for electrode 3.

Figure 2.2.: Illustration of the electric field a) and the weighting field b) in a detector as seen as a slice trough the detector. Figure from [16].

Table 2.1.: Parameters used in the Bethe formula in equation (2.4)

N_A	Avogadro's number
r_e	Classical atomic radius
m_e	Electrons mass
K	$4\pi N_A r_e^2 m_e c^2$
Z	Atomic number of absorber material
A	Atomic mass of absorber in $\frac{g}{mol}$
c	Speed of light in vacuum
v	Velocity of impacting particle
β	$\frac{v}{c}$
γ^2	$1-(1/\beta^2)$
W_{max}	Maximum energy transfer in a single collision. for particles with mass M$\gg$ m$_e$
I	Mean excitation energy
$\delta(\beta\gamma)$	Density effect correction to ionizing energy loss. Depends on the material and is important for high energies $\beta\gamma \approx 100$ or higher

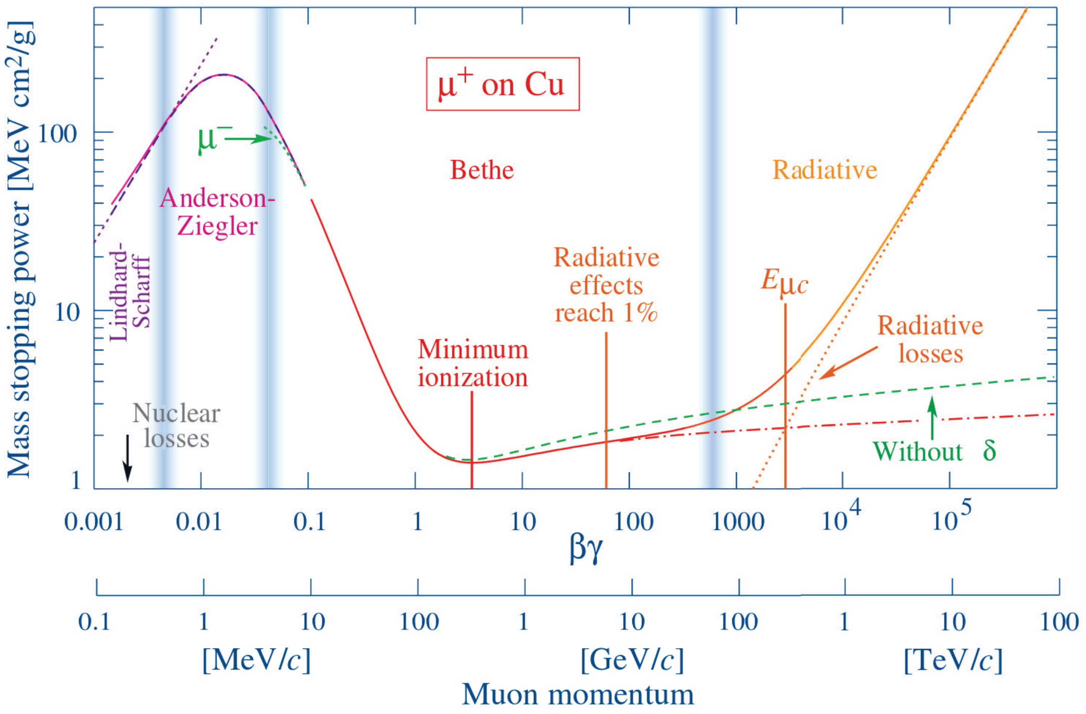

Figure 2.3.: The mass stopping power of a muon in copper as a function of $\beta\gamma$. The solid line indicates the total stopping power, and shows how the energy loss is large per unit length for low energies before it drops and rises again due to radiative losses. The red line gives the Bethe formula, and as expected it overlaps with the solid line in the area $0.1 < \gamma\beta < 1000$. Figure from [13].

and then slowly goes up again. When a particle is in this minimum plateau it is called a minimum ionizing particle (MIP). This minimum is found around $\gamma\beta$ = 3.0-3.5 depending on the material. A pion is a MIP at around 350 MeV in silicon, while a proton is a MIP at around 2350 MeV.

Energy loss is a stochastic process, and the Bethe formula gives the mean energy loss. The variation around the mean is given by the Landau distribution.

2.2.2. Charge diffusion

Charges liberated by energy depositions will diffuse as a result of random thermal motion in the metal. A point like charge carrier concentration will after a time t_d be spread out as a Gaussian distribution with standard deviation given by [14]:

$$\sigma = \sqrt{2Dt_d}, \tag{2.5}$$

where D is the diffusion constant that depends on the material and carrier type (electrons or holes). The diffusion constant for holes in silicon is 12 cm^2/s, while for electrons it is 36 cm^2/s at room temperature [17]. The following model gives the collection time t_d for free charge carriers when interactions between the carriers are not considered [15, 18]:

$$t_d = \frac{w^2}{2\mu V_d} \ln\left(1.0 - \frac{z}{w} \cdot \frac{2V_d}{V + V_d}\right) \tag{2.6}$$

Here z is the depth of the energy deposition, w the thickness of the detector, V_d the depletion voltage, μ the carrier mobility and V the applied voltage. This show that higher bias voltage on the detector gives shorter collection time, that further leads to less diffusion and then less charge sharing between pixels.

2.2.3. Charge collection and the Ramo theorem

For a pixel detector there is usually one electrode connected to each pixel. The electric signal in an electrode is caused by induction of current and not the actual free charges reaching the electrode. The Ramo theorem [19] describes this behavior and states that the instantaneous current in an electrode i is given by

$$I_i = -q_p \vec{v}_p \cdot \vec{E}_{W_i} \tag{2.7}$$

where q_p is the charge moving in the detector, $\vec{v}_p$ is its velocity and $\vec{E}_{W_i}$ is the weighting field from electrode i. The weighting field for electrode i is defined as the field present if that electrode is at unit potential, while all other electrodes are at zero potential. Figure 2.2b shows the weighting field for electrode number 3. The charge collected in an electrode is equal to the integrated current. As seen the weighting field is strongest closest to the electrode under consideration, hence the current flowing in an electrode is highest as the charge is collected in that electrode. However, the weighting field from one electrode extends in the whole detector. Therefore current is also flowing in pixels where no charge is collected, however the integral will be zero. So charge collected in for instance electrode 3 will cause current to also flow in all the other electrodes, even those so far away that no charge is collected there. This knowledge is important for understanding why hits not caused by actual charge collection are seen in the Timepix3 data. These so called halo hits will be discussed in detail in section 3.4.1.

2.3. The Timepix3 detector

The detector used for most of the antiproton studies in this thesis consisted of a 675 µm or 300 µm thick segmented silicon sensor bump bonded to an ASIC with the Timepix3 [20] readout system. The silicon sensor has a 0.5 µm thick aluminum layer on top. For simplicity such a detector is often just called a Timepix3 detector. The size of a Timepix3 detector is 1.4×1.4 cm, it has 256×256 pixels, and a pixel pitch of 55 µm. Each pixel is self triggering and able to simultaneously measure both Time of Arrival (ToA) and the amount of charge collected in each electrode. For measuring the ToA the Timepix readout system has a general clock for time stamping running at 40 MHz. When a pixel is triggered a faster clock of 640 MHz starts running until the next time stamp from the general clock. Combining these two internal clocks gives a time resolution of 1–2 ns, and this is very small compared to the 2 000 000 ns travel time of the antihydrogen atoms trough the moiré deflectometer. The dead time of the pixels is given as the ToT pulse time + 475 ns [20]. A photo of the 675 µm thick Timepix3 detector is shown in figure 2.4.

In order to quantitatively study different detector effects, especially related to large energy depositions, a simple TCAD model of the 675 µm thick Timepix3 detector is developed as a part of this thesis. TCAD stands for Technology Computer Aided Design, and here the Synopsys TCAD package is used [21]. A TCAD model of a detector is made by defining

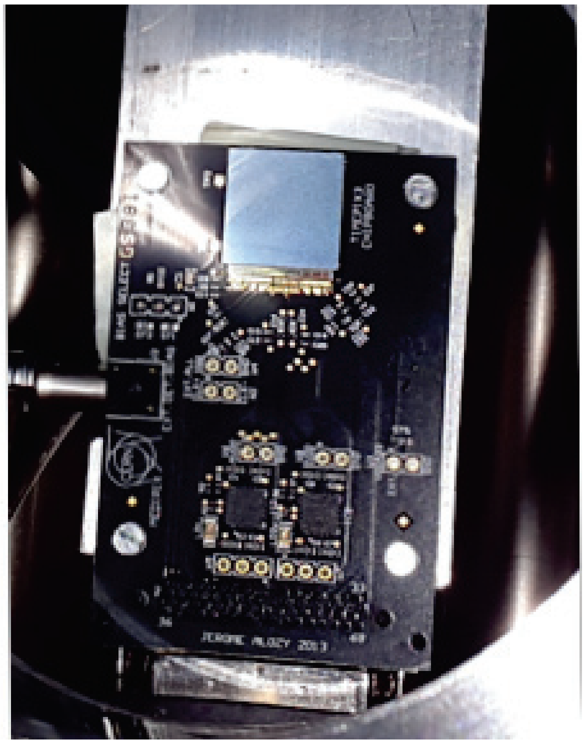

Figure 2.4.: The 675 µm thick Timepix3 detector as it was mounted on the end plate of GRACE. The GRACE beam line is described in chapter 4

the geometry, the material with its doping concentrations, and the position of the electrodes. The bulk of the sensor in the modeled Timepix3 detector consists of a 675 µm thick low n-doped silicon material. The PN junction is created by implanting a heavy p-doped material around the electrodes and heavy n-doped material on the backside. The heavy doped material extends into the detector bulk by means of diffusion. This is also an example of a more usual doping configuration where the detector consist of a large bulk of low doped material, and very thin implants of heavier doped materials on the backside and around the electrodes.

The input to the TCAD model is the potential at the different electrodes. Then TCAD uses Maxwells equations and Boltzman transport equations to provide information about the electric field in the detector, the carrier concentration and the current flowing in the electrodes. In the Synopsys TCAD package these differential equations are solved by the finite element method.

The TCAD model of the Timepix3 detector is a 2D model with cylindrical symmetry. Only 9 pixels are simulated because the simulations are computationally very heavy. Figure 2.5 shows the field in the detector bulk for a bias voltage of 200 V as given by the TCAD model. An applied voltage of 200 V corresponds to the depletion voltage for this detector. As expected at the depletion voltage the electric field in the bulk starts at around 0 and increases linearly.

When the geometry and the electric fields in a model of a detector has been established, TCAD can also model how en energy deposition would be collected in the detector. Free charges can be inserted into the model, and TCAD then simulates how they drift and diffuse in the detector. By using the conversion that 1 electron/hole pair corresponds to a 3.6 eV energy deposition, one can simulate the response of the detector to energy depositions and

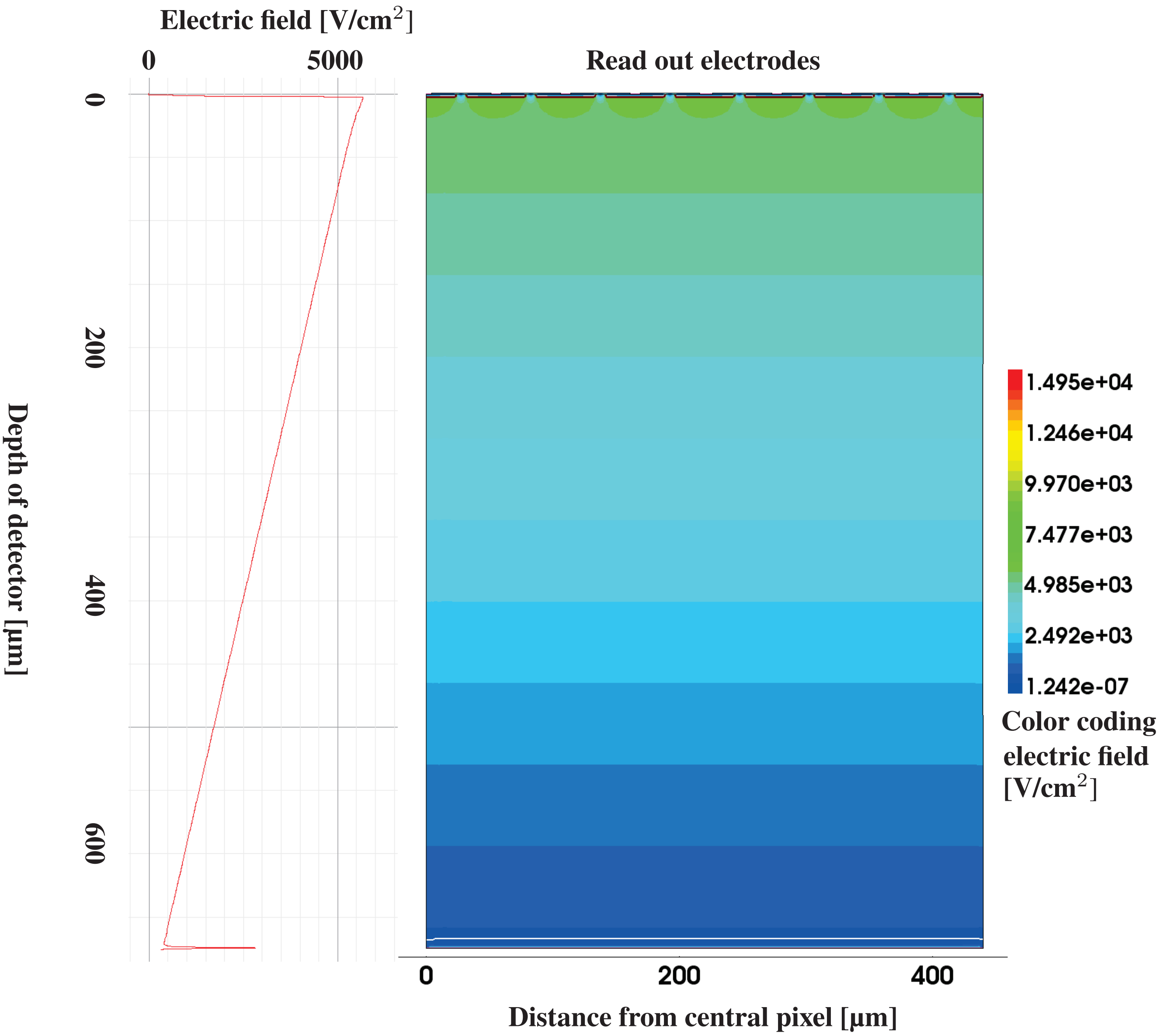

Figure 2.5.: Electric field in the Timepix3 detector at the depletion voltage of 200 V. The electric field is found by TCAD simulation.

get the current at the electrodes as a function of time. TCAD takes into consideration the interaction of the free charges with each other, and this will be important for simulating the plasma effect that is described in section 3.4.2.

2.4. Summary

In this chapter the most relevant theory of detectors and how particles interact with matter has been described. First how a pn-junction and external voltage can create a sensitive area where current will only flow if free electron/holes pairs are created by ionizing radiation. Then the Bethe formula is presented, as this is the standard model for the average energy loss by an ionizing particles in a material. Free electron/hole pairs will drift in the electric field of the detector, and diffuse on their way to the electrode. The amount of diffusion depends on how long time they use to get there, the collection time.

A TCAD model of the Timepix3 detector was made to study different detector effects. Results from this model will in chapter 3 be used to understand and explain how large energy depositions impact the Timepix3 detector. In chapter 6 the model is, together with the theory of diffusion, used to model charge sharing between the electrodes.

3. Antiproton annihilations in theory, in simulations, and in pixel detectors

To develop a detector response model to be used for antiproton annihilations it is important to have some knowledge of antiproton annihilations, both some theoretical background, knowledge about simulation tools, and a good understanding of how an antiproton interacts in a detector. The antiprotons studied in this thesis have a kinetic energy below 15 keV. An antiproton entering a material at this energy is slowed down by ionizing energy loss before it annihilates at rest, and therefore only annihilation at rest is considered.

Antiproton annihilations as studied here can also be used for studying antihydrogen annihilations, as the positron annihilates independently on an atomic electron, resulting in two 511 keV photons. These photons will have no significant impact on the antiproton annihilation cluster.

This chapter starts with a brief introduction to the theoretical and experimental status of antiproton annihilations today. The second section discuss how Geant4 [22] and FLUKA [23] can be used for simulating the annihilation events. The preliminary analysis done to select which of these simulation tools to use is also presented. Then follows an overview and description of the measurements of antiproton annihilations that provided the data used for this thesis. The last section discuss different detector effects that was seen in the data. This section also presents the preliminary studies that was carried out in order to quantitatively understand these effects in order to incorporate them in the detector response model presented in chapter 6.

3.1. Antiproton annihilation at rest

An antiproton annihilation with a nucleon (proton or neutron) happens at the quark-antiquark level and will mainly result in a number of charged and uncharged pions. The pions are either produced directly by recombination of the quarks or they are decay products of mesonic resonances [24]. A diagram showing the decay into three pions by rearrangement is found in figure 3.1 There are no good and verified theoretical predictions for the branching rations to different pion configurations [25], and therefore experimental data is important for understanding antiproton annihilations with a nucleon.

One important experiment was the Crystal Barrel experiment at the Low Energy Anti Proton Ring (LEAR) at CERN [26]. LEAR provided an antiproton beam of 200 MeV/c, and the beam was stopped in liquid hydrogen in the center of the experiment. The experiment consisted of a silicon vertex detector closest to the annihilation point and was surrounded by a drift chamber and a calorimeter. Another important experiment was done at the Alternating Gradient Synchrotron at Brokhaven national laboratory where antiprotons where studied in the 30-in Columbia-Brookheaven National Laboratory bubble chambers [27]. The number and momentum of the uncharged pions was determined by conservation of momentum be-

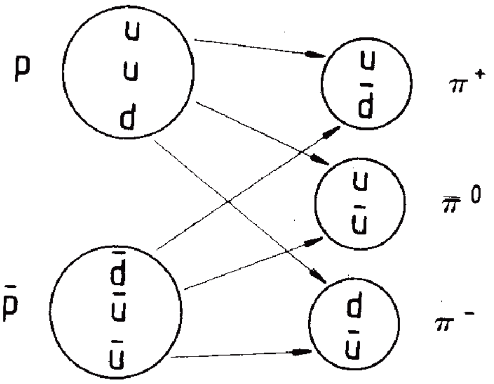

Figure 3.1.: Proton antiproton annihilation into three quarks by means of quark rearrangement.

Number of pions	Combined percentage abundance from experiments [25]	Geant4	FLUKA
2	0.38±0.03 %	5.5 %	5.1%
3	7.4±0.03 %	12.6 %	8.9%
4	18.1±1.8 %	30.8 %	26.6%
5	35.2±3.7 %	34.1 %	20.0%
6	23.2±2.8 %	14.6 %	21.4%
7	3.3±0.03 %	1.2 %	16.2%
8	0 %	0 %	0.4%
9	0 %	0 %	0.9%

Table 3.1.: Comparison of the pionic multiplicity between data and simulation for proton antiproton annihilations. The experimental results are the combined results from Scalay Bubble Chamber at CERN [25], the 30-in Columbia-Brookheaven National Laboratory bubble chamber [27] and the Crystal Barrel experiment at CERN [26]. Neither Geant4 or FLUKA gives completely accurate predictions for the pion multiplicity, and they also differs from each other. Saclay Bubble Chamber

fore and after the annihilation. Table 3.1 shows the pion multiplicity from the Crystal Barrel experiment combined with the results from bubble chambers [25]. The table also include results obtained with FLUKA and GEANT4. The average is 5 pions per annihilation, and of those on average 3 is charged [25].

When an antiproton enters a material, it is first slowed down mainly by ionizing energy loss and, as it comes to rest, it is captured into the atomic orbits of the hit atom. The antiproton cascades down towards the nucleus by emission of Auger electrons and x-rays, and finally annihilates with one of the atomic nucleons. As described this antiproton nucleon annihilation creates pions. The total available energy from the annihilation is 1880 MeV, and it is estimated that an excitation energy of up to 800 MeV can be transferred to the nucleus. This creates an intra-nuclear cascade causing direct emission of fast pions, protons and heavier particles. Then follows evaporation of nucleons from the heated nucleus. Lighter nuclei, like silicon atoms, may undergo fragmentation in addition [28].

Fragments	p (6-18 MeV)	d (8-24 MeV)	t (11-29)	^{3}He (36-70)	α (36-70)
LEAR ^{12}C	23.3±2	9.3±0.8	2.8±0.1	1.7±0.17	1.14±0.12
Geant4 ^{12}C	3.0	0.0	0.0	0.4	12
FLUKA ^{12}C	18.3	13.1	5.0	2.0	2.5
LEAR ^{40}Ca	74.2±4.1	18.1±1.1	5.7±0.4	2.22±0.17	2.18±0.16
Geant4 ^{40}Ca	6.7	0	0	0.1	4.0
FLUKA ^{40}Ca	30.2	19.1	8.1	0.2	1.6

Table 3.2.: Comparison between simulated results and the LEAR experiment for antiprotons annihilations in targets of ^{12}C and ^{40}Ca [29]. FLUKA seems to better replicate the experimental results.

At LEAR annihilation of antiprotons with nuclei of ^{12}C, ^{40}Ca, ^{63}Cu, ^{92}Mo, ^{98}Mo and ^{238}U where studied [29]. Table 3.2 show the observed annihilation products for ^{12}C and ^{40}Ca, as these atoms are the most similar to silicon. The experimental results are compared with simulated results obtained with Geant4 and FLUKA.

3.2. Simulating antiproton annihilations

As discussed in chapter 2 particles interacting with material loose energy mainly by creating free electron/hole pairs, and the detectors collects and measures this charge. The starting point for developing a detector response model is therefore to know the magnitude and position of the deposited energy of the particles interacting with the detector. Both Geant4 and FLUKA simulates hadronic interaction, for instance annihilation of antiprotons, and energy loss caused by particles traveling in the detector bulk. Therefore they are both candidates for delivering the input information to the detector response model. In figure 3.2 the simulated multiplicity of the annihilation fragments for antiproton annihilation in silicon is compared between FLUKA and Geant4. As seen the predicted multiplicities are not exactly the same, and the choice between Geant4 and FLUKA is therefore based upon how well they reproduce the experimental results available.

From Table 3.1 it looks as both Geant4 and FLUKA does a reasonably, but far from perfect, job at reproducing the experimental pionic multiplicity. For annihilations in materials as shown in Table 3.2 it is clear that FLUKA more accurately reproduces the experimental results. More recent studies using an emulsion detector also show that FLUKA is better at predicting the multiplicity of pions and heavier fragments when antiprotons annihilates in copper, silver and gold at low energies [30]. For these reasons FLUKA is chosen as the simulations software for developing the detector response model in this thesis. It should however be noted that the comparison between data and simulation is far from perfect, and this is always kept in mind when evaluating the results from the model.

FLUKA models the annihilation of an antiproton with a nucleus in two steps [31]. First as an antiproton-nucleon annihilation that results in pions, where the branching ratios to different pionic multiplicities are tuned to experimental data. The next step is the interaction between the nucleus and the pions that happens to penetrate the nucleus. This interaction is simulated by the PEANUT model [32] that FLUKA use for all hadronic interactions. The hadronic interaction between a pion and the nucleus is first an intra nuclear cascade, meaning

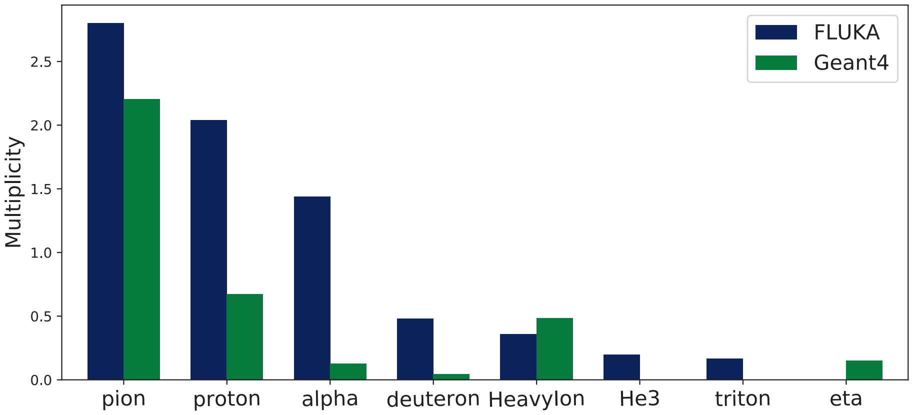

Figure 3.2.: Multiplicity of fragments when an antiproton annihilates in silicon as simulated with FLUKA and Geant4.

a successive chain of two body interactions of projectile and reaction products. Then follows evaporation and fragmentation due the excess energy transferred by the pions to the nucleus. The result of the annihilation is that the nucleus is fragmented and all the fragments travel away from the annihilation point.

3.3. Measurements of direct annihilation of antiprotons in pixel detectors

The fragments that moves away from the annihilation point give rise to a star shaped signature in a pixel detector if they travel in the plane of the detector. These tracks are from here on called prongs.

In 2012 these star shaped signatures was for the first time observed in a silicon pixel detector when low energy antiprotons annihilated directly on the detector surface [33]. One example of these star shaped annihilation is seen in figure 3.3, however the frequency of these clear annihilations was quite sparse in the data. The analysis of the data was published in the article *Comparison of Planar and 3D Silicon Pixel Sensors Used for Detection of Low Energy Antiprotons* found in appendix E. The simulation of the 3D pixel detector in this article was the first simulation done for this thesis. At that time the option of using FLUKA had not been explored, and therefore the virtual MC framework of Geant4 was used instead. The article includes comparison between data and simulation for the cluster size and deposited energy in a cluster. There are two main takeaways from this study. The first is that an antiproton annihilation can be recognized by its star shaped signature. The second is that the detector was also hit by fragments and pions from annihilations happening other places than on the detector itself, and that this made up the majority of the clusters in the 3D pixel detector data. Clusters caused by such secondary fragments or pions are from here on called secondary clusters, while clusters originating from annihilations actually happening on the detector are from here one called annihilation clusters.

The next experiment where antiprotons annihilated directly on a silicon pixel detector was carried out in 2014 in a vacuum chamber mounted at the end of the ACE beam line.

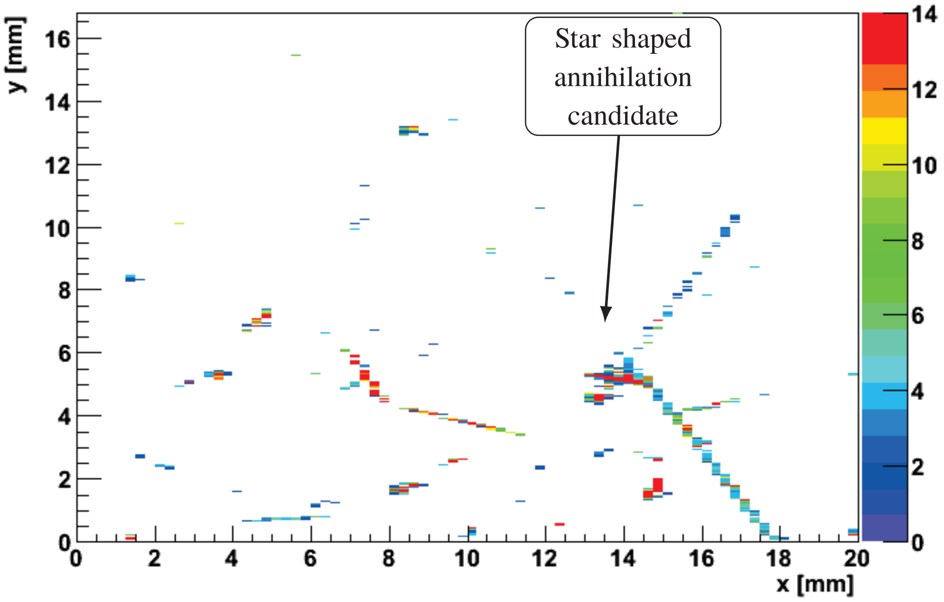

Figure 3.3.: One of the clear annihilation events seen with the 3D pixel detector. The rest of the clusters are most likely from fragments from annihilations happening other places than in the detector itself, so called secondary fragments. Figure from [33].

The ACE beam line is on of the extraction lines of the AD and was previously used by the ACE collaboration who studied the possibility of using antiprotons for cancer therapy [34]. Today the ACE beam line works as a secondary beam line to the AEgIS experiment, and a switching magnet allows this beam line to use spills of antiprotons not needed by the main AEgIS apparatus. Figure 3.4 shows an illustration of the vacuum chamber used for this detector study. A variable degrader was used to spread the beam as much as possible such that individual annihilations could be observed and separated from each other.

The detector used was a 300 µm thick silicon detector with the Timepix3 [20] readout, and this was the first time a Timepix detector was tested with antiprotons in laboratory conditions. Figure 3.5 shows the time laps for one spill of antiprotons. In the first 100 ns after the first particles arrives at the detector some clear annihilations can be seen. These can be recognized by a central area of high energy depositions with one or more prongs originating from this center, giving the characteristic star shape. The presence of the prongs is the main feature to distinguish an annihilation cluster from a secondary cluster. Antiproton annihilations might also result in a cluster without any prongs if none of the fragments travel in the plane of the detector, but these annihilation clusters are not easy to distinguish from secondary clusters. Within one spill the detector quickly starts to saturate, 300 ns after the first particles arrive the frame is completely full. Since the dead time of a pixel is more than 475 ns, the pixels do not recover within one spill. Therefore only the first few particles arriving at the detector could be used for analysis. The analysis done on this data is found in the article *Study of antiproton annihilation in silicon with a hybrid pixel detector using the TimePix3 readout* in appendix F.

For the test beams in 2015 and 2016 a new beam line named GRACE [35] was in place.

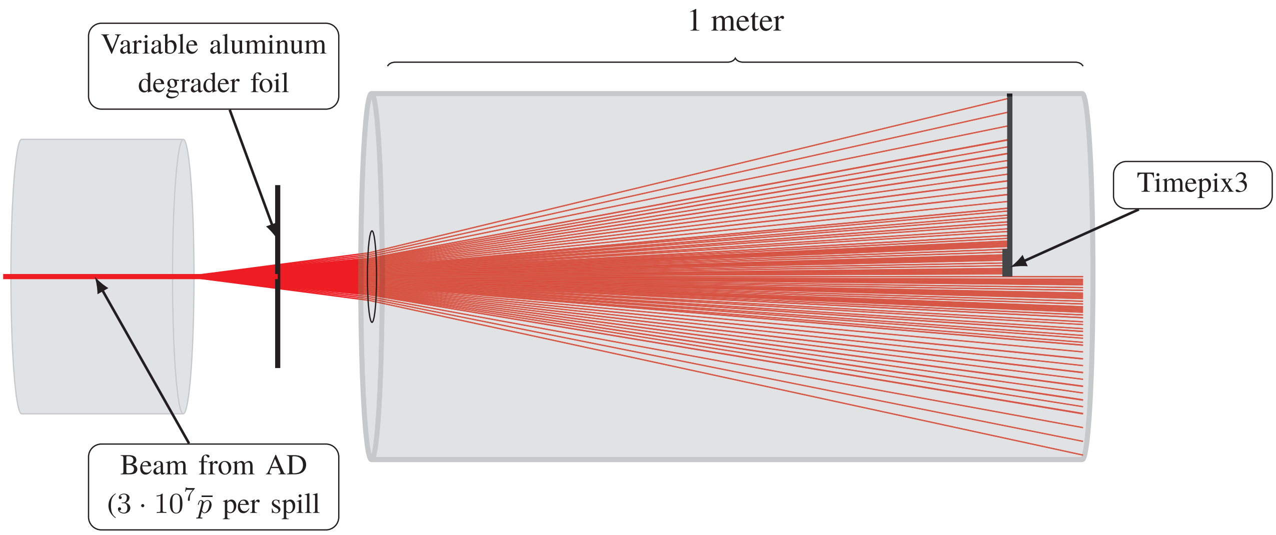

Figure 3.4.: Setup of the simple vacuum chamber at the end of the ACE beam line used during test beam in 2014. Figure not to scale.

Chapter 4 is devoted to this beam line, and in that chapter the beam line is described in detail and the motivation for building it is discussed. In addition a full simulation and data analysis of its performance is carried out. In short the GRACE beam line uses electrostatic bending to direct only the low energy antiprotons toward the detector. Then the annihilation depth is know, and the detector does not saturate due to excessive amounts of particles hitting the detector per spill from AD.

In this beam line a 675 µm thick detector also equipped with the Timepix3 readout was tested. An example of a time laps from the GRACE beam line is shown in figure 3.6. Also here the annihilations can be recognized by a central high energy deposition and prongs originating from this center. Compared to the simple vacuum chamber data seen in figure 3.5 more clear annihilations are seen as the detector does not saturate.

The data set taken in the GRACE beam line was the largest one containing in total 560 spills from the AD and had the most clear annihilations. Therefore this data set was used for the throughout analysis presented in the article *Antiproton tagging and vertex fitting in a Timepix3 detector* found in appendix G. This study, including a few more details than the article, is also presented in chapter 5, 6 and 7.

3.4. Detector response to the large energy depositions.

In the center of an annihilation cluster the amount of deposited energy is large since all fragments extends from this point. In figure 3.7 FLUKA is used to simulate the deposited energy in the central 16 pixels, together with the total deposited energy in the annihilation cluster. As seen antiproton annihilations causes large energy depositions, frequently above 50 MeV for one annihilation. A large amount of this energy, often above 20 MeV is deposited in a small area of 220 µm × 220 µm corresponding to the 16 central pixels. Such high energy depositions give rise to three different peculiar detector responses; the halo hits, the plasma effect and the volcano effect. All these effects are discussed in detail in this section. It is important to quantitatively understand these effects as they have to be taken into

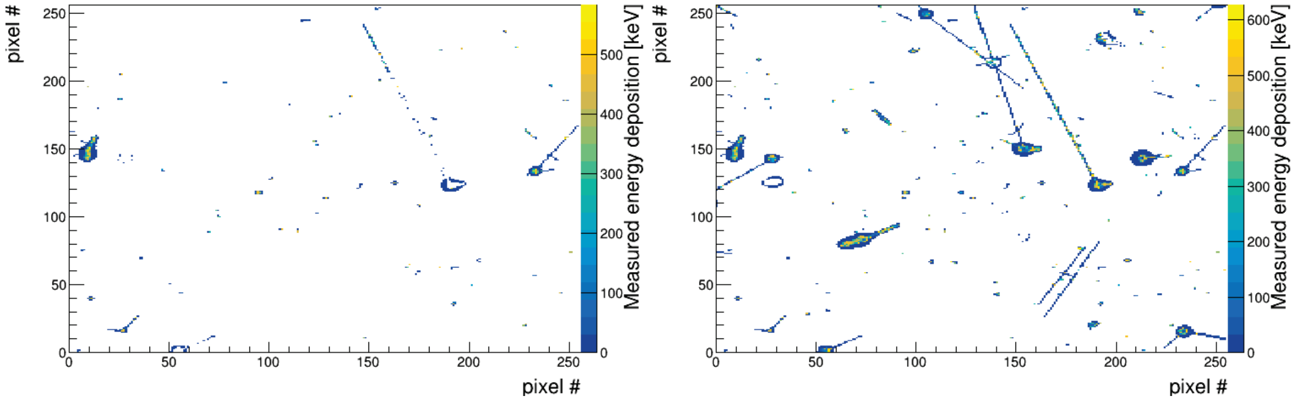

(a) First antiprotons arrive

(b) 50 ns after the first antiprotons arrived

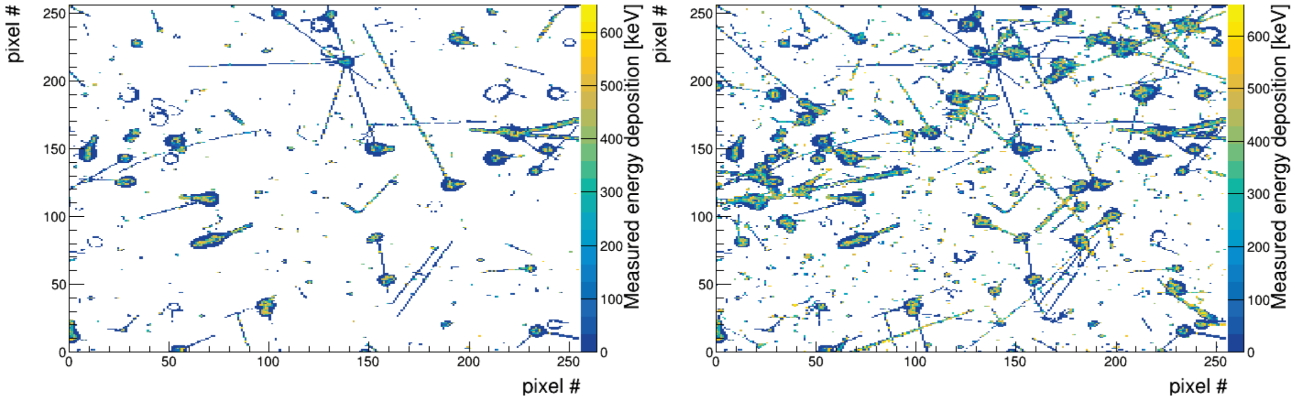

(c) 100 ns after the first antiprotons arrived

(d) 150 ns after the first antiprotons arrived

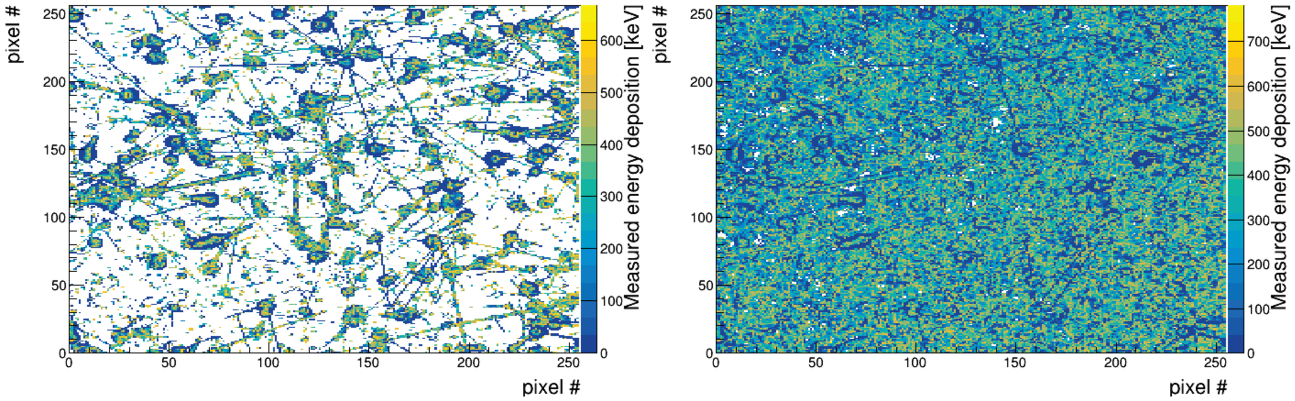

(e) 200 ns after the first antiprotons arrived

(f) 300 ns after the first antiprotons arrived

Figure 3.5.: Time laps for one spill of antiprotons with a simple vacuum chamber at the ACE beam line. During the first 100 ns of the spill a couple of clear annihilations with prongs can be seen before the detector completely saturates. Large energy depositions tend to be surrounded by a ring or halo of lower energy depositions, and this effect is explained in section 3.4.1

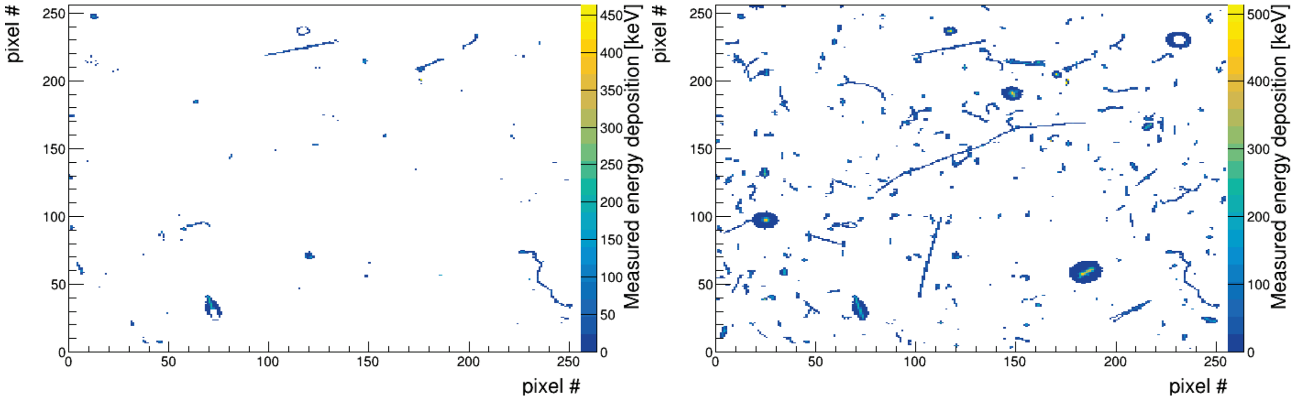

(a) Right before the first antiprotons arrive.

(b) 100 ns after frame a).

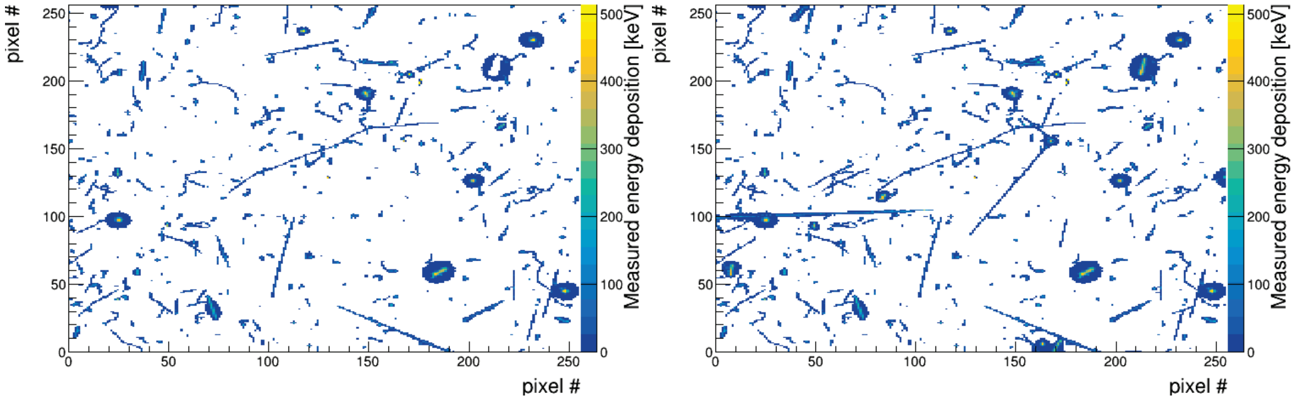

(c) 300 ns after frame a).

(d) 800 ns after frame a).

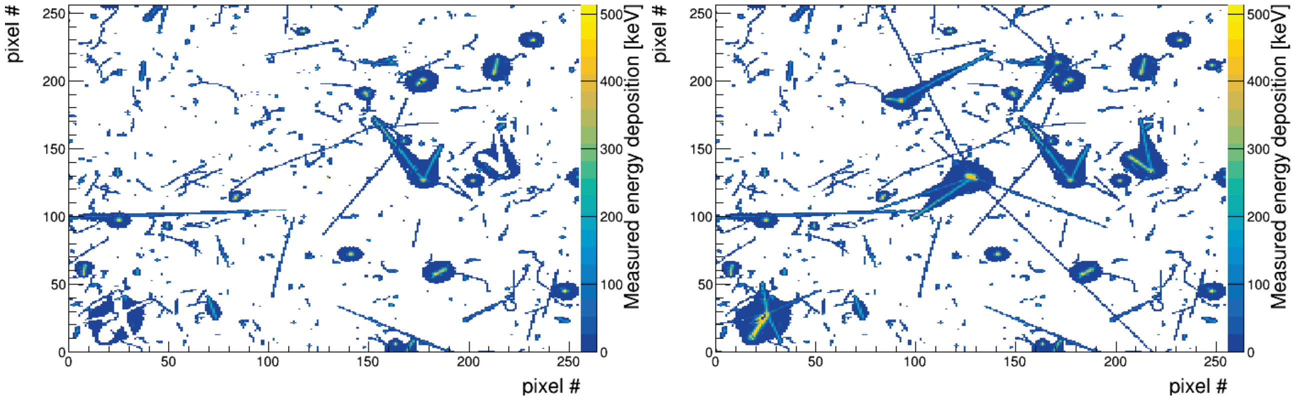

(e) 9000 ns after frame a).

(f) 1000 ns after frame a).

Figure 3.6.: Time laps for one spill of antiprotons in the GRACE beam line. As compared to the simple vacuum chamber the detector does not saturate, and each spill contains more clusters suitable for analysis. Also here large energy depositions tend to be surrounded by a ring or halo of lower energy depositions, and this effect is explained in section 3.4.1.

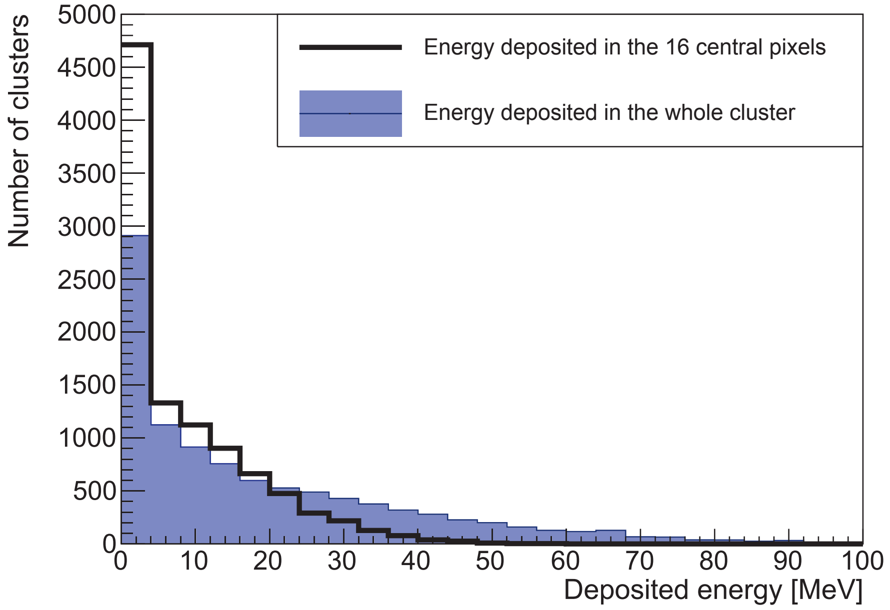

Figure 3.7.: The deposited energy in the center of the annihilation cluster and in the whole annihilation cluster, according to FLUKA. A large amount of the total energy is deposited in the center.

consideration when developing the detector response model. The different effects are studied and described using simulations and the data set from the GRACE beam line collected with the 675 µm thick Timepix3 detector. This data set is from here on referred to as the antiproton data.

3.4.1. Halo

As seen in figure 3.5 and 3.6 large energy depositions tend to create a ring or halo of lower energy depositions around it. The hits constituting this ring is from here on called halo hits. Figure 3.8 shows the energy deposited in all the pixels in the antiproton data, and a peak can be seen at around 3-4 keV. Around 40 % of the pixels have a measured energy below 6 keV, and this excess of low energy hits are the halo hits. The halo hits can not be caused by real particles, since on average a minimum ionizing particle (MIP) generates 80 electron/hole pairs per µm. This means that a MIP only needs to travel 21 µm to deposit 6 keV of energy. Given that the pixel pitch is 55µm and that most of the annihilation products are not MIPs, the amount of pixels with measured energy below 6 keV is unnaturally high.

The exact reason why the halo hits occur is not fully understood, however the current understanding is the following [36]: As discussed in section 2.2.3, charge moving in the Ramo field of a pixel will cause an induced current in that pixel, and for large energy depositions a significant current will flow in pixels far away from where the charge is actually collected. This current can be studied using the device simulation software TCAD, that among other applications, is used to simulate the drift and diffusion of electron/holes in semiconductors. Figure 3.9 shows the current in a pixels 385 µm (7 × 55 µm) away from an 10 MeV energy deposition in the TCAD model of the 675 µm thick Timepix3 detector. As seen there is significant current flowing in the pixel, but the integrated current is zero, so no charge is actually collected in this pixel. However, the time integration of the signal in the front-end is not completely uniform over time, and since the current is flowing over a long time period the result is a small integrated net current. This small integrated current is probably what causes the halo hits.

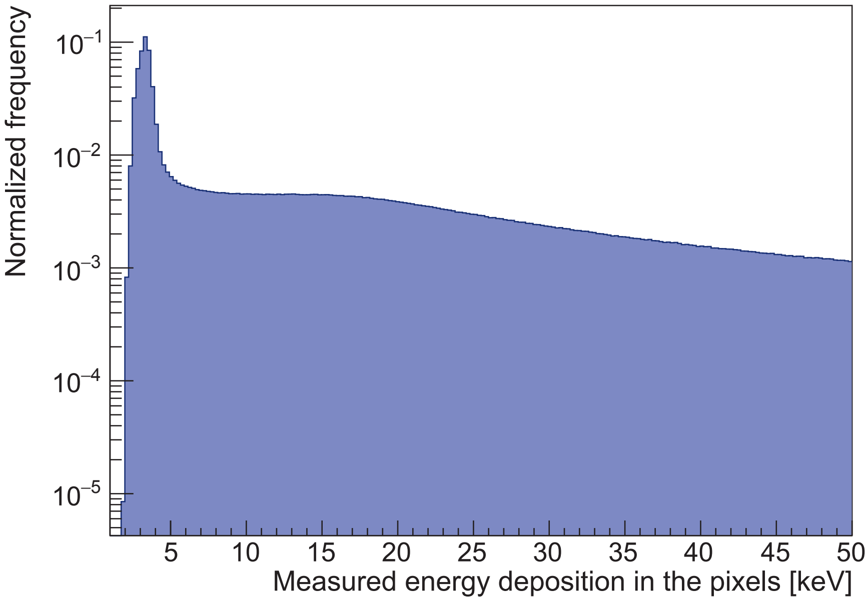

Figure 3.8.: Energy deposited in the individual pixels for the antiproton data. The peak at around 3-4 keV is caused by the halo hits.

3.4.2. Plasma effect

High energy depositions might liberate enough electron/hole pairs to disturb part of the field in the bulk of the detector as they create a neutral plasma. Figure 3.10 shows the field, as simulated with TCAD, in a Timepix3 detector after an energy deposition of 22.5 MeV. As seen the field is almost zero around the energy deposition. This will increase the collection time as the electrons/holes in the center of the plasma don't experience any electric force before the surrounding electron/holes has been removed. This effect is called the plasma effect [37], and leads to more charge sharing between pixels as the electron and holes has more time to diffuse.

The formula for the collection time presented in equation (2.6) does not take the plasma effect into account. The simulation software TCAD takes this effect into account and simulations show that energy depositions above 10 keV has longer collection time than what would be expected from the simple model in equation 2.6. An energy deposition of 10 MeV, which is a common energy deposition in a small area according to figure 3.7, gives an collection time of 1780 ns in a 675 µm thick Timepix3 detector. The size of the charge cloud in terms of its standard deviation at the readout electrodes is then 80 µm in a silicon detector. Since the pixel pitch is only 55 µm, the charge sharing due to the plasma effect has to be taken into consideration when developing the detector response model. Section 6.1.1 will describe how the plasma effect is implemented in the detector response model.

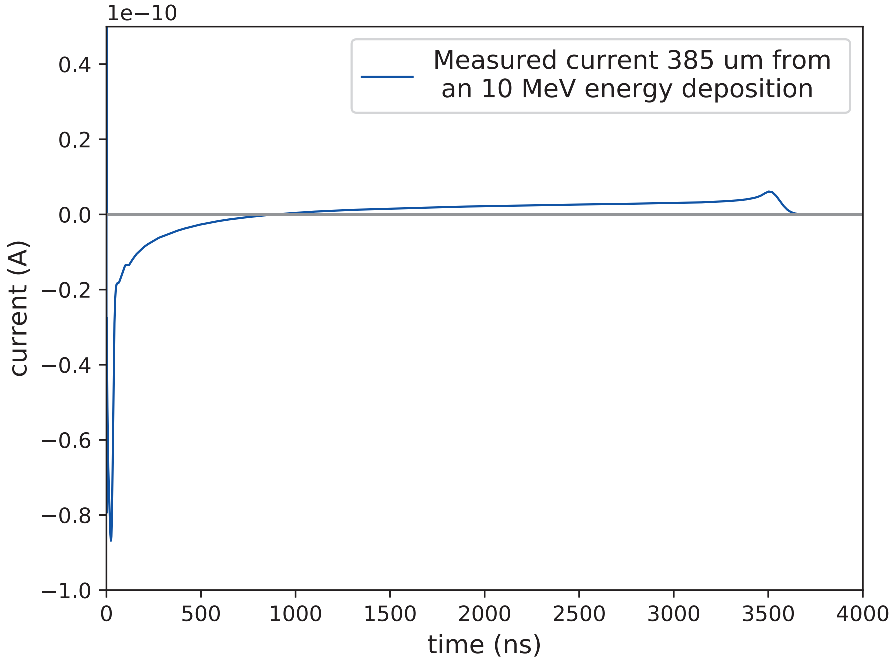

Figure 3.9.: Example of the current flowing in a pixel in the halo where the integrated charge is zero

Another consideration related to the plasma effect is that the longer collection time could increase the amount of recombination of electron/holes pairs. This could result in the detector not reading out all the deposited energy. To investigate this effect the charge loss due to recombination was simulated using TCAD for an energy deposition of 10 MeV and 50 MeV. According to figure 3.7 energy depositions of 10 MeV is frequently found in the center of the cluster, while depositions above 50 MeV are very unlikely. Using TCAD no measurable charge loss is found for an energy deposition of 10 MeV, while for an energy deposition of 50 MeV 95% of the charge is collected. Since the effect of recombination due to long collection time is quite small, charge loss due to recombination is not consideration in this particular detector response model. It will also be shown in the next section that pixels receiving high energy depositions suffer from the volcano effect, and this effect would overthrow any small recombination effect.

In conclusion, the plasma effect caused extra charge sharing between pixels and this has to be taken into account in the detector response model. It also causes increased amount of recombination, but for antiproton annihilations the effect is to small to take into consideration.

3.4.3. Volcano effect and saturation

The volcano effect is a disturbance in the readout when a pixel experiences a large energy deposition. It causes a single pixel to read out a random lower energy deposition instead of the amount actually collected at the electrode. The effect has been seen in several experiments [38, 39, 40]. The exact explanation is not completely known, but recent studies suggest that the volcano effect is compatible with the fact that the Timepix readout chip is

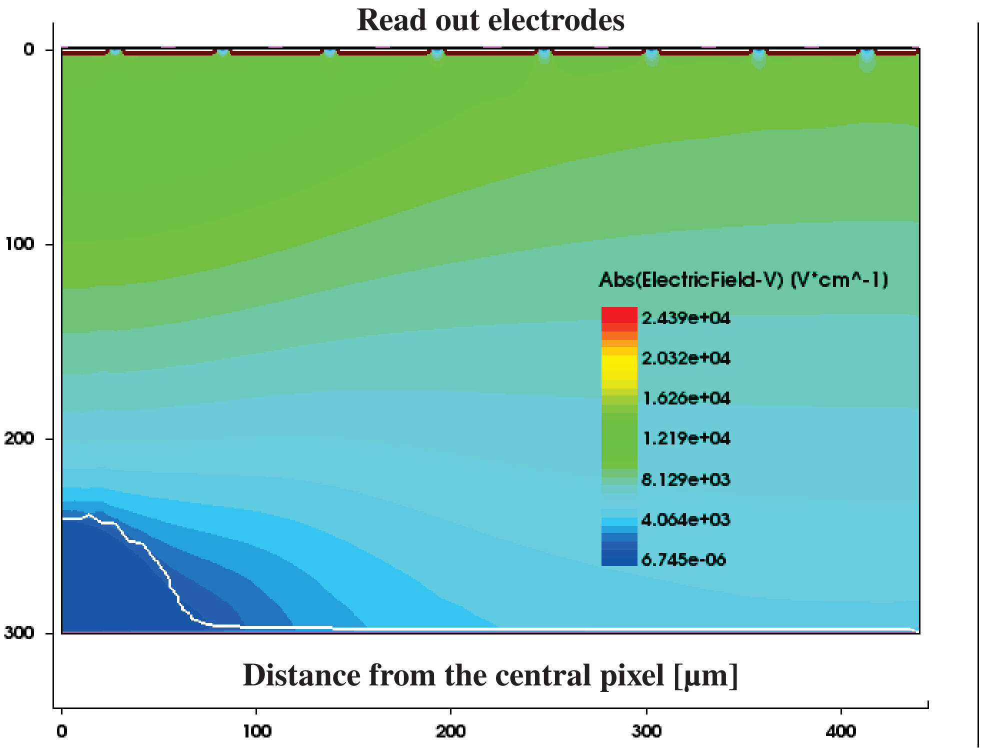

Figure 3.10.: The field in a 300 µm thick silicon detector experiencing an energy deposition of 22.5 MeV in the center pixel. The white line shows where the depletion zone extends, and as seen the detector is not depleted around the large energy deposition due to the plasma effect.

equipped with an internal protection circuit for very high input charges [40].

One of the previous studies of the volcano effect contained quantitative information about the pixels in each cluster that had the highest read energy depositions [38], and is therefore interesting since it can be compared to the antiproton data. The study was carried out at the Heavy-Ion Medical Accelerator (HIMAC), in Chiba, Japan. Here high energy heavy ions of type O, Ne, Ar, and Fe with energies between 230 MeV/A and 526 MeV/A were impinging on a 300 µm thick Timepix3 detector. Comparison between the data and theoretical predictions showed that between 40 % and 93 % of the energy was not read out, the exact fraction depended upon the particle type and its energy. In a single pixel the read-out energy never exceeded 600 keV. Taking the pixel with the highest measured energy deposition in each cluster make up what from here on is referred to as the maximum pixel energy distribution. The maximum pixel energy distribution from the heavy iones at HIMAC seemed to followed a Gaussian-like distribution with mean around 500 keV, and standard deviation around 50 keV.

Due to the large and dense energy depositions caused by an annihilation it is expected that the volcano effect is also seen in the antiproton data. Figure 3.11 shows the maximum pixel energy distribution for the antiproton data. A peak at around 500 keV can be seen, and there are no entries above ≈ 650 keV. This seem to replicate the shape found in [38]. In the antiproton data in figure 3.11 entries at lower energies are also seen. This happens because not all clusters are caused by particles giving high enough energy depositions for the volcano effect to kick in.

In figure 3.11 there is no sharp cutoff, this indicates that there is no sharp onset in terms of the energy deposition for the volcano effect to be present. There is a peak at around 500 keV, and the explanation for this peak is probably that pixels suffering from the volcano effect takes a value around 500 keV instead of the value corresponding to the actual deposited energy.

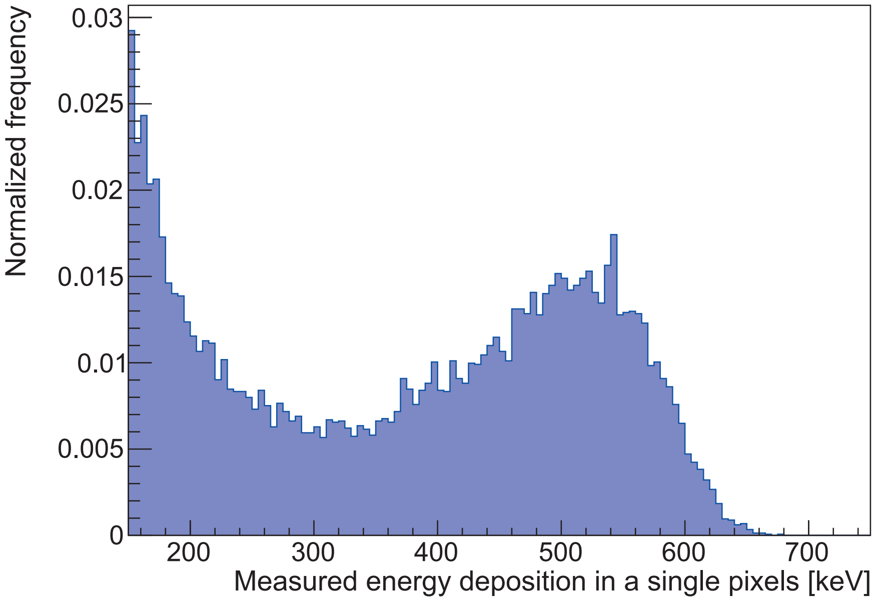

Figure 3.11.: The maximum pixel energy distribution for the antiproton data. The distribution is made by finding the pixel with the highest deposited energy from each cluster in the data. The peak around 500 keV seems to replicate what was seen in [38] were the volcano effect was studied with high energy ions.

3.5. Summary and conclusion

From theory one knows that an antiproton annihilating with a nucleon mainly creates pions. The branching ratios into different pionic configurations is not theoretically known, but has been experimentally determined. When the antiproton annihilates with a nucleon belonging to a nucleus, some of these pions are likely to penetrate the nucleus and break it into fragments. In a pixel detector this gives rise to a star shaped signature if the fragments travels sufficiently long in the bulk of the detector.

Both FLUKA and Geant4 are simulation tools that can be used to simulate antiproton annihilations in material, however their predictions differs quite a lot. None of them shows perfect agreement with experimental data, but FLUKA is the closest. Due to this uncertainty in the simulation software, results from the detector response model developed in this thesis is whenever possible supported by results based only or mainly on data.

The annihilation of antiprotons causes large energy depositions mainly in the center of the cluster. The large energy depositions give rise to three peculiar effects in the detector: the halo hits, the volcano effect and the plasma effect. These effect will be taken into consideration when developing the detector response model in chapter 6.

4. The GRACE beam line: A new beam line to extract low energy antiprotons

The GRACE beam line [35, 41] is a secondary beam line to the AEgIS experiment, and a picture of the beam line can be seen in figure 4.1. This beam line is designed to provide antiprotons of low kinetic energy, while minimizing the background produced by antiprotons annihilating prior to the detector.

The GRACE beam line was used for the study of the 675 µm thick Timepix3 detector. This detector is described in chapter 2, and the results of that detector study are presented in chapter 5, 6 and 7.

This chapter first presents the GRACE beam line and the full simulation of it. The simulation is then used to gain insight into how the energy and flux of the beam varies with different settings on GRACE. This provides valuable information for planning further experiments and detector tests on this beam line.

4.1. Motivation for building the GRACE beam line

The GRACE beam line was first built to improve the experimental conditions for testing detectors for antiproton annihilations. Previous tests with a Timepix3 detector was done

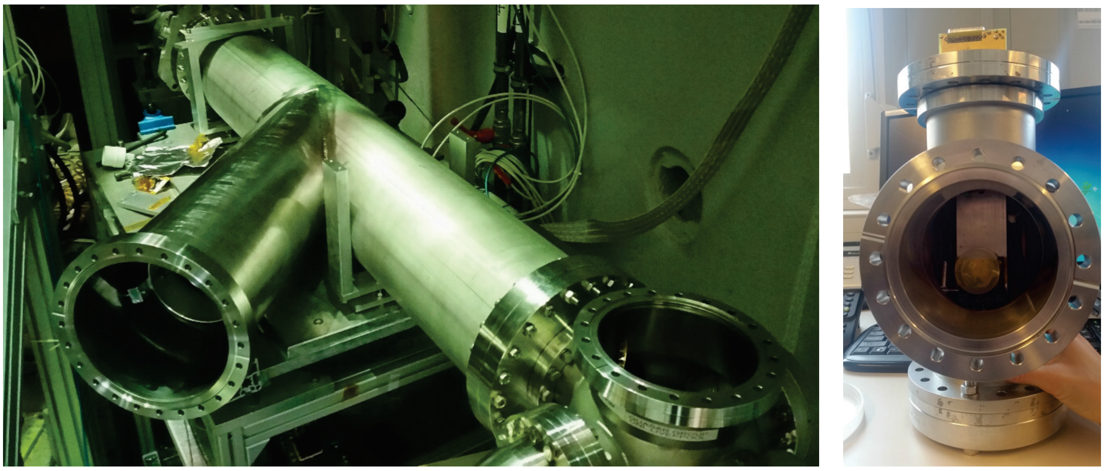

(a) The GRACE beam line as it was mounted on the extraction point of the AD. The device under test (for instance a Timepix3 detector) is installed in a vacuum chamber that is mounted on the open flange on the left.

(b) The chamber with the mounted Timepix3 detector to be installed at the open flange on the left in figure 4.1a.

Figure 4.1.: Photo of the GRACE beam line with the vacuum chamber disassembled.

using a simple vacuum chamber as described in section 3.3. As seen in figure 3.5 the detector was quickly saturated after the first few antiprotons hit the detector, and therefore a lot of data was lost. Because the detector saturated, only the first few antiprotons to hit the detector could be used for analysis, and this is problematic because the annihilation depth of these first antiprotons is to high.

In the final gravity experiment the energy of the antihydrogen beam will be in the order of eV, and therefore the annihilations will happen at the surface of the detector. Figure 4.2 shows the simulated energy distribution of the beam as it enters the vacuum chamber, and as seen the energy distribution is very broad. This means that the first few antiprotons to arrive at the detector had a kinetic energy above 500 keV, corresponding to an annihilation depth of 6 µm in silicon [42].

The GRACE beam line can selects out only the low energy antiprotons, and as a result the flux is also reduced. The settings applied to GRACE when retrieving the data from the 675 µm thick Timepix3 detector ensured that the antiprotons had en energy below 6 keV. The penetration depth for a 6 keV antiproton in silicon is below 0.2 µm [42], and this is a much more similar situation to the final experiment than a penetration depth of 6 µm which was the situation before the GRACE beam line was built. A silicon detector will always have an oxidation layer or be metalized on the surface. Therefore different annihilation depths gives different material for the antiprotons to annihilate in. The annihilation material might influence the annihilation clusters since different material gives different annihilation fragments.

In conclusion the GRACE beam line improves the experimental conditions first by providing lower flux such that the Timepix3 detector does not saturate. Secondly it provides antiprotons with low kinetic energy such that the annihilation depth is more similar to what is expected in the final gravity experiment.

Another important motivation for building the GRACE beam line was that it can be run in parallel with the AEgIS experiment as a test facility. During the test beams in 2015 and 2016, a switching magnet directed spills of antiprotons not needed by AEgIS into GRACE. The switching of the beam makes it possible to test components of the final gravity experiment independent of the status of the main AEgIS experiment.

The plan for AEgIS is to continue to use the GRACE beam line for detector tests, testing prototypes of the moiré deflectometer and possibly set up other small experiments where low energy antiprotons are needed.

4.2. Experimental setup

AD delivers spills of $\approx 3 \times 10^7$ antiprotons with a kinetic energy of 5.3 MeV to the GRACE beam line about every 100 seconds. An illustration of the GRACE beam line is shown in figure 4.3. The extraction line of GRACE is inclined 40° with respect to the main line of the chamber. The beam line is build up of two of einzel lenses [43] that focuses the antiprotons without altering their energy. The einzel lens right after the GRACE vacuum window is named E_1, while the one on the inclined line is named E_2. Two bending electrodes are present to direct the low energy antiprotons towards the detector. The small rounded electrode is named D_1 and is always grounded to zero potential. The lower longer one is named D_2. In order to bend the low energy antiprotons into the extraction line electric potential was applied to this electrode.

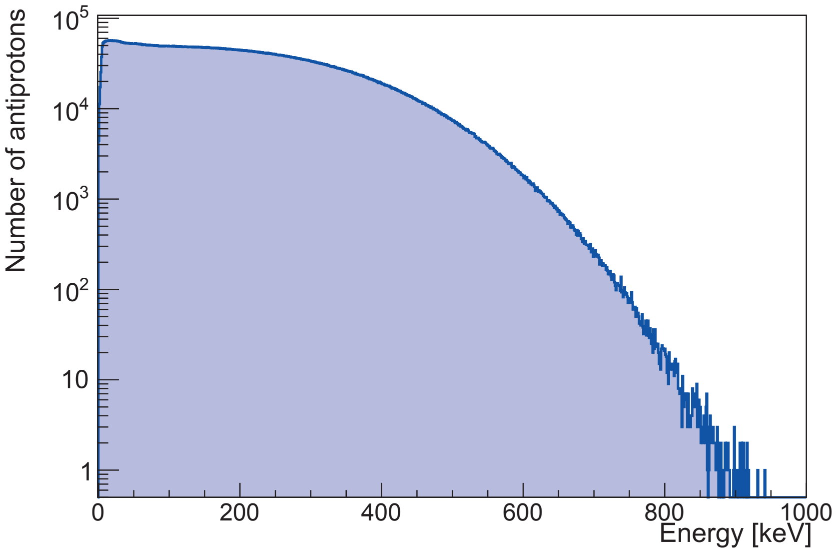

Figure 4.2.: The simulated energy distribution of one spill of antiprotons from the AD as they have passed the entrance window to GRACE or passed the entrance window to the simple vacuum chamber that is described in section 3.3. These two distributions are the same since the thickness of the vacuum windows and the air gap are the same in the two setups. In this simulation the thickness of the variable aluminum degrader is 33 μm.

The GRACE vacuum window has a diameter of 4.0 cm and consist of 25 μm titanium. There is a 6.5 cm air gap between the AD vacuum window and the GRACE vacuum window, and this air gap plus the two vacuum windows reduce the energy of the beam. To reduce the energy even more an aluminum degrader of variable thickness is placed in the air gap. Every time the GRACE beam line has been moved the thickness of this degrader is scanned to find the setting giving the most antiprotons on the detector. If the degrader is too thin, none of the antiprotons will have low enough energy to be bent towards the detector. If on the other hand, the degrader is too thick, all the antiprotons will annihilate in the degrader.

Depending on the detector and its support structure, the detector can be placed anywhere in the plane where the detector is shown to be mounted in figure 4.3. This area is from here on called the detector plane. During the data taking the detector was placed around 2 cm down from the center of the detector plane, as seen in figure 4.1b. It should be mentioned that this is a rough estimate taken from pictures of the setup.

In principle any potential between 0 and 10 kV could be applied to the electrodes. However, it was experienced that the power supply was shutting down when voltages higher than 4 kV were applied, probably due to bad connectors between the power supply and the electrodes. Since new high voltage connectors were not available during the test beam period only configurations using electrode potentials below 4-5 kV could be tested.

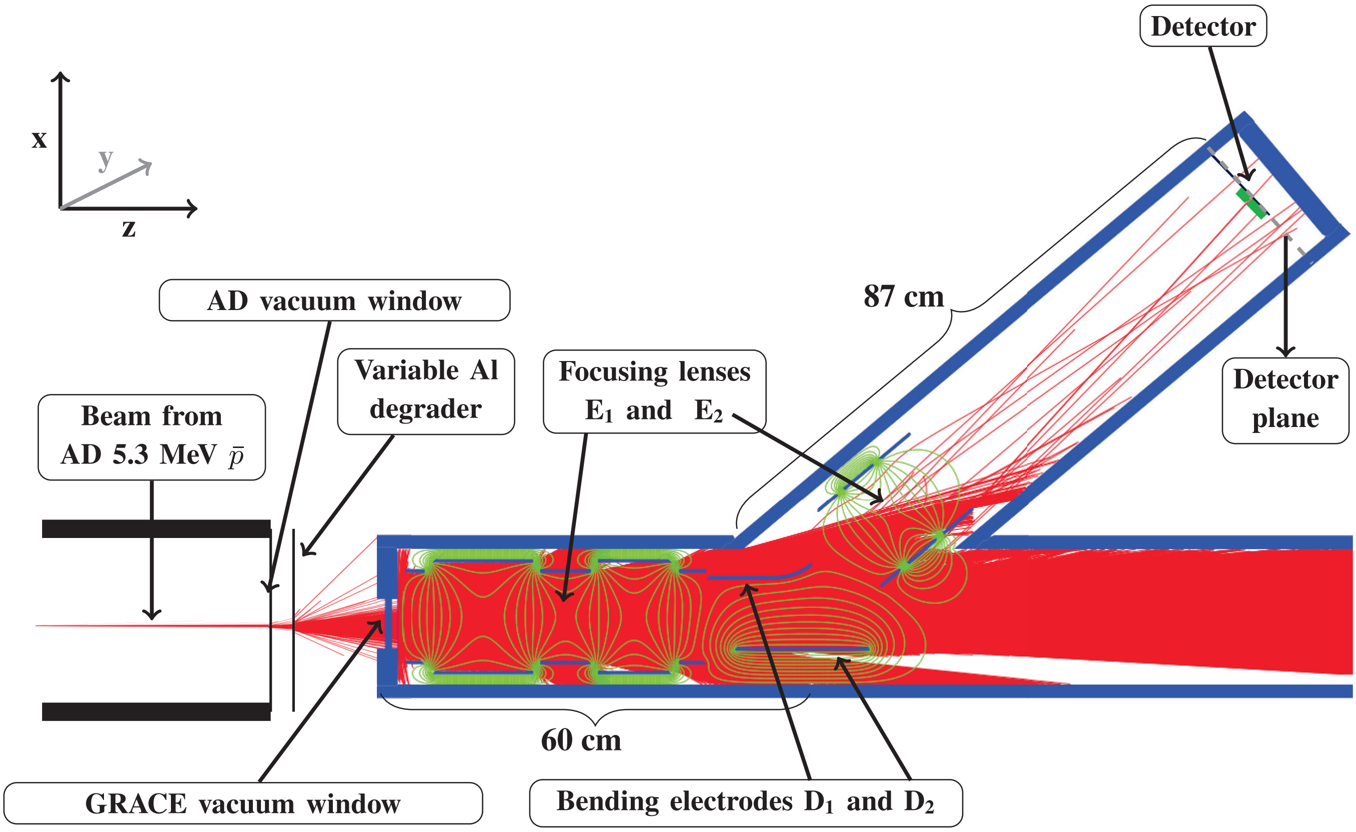

Figure 4.3.: Illustration of the GRACE beam line. The antiproton beam of 5.3 MeV arrives from the AD, looses energy and is scattered in the vacuum windows, the variable degrader, and the air gap between AD and GRACE. The bending electrodes are used to select antiprotons with low energies and direct them towards the detector. This figure is not to scale.

4.3. Simulation of the GRACE beam line

For the work of this thesis a full simulation of the GRACE beam line was developed. The simulation is done in two steps, as presented in the two following subsection, and can be used to predict the flux and energy of the antiprotons in the detector plane. The first step is to simulate the incoming beam to GRACE, and for this purpose a simulation program named **DegraderSimu** was developed. The antiprotons also need to be tracked through the GRACE apparatus, and for this purpose a simulation program named **GRACESimu** was developed. Technical documentation with details of the programs and instructions for setting up and running these two programs are provided in appendix A and B.

4.3.1. **DegraderSimu**: Simulation of incoming beam using Geant4

The beam from AD loose energy and is scattered in the AD window, the air gap between AD and GRACE, the variable aluminum degrader, and the vacuum window of GRACE. The **DegraderSimu** program simulates the energy loss and scattering of the beam in these three foils using the Geant4 [22] framework, and is documented in appendix A. In the simulation the beam from the AD is represented as a point beam of energy 5.3 MeV, since the beam distribution in the transverse phase space, as well as the beam energy spread as it enters GRACE, is dominated by the interactions in the foils. The output of the simulation is the position and momentum of the antiprotons right after they have entered GRACE through the GRACE vacuum window.

For this simulation the thickness and material of the AD vacuum window must be known. This window was installed for the ACE experiment that started in 2003, more than 15 years ago, and there is deviating information about the material and thickness of the window. Since measuring its thickness would include breaking the vacuum to the AD, this was not an option. While an article [44] from the ACE experiment states that the window is made of 15 µm titanium, technical documentation states that it is 50 µm titanium while the general thickness and material of all other vacuum windows at AD is 50 µm stainless steel [45]. As will be shown in section 4.5.1 it was experimentally found that the thickness of the variable aluminum degrader giving the maximum flux is between 33 and 35 µm. It was also found that an aluminum degrader thickness above 38 µm or below 25 gave no antiprotons on the detector. These results are as expected for an AD window consisting of 50 µm stainless steel. If one assumes that the AD window is made of 50 µm titanium, the simulation predicts that the thickness of the variable degrader providing maximum flux is around 80 µm. For these reasons it is assumed that the AD vacuum window is made of 50 µm stainless steel, and this is therefore implemented in the final version of **DegraderSimu**.

4.3.2. **GRACESimu**: Tracking the antiprotons through GRACE

The **GRACESimu** program tracks the particles through the electrostatic optics of the GRACE beam line. It is written in C++ and uses the IBSimu library [46]. The input to **GRACESimu** is the beam as it enters into GRACE, meaning its input is the output from **DegraderSimu**. The output of **GRACESimu** is the position and energy of the particles that ends up in the detector plane. An initial proof of principle version of this simulation was developed by the summer student Gerry Lawler, and was used to provide rough guidelines for the geometry of GRACE [35]. The **GRACESimu** program is a more detailed version of is predecessor and implements the exact geometry of GRACE. It is also thoroughly debugged and tested against data as will be shown in section 4.5.

Figure 4.4 shows the electric field between the two bending electrodes according to this simulation, and as seen the field is not uniform. This also shows that any analytic analysis of the GRACE beam line using infinite plate approximation would not be sufficient, as that would predict a uniform field between the electrodes. For this reason it was important to make a full simulation of the GRACE beam line.

4.4. Data analysis

The interesting parameters for evaluating the GRACE beam line is the flux and energy of antiprotons on the detector for different settings. A setting is defined as the combination of potentials on the electrodes, and the thickness of the variable aluminum degrader.

According to the simulation the flux of particles do not have a completely uniform distribution in the detector plane. Figure 4.5 proves this by showing the spatial distribution of the antiprotons hitting the detector plane for a bending voltage of 3 keV and focusing voltages corresponding to the scans that will be discussed in section 4.5. The projection is in the eye of the deflected beam, and the y direction is the same as in figure 4.3. The corresponding

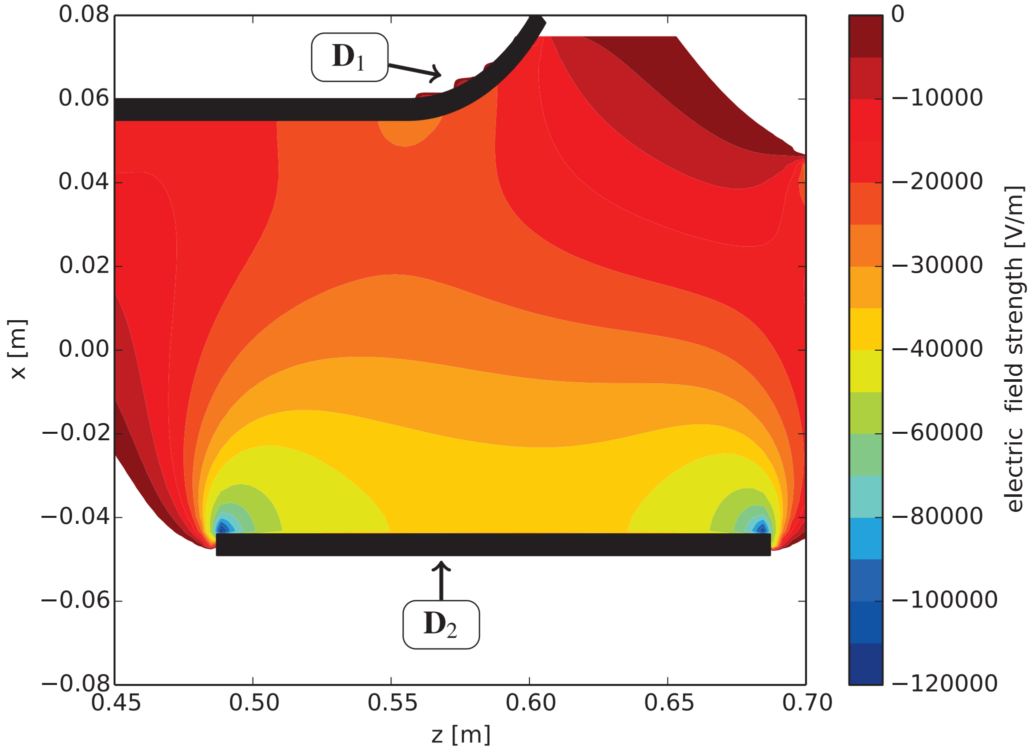

Figure 4.4.: Electric field between the two bending electrodes in GRACE showing that the field between the electrodes is not uniform. This shows the importance of making a full simulation as any analytic solutions using an infinite plate approximation would not be sufficient.

profile plot shows how the kinetic energy also varies over the detector plane in the x direction. No such variation was found in the y direction, which makes sense since the whole beam line is symmetrical in this direction.

The spatial variation of the flux means that a small misalignment in the GRACE apparatus or a small displacement of the detector might alter the flux. For the data only a rough estimate of the position of the detector exists, it was placed approximately 2 cm off center in the y direction. For these reason both the flux at the estimated detector position and the average flux per detector area of 1.408 cm^2 is calculated when estimating the flux from the simulated data.

The data used for the verification of the simulation was obtained during test beam in 2015 and 2016. These data were mainly used to develop the tagging and vertex fitting algorithms that are the main content of this thesis. At the start of the test beam period a degrader scan and a scan of different voltages on the einzel lenses was performed in order to find a good configuration to obtained the antiproton data. It was later seen that these scans could be used to verify the simulation of the GRACE beam line, and this is done in section section 4.5.

To analyze the test beam data the tagging algorithm presented in [47] and in chapter 5 and 6 is used. This tagging algorithm has a tagging efficiency of 50% and a false tagging rate below 1.1%, given cuts of at least one prong and at least 70 pixels in the cluster.

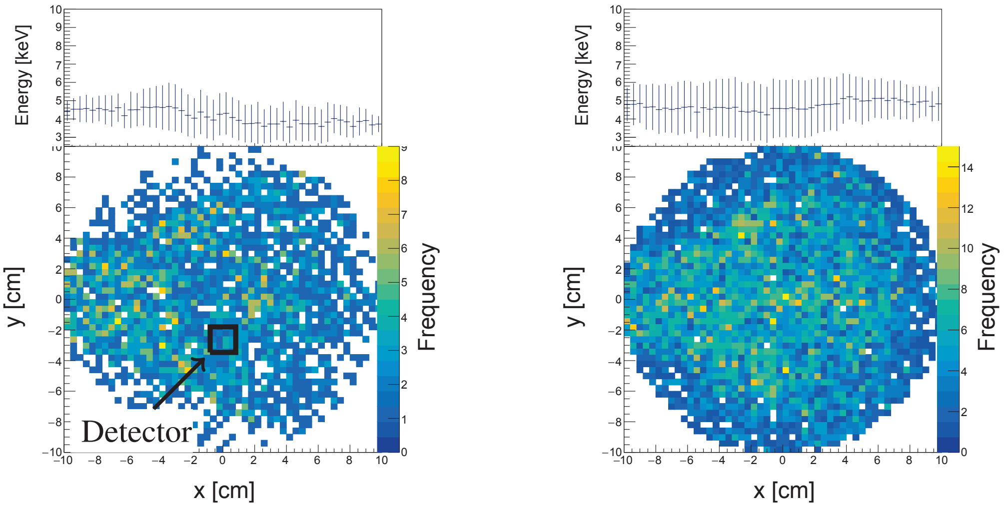

(a) D_1=0, D_1=3 kV, E_1=1 kV, E_2=3 kV

(b) D_1=0, D_1=3 kV, E_1=2 kV, E_2=3 kV

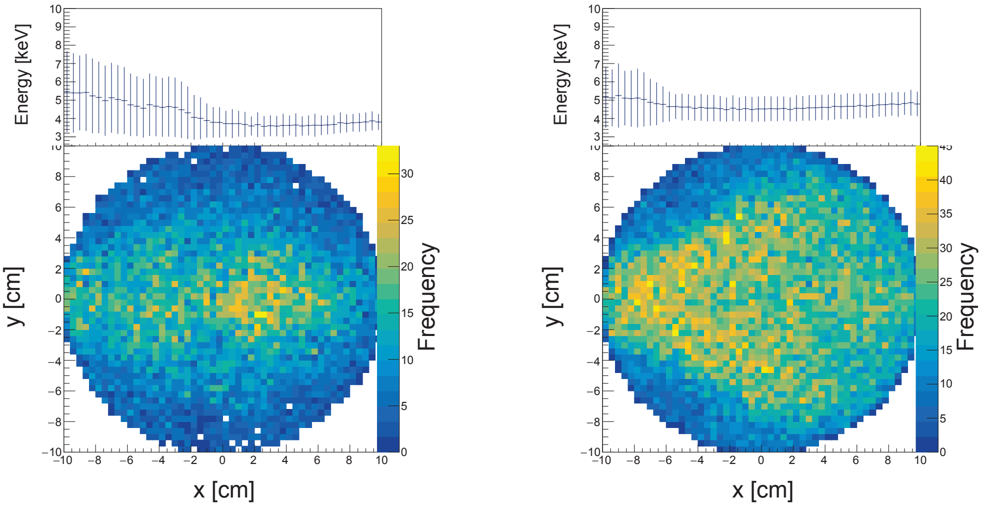

(c) D_1=0, D_1=3 kV, E_1=3 kV, E_2=3 kV

(d) D_1=0, D_1=3 kV, E_1=4 kV, E_2=3 kV

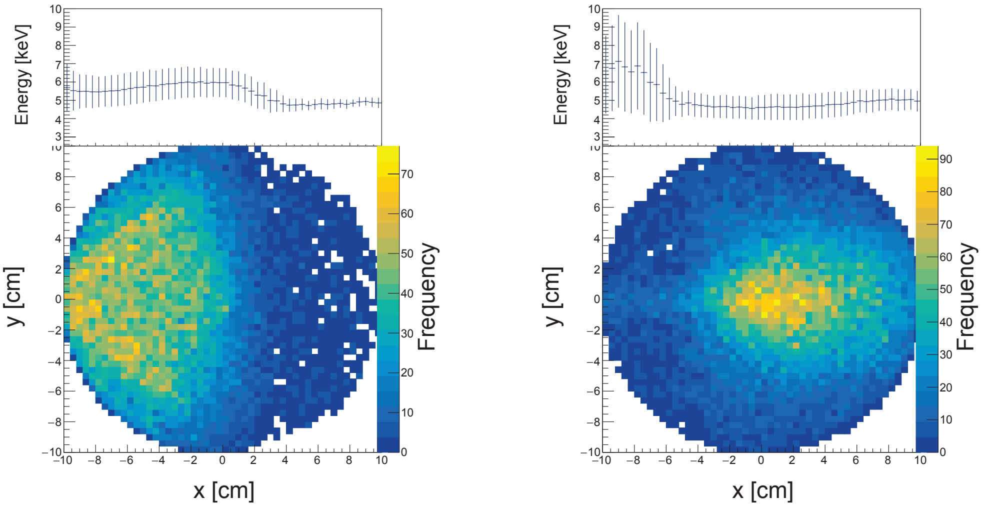

(e) D_1=0, D_1=3 kV, E_1=5 kV, E_2=3 kV

(f) D_1=0, D_1=3 kV, E_1=4 kV, E_2=4 kV

Figure 4.5.: Simulated examples of the flux distribution in the detector plane and the profile plot of the kinetic energy distribution of the antiprotons in the x-direction. The profile plot shows the average and sample standard deviation of the kinetic energy. Neither of the distributions are completely uniform. In figure 4.5a the approximate position of the detector is indicated.

The possibility to compare simulation against data revealed that the energy loss model of Geant4 stepped into a singularity when their single scattering model was used at low energies. This bug was resolved in collaboration with the Geant4 team and the solution was implemented from release Geant4.10.4 [48].

4.4.1. How to compare kinetic energy between data and simulation

The travel time for an antiproton in GRACE, meaning the time it takes for it to travel from the entrance of GRACE and to the detector plane, depends upon the kinetic energy of that antiproton. In the simulation this travel time is known for each individual antiproton. In the data the travel time needs to be estimated as there is no trigger for when the beam enters into GRACE. It is possible to make this estimate because the majority of the antiprotons annihilate without being bent towards the detector, and because the fragments produced on and around the bending electrodes have a free path to the detector.

The secondary fragments from annihilations around the bending electrodes will arrive at the detector before the antiprotons. This happens because the annihilation products has a much higher kinetic energy than the antiprotons that are being bent towards the detector. According to FLUKA [23], the average kinetic energy of the annihilation products is 90 MeV. For an alpha particle this corresponds to a travel time from the bending electrodes to the detector of only 14 ns. As shown in chapter 3, most of the annihilation produces were lighter and therefore have even shorter travel time for the same kinetic energy. For comparison the travel time in GRACE for a 5 keV antiproton is 1400 ns.

The shower of secondary fragments and the delayed antiprotons can be clearly seen in figure 4.6, which shows the time of arrival (ToA) in the detector in all pixels from one spill of antiprotons. The histogram has two peaks. The first peak is caused by fragments from annihilations close to the bending electrode, while the second peak contains the antiprotons together with fragments and pions from annihilations closer to the detector. The substructure of the second peak is caused by some of the clusters being very large, and therefore one cluster might by itself appear as a peak in the histogram. When integrating over all the spills, as will be shown in figure 5.1 in chapter 5, these substructures disappear.

The travel time for an antiproton is estimated by first making the same histogram as shown in figure 4.6 for the relevant spill from AD and find the ToA of the first peak. Then the travel time is estimated as the difference between this ToA value and the average ToA in the pixels making up the annihilation cluster, and then adding 100 ns. The 100 ns is added because it takes on average 100 ns for the antiprotons that annihilate around the bending electrodes to travel from the the entrance of GRACE to their annihilation point. This is only a small correction, as the time difference between the two peaks is in the range of 1000–2000 ns for the data studied in this chapter.

As explained in section 1.2 the longitudinal spread of the spill of antiprotons out of AD is around 200 ns and this gives an uncertainty to the estimated travel time. This is taken into account by adding a random number from a flat distribution between -100 ns and 100 ns to the travel time for each antiproton in the simulated data.

4.5. Comparison between data and simulation

This section presents the comparison between data and simulation in order to verify the simulation and estimate its predicting power. First the flux as a function of the variable

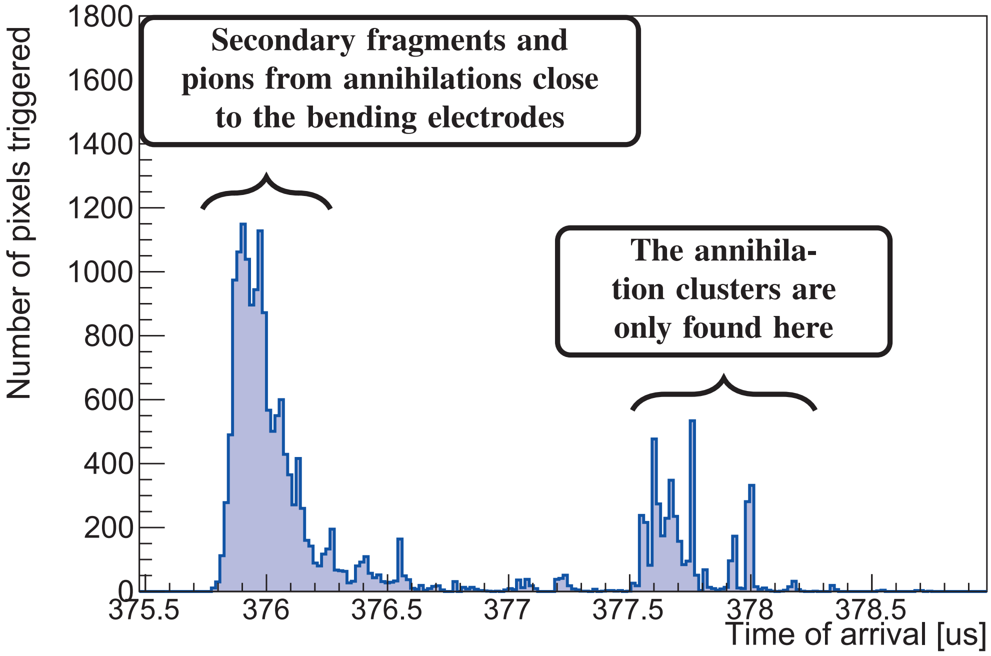

Figure 4.6.: The Time Of Arrival (ToA) of the pixels as they arrive at the detector for one spill of antiprotons. The mode of the first peak is used to find the time the antiprotons enters into GRACE. The substructure of the second peak is probably because some of the clusters are very large and therefore by them self appear as a peak in the histogram.

aluminum degrader thickness is studied. Then both the flux and kinetic energy of the antiprotons are compared for the scans of different applied potentials to einzel lenses.

The last subsection explains why the potential on the einzel lenses affected the energy distribution of the antiprotons in the detector plane. This was quite unexpected since an einzel lens by itself should only focus the beam and not alter its energy [43].

4.5.1. Scanning the variable aluminum degrader thickness

The thickness of the variable aluminum degrader determines the energy distribution of the particles into GRACE, and is therefore an important parameter for the flux on the detector. A scan of degrader thicknesses was performed in the setting D_1=0, D_2=3 kV, E_1=4 kV and E_2=4 kV, as this setting seem to give the highest flux without the power supply shutting down. The scan was performed in steps of 2-3 µm depending on the aluminum foils available, and the result is shown in figure 4.7. As seen the comparison is quite good, although not perfect. The statistical error on the mean of the measured flux is always below 0.3, and is therefore not visible in the plot. At the time when the degrader scan was performed, the tagging algorithm had not been developed and the flux was estimated by eye. Therefore the best degrader was assumed to be 33 µm and this thickness was therefore used for the rest of the data taking. Since saturation due to excessive amounts of antiprotons did not appear to be a problem, it was chosen to use the setting providing the assumed highest flux to get as much

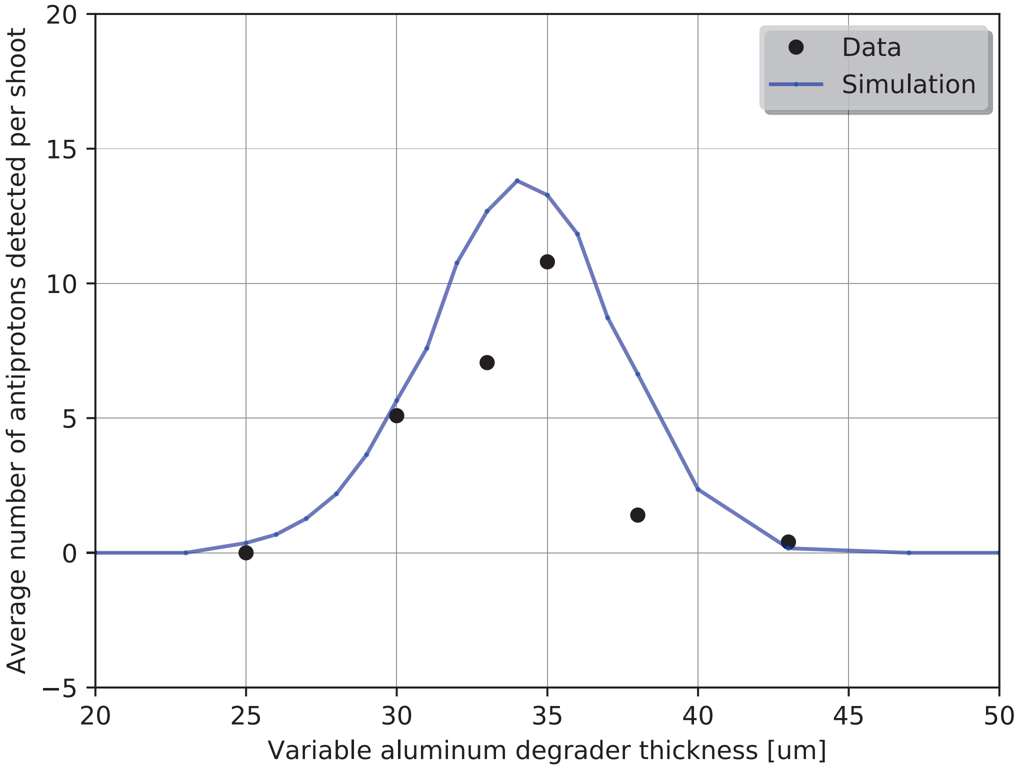

Figure 4.7.: Comparison between simulation and data for the scan of the variable aluminum degrader. This scan was done to find the thickness of the variable aluminum degrader giving the maximum flux of antiprotons on the detector.

useful data as possible.

4.5.2. Scanning the focusing lenses

The effect of the focusing lenses on the flux was systematically tested for two different voltages on D_2, first with D_2 =3 kV and then with D_2 put down to 1.5 kV. The results are found in table 4.1, and the settings giving the highest flux for each of the scans are marked in blue. The simulation is able to predict the flux quite well, the discrepancy is always below ± 30%. The only exception is the setting D_1=0, D_2=3 kV, E_1=4 kV, and E_2=4 kV, where the simulation overestimates the flux. This is also the only setting where there is a large difference between the average flux on the detector plane and the flux at the estimated detector position. Therefore it is possible that the discrepancy is caused by a small misplacement of the detector or the GRACE apparatus.

The negative numbers in the data occur since the estimated amount of falsely tagged antiprotons is subtracted. Negative numbers only occur when the predicted flux is very low, and is probably because the tagging efficiency of 1.1% might be slightly overestimated, this is discussed in section 6.3.1.

Setting on GRACE				**Data**		**Simulation**	
D$_1$	D$_2$	E$_1$	E$_2$	Tagged antiprotons on detector	Sample standard deviation	Tagged antiprotons per detector area	Tagged antiprotons on detector
0	3 kV	0	3 kV	1.7	2.1	0.72	0.95
		1 kV		1.1	0.3	1.03	1.20
		2 kV		4.0	0.6	2.50	2.85
		3 kV		6.9	1.6	6.05	8.65
		4 kV		15.5	3.0	12.64	18.20
		5 kV		16.8	3.4	12.66	17.20
0	3 kV	4 kV	0	6.3	2.0	5.93	6.05
			1 kV	6.3	2.2	6.16	6.10
			2 kV	6.8	0.8	7.47	7.05
			3 kV	15.8	3.0	12.64	18.2
			4 kV	7.1	1.5	12.68	32.15
			5 kV	(no data)		8.48	15.10
0	1.5 kV	0	3 kV	-0.7	0.2	0.50	0.15
		1 kV		0.7	1.9	0.17	0.00
		2 kV		2.0	1.9	2.37	1.05
		3 kV		0.6	0.4	2.40	1.15
		4 kV		-0.2	0.3	0.96	2.50
		5 kV		(no data)		0.44	0.80

Table 4.1.: Comparison between data and simulation for the the flux on the detector. The settings giving the highest flux in data for each of the scans are marked in blue. See table 4.2 for estimated energies in different settings.

4.5.3. Time of arrival

The comparison between data and simulation for the travel time in GRACE is shown in figure 4.8. The travel time is estimated by the method described in section 4.4.1. The histograms are shown for the settings giving the highest flux as marked out in table 4.1. As seen the comparison is in general quite good, and the travel time is as expected considerably longer for D_2=1.5 kV than for D_2=3kV.

According to the simulation the kinetic energy of the antiprotons in the setting with D_2= 3 keV is in the area of 3 to 6 keV, and this bending voltage was used when obtaining the data for the analysis shown in chapter 5. In the setting with D_2=1.5 keV the kinetic energy is in the area of 2 to 5 keV.

4.5.4. The effect of the focusing on the energy distribution

Figure 4.9 shows the effect of the focusing on the travel time, in both real and simulated data. Plots are only shown for the settings where D_2 is 3 kV as this bending voltage gave high enough flux to clearly see the time distribution for several different settings on E_1 and E_2. As seen the amount of focusing on E_1 changes the energy distribution of the antiprotons reaching the detector plane. The magnitude of E_2 does not seem to have this effect. The effect is present in both data and simulation, and is quite unexpected as an einzel lens should only focus the beam and not change the energy of it [43].

The reason is that even though einzel lens E_1 does not change the energy of the antiprotons, it is selective of which energies it manages to focus. The effect of this is illustrated in figure 4.10 where the simulation is used to track only the 200 antiprotons with the highest kinetic energy that reach the detector plane in the setting D_1=0, D_2=3 kV, E_1 =5 kV and E_2 =3 kV. Figure 4.10a shows the paths in this setting, and the antiprotons reach the detector plane. In figure 4.10b the same particles entering GRACE are tracked, but now a focusing potential of only 3 kV is applied on einzel lens E_1. As seen those high energy antiprotons never make it to the bending electrode. They could be bent towards the detector by the field between the bending electrodes, but are lost before they get there.

In conclusion einzel lens E_1 changes the energy distribution of the antiprotons reaching the detector plane by managing to focus antiprotons with higher kinetic energy and get them to the area between the two bending electrodes.

4.6. Evaluating GRACE beam line

As seen in the previous section the simulation predicts the energy and the flux of the antiprotons reasonably well. It was also seen that the average number of tagged antiprotons in the setting giving the highest flux was around 16. This flux is good for detector tests, as it provides some clusters to analyze per spill, while the flux is still low enough for the detector not to saturate. However, for other possible applications of the GRACE beam line it would be beneficial to have higher flux of low energy antiprotons. For instance testing of the moiré deflectometer would require much higher flux than detector tests since more than 80% of the antiprotons annihilate in the gratings [49].

This section first uses the simulation to look into what can theoretically be achieved in terms of energy and flux, and then the simulation is used to investigate what is limiting the possibility to get even higher flux.

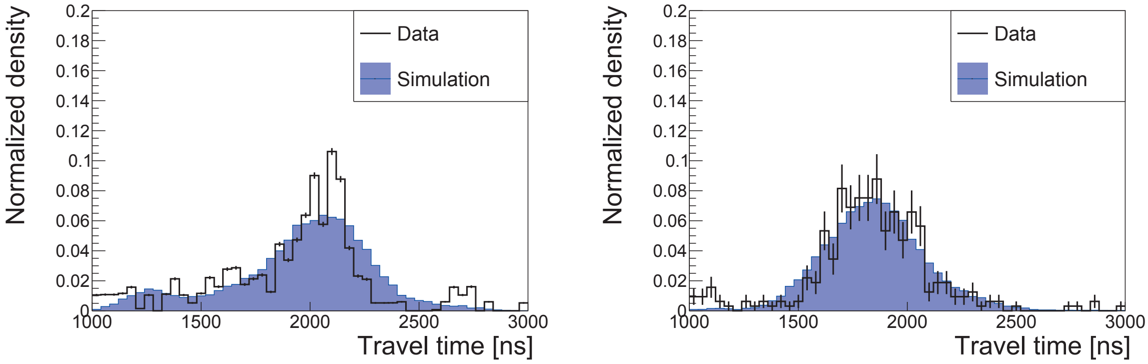

(a) D_1=0, D_2=3 kV, E_1=3 kV, E_2=3 kV

(b) D_1=0, D_2=3 kV, E_1=4 kV, E_2=3 kV

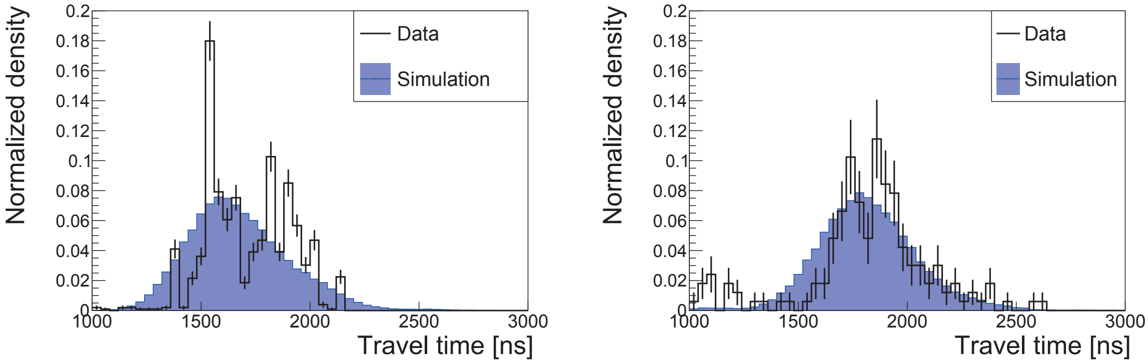

(c) D_1=0, D_2=3 kV, E_1=5 kV, E_2=3 kV

(d) D_1=0, D_2=3 kV, E_1=4 kV, E_2=4 kV

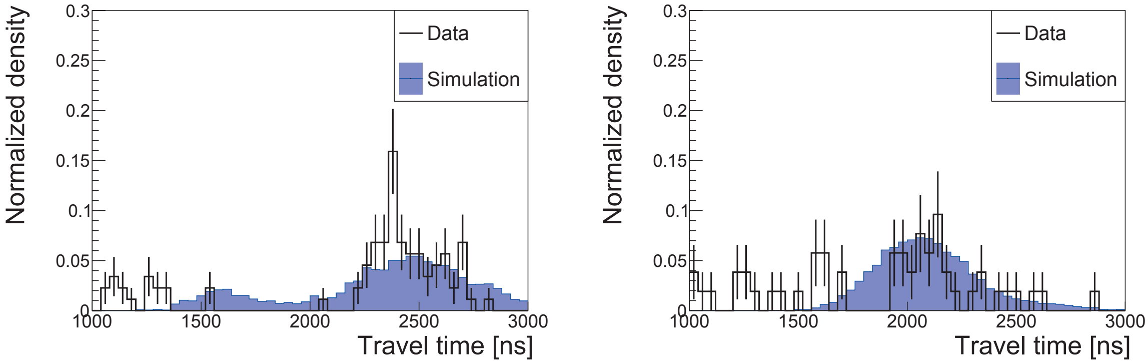

(e) D_1=0, D_2=1.5 kV, E_1=2 kV, E_2=3 kV

(f) D_1=0, D_2=1.5 kV, E_1=3 kV, E_2=3 kV

Figure 4.8.: Comparison between the time delay for data and simulations in the settings giving the highest flux in each scan.

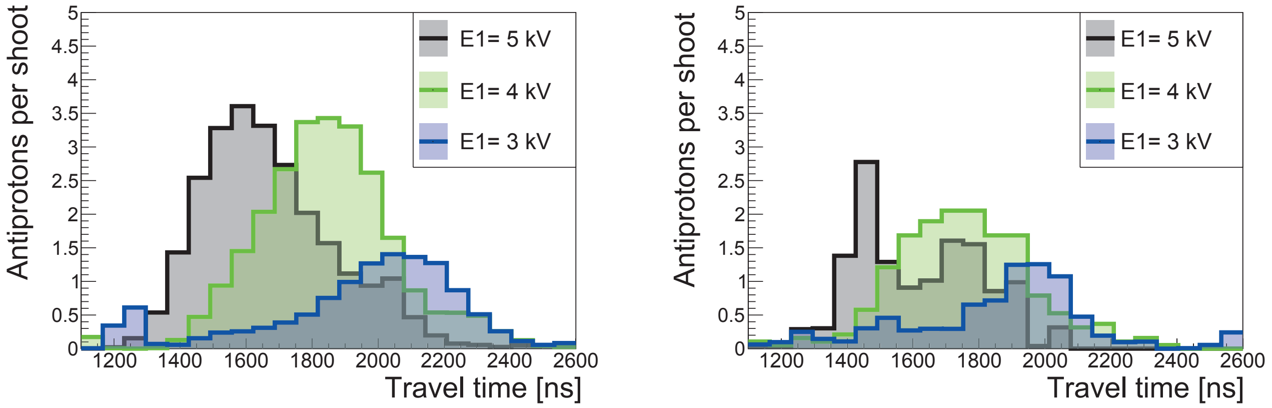

(a) Scan on E_1 simulated data with D_1=0, D_2=3 kV, and E_2 =3 kV.

(b) Scan on E_1 for real data with D_1=0, D_2=3 kV, and E_2 =3 kV.

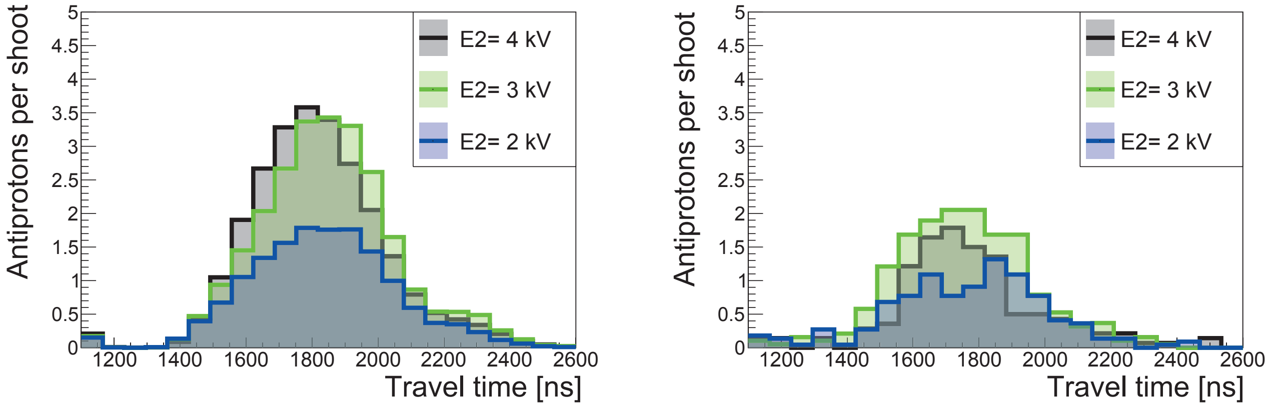

(c) Scan on E_2 for simulated data with D_1=0, D_2=3 kV, and E_1 =4 kV.

(d) Scan on E_2 for real data with D_1=0, D_2=3 kV,and E_1 =4 kV.

Figure 4.9.: The estimated travel time of the antiprotons in data and simulation for the scans on E_1 and E_2. Both in data and in simulation it is apparent that increasing the magnitude of E_1 decreases the travel time. The potential applied to E_2 does not seem to have this effect.

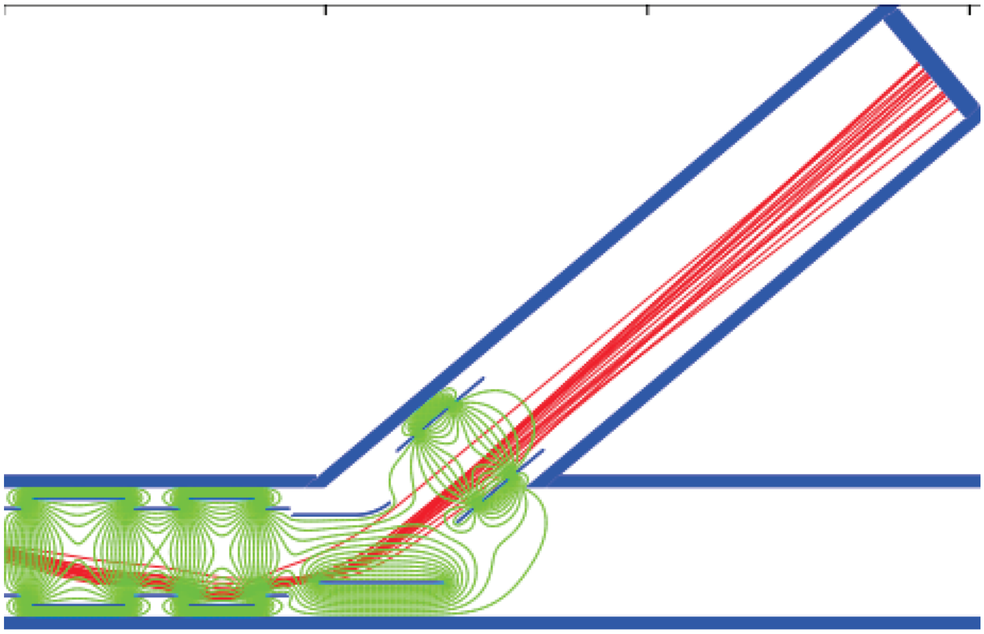

(a) The track of the highest energy particles that reach the detector with E_1=5 kV

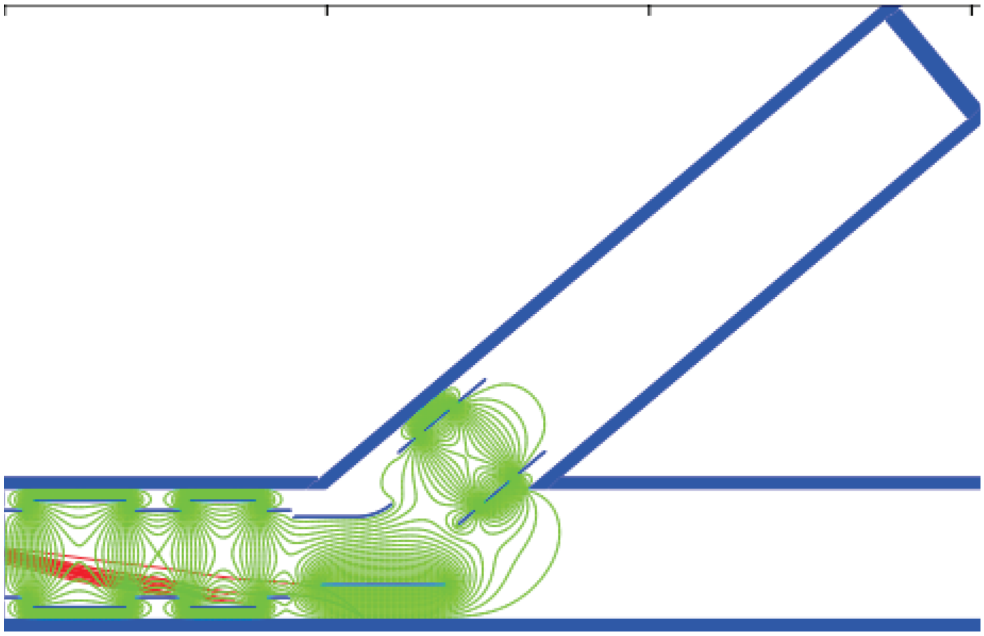

(b) The track of the same particles when E_1=3 kV

Figure 4.10.: The simulated tracks of only the 200 particles with highest kinetic energy that reach the detector in the setting D_1=0, D_2=3 kV, E_2=3 kV and E_1=5 kV. The particles with high energy that ends up in the detector plane follow a path where they hit a region between the bending electrodes with high enough field strength to bend them towards the detector.

4.6.1. Best settings for maximum flux and low energies

To find the settings providing the highest flux for different energy distributions in the detector plane a scan is made over all available voltages on D_2 in steps of 1 kV. For each value of D_2 the settings on the einzel lenses providing the highest flux is found and the resulting mean and standard deviation of the energy distribution in the detector plane is estimated. The results of this scan is found in table 4.2.

From the table it looks like a convenient rule of thumb that to obtain maximum flux for a given value of D_2 one should set E_1=D_2+2 kV and E_2=D_2+1 kV. It it also apparent that an increasing flux in the detector plane results in increased energy and less mono-energetic distribution in the detector plane. If a kinetic energy below 6 keV is required, it seems impossible to get much higher flux than around 15 antiprotons per cm^2.

Settings on bending electrodes		Best focusing		Flux in detector plane [$\bar{p}$/cm^2]	Mean energy of particles [keV]	Sample standard deviation of energy
D_1 [kV]	D_2 [kV]	E_1 [kV]	E_2 [kV]			
0	1	2	2	0.93	2.46	0.45
	2	4	3	5.94	4.67	0.75
	3	5	4	16.72	5.77	0.92
	4	6	4	26.82	6.91	1.13
	5	7	6	34.47	8.11	1.48
	6	8	7	40.24	9.25	1.70
	7	9	8	45.31	10.47	2.05
	8	10	9	51.06	11.65	2.39
	9	10	9	49.47	12.10	3.10
	10	10	9	63.36	13.97	3.12

Table 4.2.: A scan over all the possible values of D_2 is made in order to evaluate what GRACE can provide in terms of the flux and energy distribution of the antiprotons in the detector plane

4.6.2. Can the flux at low energies be improved?

Even when scanning over all possible configuration it seems difficult to get a very high flux, according to the simulation only 0.142 % of the antiprotons from AD ends up in the detector plane with the settings providing the highest flux. If a beam energy below $\approx$ 6 keV is required this number is reduced to 0.053%. It is therefore interesting to understand what is limiting the flux on the detector. Figure 4.11 shows histograms of the energy, position and momentum of the antiprotons as they enter GRACE. For each of the histograms, the part of the distribution belonging to the particles that make it in the detector plane is drawn in black. This means both histograms shows the distribution of the beam as it enters GRACE, but the black histogram shows just the particles that makes it to the detector plane. The histograms therefore shows the effect of the beam parameters (energy, position and momentum) on the flux in the detector plane.

From figure 4.11a it is clear that only a small amount of the incoming antiprotons has the energy range that GRACE can bend into the extraction line. Figure 4.11b and 4.11c shows the x and y position of the antiprotons as they enter GRACE. The shape of this distribution is almost the same for the particles ending in the detector plane and the incoming beam as a whole. This indicates that the exact position of the particles as they enter GRACE is not so important. In other words, carefully aligning the beam from the AD will not have a large effect as long as the majority of the beam actually hits the entrance window into GRACE. Figure 4.11d shows the deviation of the momentum vector from the z direction as defined in figure 4.3. Here it can be seen that the angular spread of the beam is quite large, and only the antiprotons that deviate from a straight path by less then 20° can end up in the detector plane.

In conclusion it is clear that the flux in the detector plane is limited by the beam entering GRACE having a large energy spread and being divergent. It is difficult to increase the flux in the current setup as the energy spread and divergence of the beam is caused by the way the energy is reduced by means of degraders.

4.7. Conclusion

GRACE was build to provide better experimental conditions for testing detectors for antiproton annihilations. For this purpose it has been very successful, as the majority of the data for this thesis was collected in the GRACE beam line.

A full simulation of the beam line has been made and it reproduces reasonably well the flux and energy of the particles in the detector plane. It was also able to explain the unexpected behavior that the energy distribution in the detector plane is influenced by the magnitude of the focusing.

During the data taking the highest flux was achieved in the setting D_1=0, D_2=3 kV, E_1=4 kV, and E_2=3 kV, when on average 16 antiprotons where tagged on the detector per spill, and their energy was between 3 and 6 keV. This condition was ideal for detector tests as the flux was high enough to get a useful sample within a couple of days of data taking, and even higher flux would probably make the detector saturate and reduce the amount of useful data.

For some applications of the GRACE beam line, for instance testing prototypes of the moiré deflectometer, it would be beneficial to have higher flux than for detector tests. Higher flux can be achieved if new connectors are installed such that higher potential can be applied on the einzel lenses and bending electrodes, but then the energy of the selected antiprotons will also increase. In the current setup it seems difficult to improve the flux at low energies as the flux is limited by broad energy distribution and the divergence of the incoming beam to GRACE.

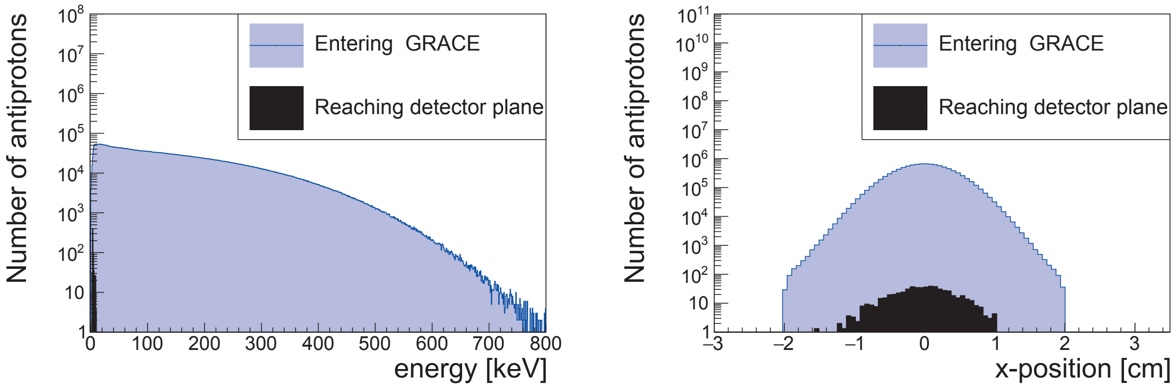

(a) Energy of the antiprotons as they enter GRACE

(b) X-position of the antiprotons as they enter GRACE

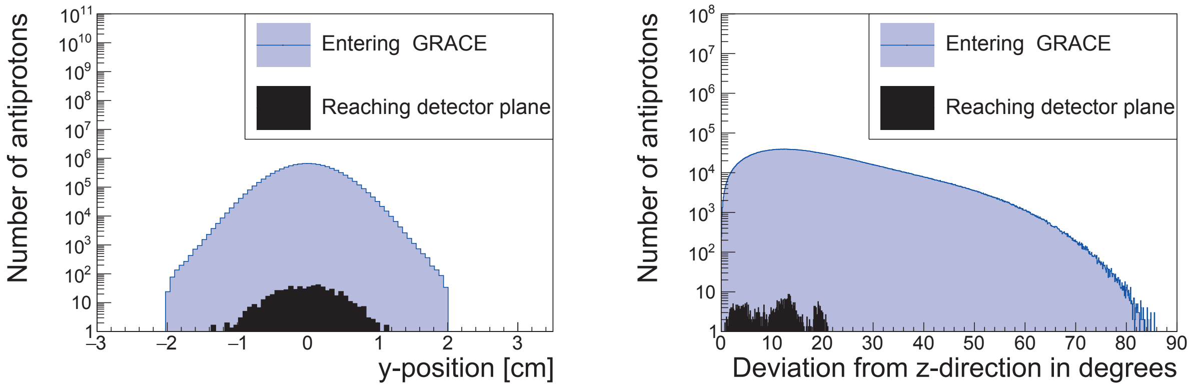

(c) Y-position of the antiprotons as they enter GRACE

(d) Deviation of the momentum vector from the z direction

Figure 4.11.: The beam parameters of the antiprotons as they enter GRACE. For each of the histograms, the part of the distribution belonging to the particles that made it to the detector plane is drawn in black.

5. Data analysis of the Timepix3 data from the GRACE beam line

This chapter describes how the data from the 675 µm thick Timepix3 detector was analyzed. The goal of the analysis is to characterize the clusters in order to study how an annihilation cluster is distinct from a secondary cluster. As defined in chapter 3 an annihilation cluster is caused by an annihilation in the detector itself, while a secondary cluster is caused by a nuclear fragment or pions originating from annihilations taking place elsewhere.

5.1. The data

Two data samples were collected during the test beams in 2015 and 2016, and consisted of one main data sample and one reference data sample. The main sample was taken using the optimal GRACE settings described in section 4, and consisted of 560 spills from the AD. Because the majority of the antiprotons did not annihilate in the detector itself, the main data sample contains a mixture of annihilation clusters and secondary clusters. From this data set 44 spills were reserved as training data to develop the algorithms for clustering and characterization. The clusters used as training data are excluded from the analysis. For this reason the main data set from here on refers to the data from the 516 spills that were not part of the training data.

The reference data sample was taken with the detector rotated such that its back was facing the beam. In this configuration no antiprotons annihilate directly on the detector. As seen in figure 4.3 the detector is mounted on an extended arm, and antiprotons can then pass this arm and annihilate on the walls of GRACE behind the detector. With the detector rotated only fragments from these annihilations can hit the detector. For this reason the reference data sample, consisting of 1561 spills, contains only secondary clusters.

During the data taking a bias voltage of 200 V was applied to the Timepix3 detector.

5.2. Time selection

As discussed in section 4.4.1 the antiprotons will arrive with a time delay compared to the main shower of annihilation products. This can be used to initially remove a large amount of the secondary clusters. In figure 5.1 the time of arrival distribution for all pixels in the main sample is shown, where time=0 is the estimated time the main shower of annihilation products hits the detector in one spill from AD. As expected a large peak consisting of secondary clusters is found around time=0. In the second peak both annihilations clusters and secondary clusters are found. The secondary clusters here mainly originates from annihilations of antiprotons that had low enough energy to be directed into the extraction line, but missed the detector. Since annihilation clusters are only found within the second peak, only pixels that are time delayed by more than 1000 ns are considered for analysis.

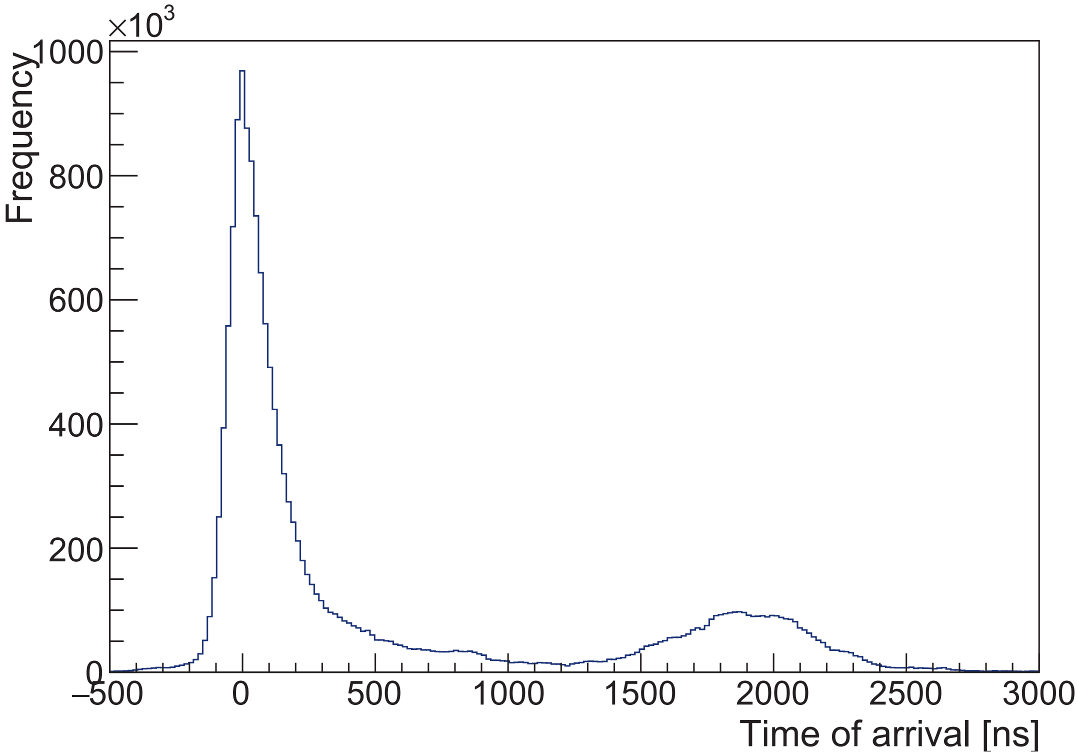

Figure 5.1.: The time of arrival in all pixels in the main data sample. The antiprotons are exclusively found in the second peak.

5.3. Removing the halo signal

As explained in section 3.4.1 the Timepix data has an excess of low energy hits that are not caused by real charge collection, the so called halo hits. Removing these hits makes the clusters easier to analyze.

In order to find a suitable threshold, the behavior of a Minimum Ionizing Particle (MIP) is considered, as any real particle would give energy depositions at least equivalent to a MIP. The search distance of the clustering algorithm presented in the next section is large enough to allow two missing pixels next to each other in a cluster. Geometrical considerations show that, for a pixel pitch p, a particle traveling less than $\frac{p}{\sqrt{2}}$ in one pixel it is bound to travel longer in at least one of the neighboring pixels. The calculation of this distance is illustrated in figure 5.2, where the path giving this minimum is drawn together with paths where the particle usually travels longer in each pixel, but occasionally travel shorter. For a pixel pitch of 55 μm this minimum distance is $\frac{p}{\sqrt{2}} = 38.9$ μm.

Figure 5.3 shows the simulated energy deposition from a MIP traversing 38.9 μm of silicon, compared to the distribution of the energy deposited in the pixels in the main data sample. As seen from this figure, the deposited energy from a MIP never goes below 5 keV, and therefore all pixels with a measured energy deposition below 5 keV is removed. This cut removes the vast majority of the halo hits, while it will never cut off a track caused by a real particle. It should also be mention that the cut at 5 keV gives a good margin. The argument for comparing to a pion traveling 38.9 μm is made in a 2D situation, meaning that the detector is assumed to be flat. In reality the detector is 675 μm thick, and most particles will also travel through some of that depth. This means the minimum path to be traveled in two adjoining pixels is usually higher than 38.9 μm.

Figure 5.4 illustrates the effect of this cut on the data. Figure 5.4a shows one shoot of antiprotons after the time cut, but before the halo hits are removed. Figure 5.4b shows the frame after the cut at 5keV has been applied. As one can see the halo around the large energy depositions are removed by the cut, and the star shapes are more clear.

5.4. Clustering and cluster characterization

After the initial time selection and removal of the halo hits, the next step of the data analysis is clustering. Pixels that are connected to one of their neighbors by less than 20 ns in time and less than 225 μm in distance are defined as a cluster. These parameters were tuned by inspecting the training data set which was excluded from the analysis. The combination of clustering in both time and space has the advantage that clusters overlapping in space can be distinguished if they don't overlap in time. This also allows a larger spatial search distance, in this case 225 μm. Using a large search distance is important because the first shower of nuclear fragments and pions will, if a pixel does not have time to recover, cause suppressed pixels when the antiprotons arrive. Therefore a long search distance reduces the possibility for a cluster to be subdivided due to suppressed pixels.

As discussed in chapter 3, an annihilation cluster is characterized by a center with high energy deposition and possibly prongs originating from this center. Therefore an algorithm to identify the prongs and the center of a cluster was developed. The algorithm is described below, while technical documentation for the program implementing the algorithm is found in appendix C. Also here, reasonable values of the parameters were found by inspecting the

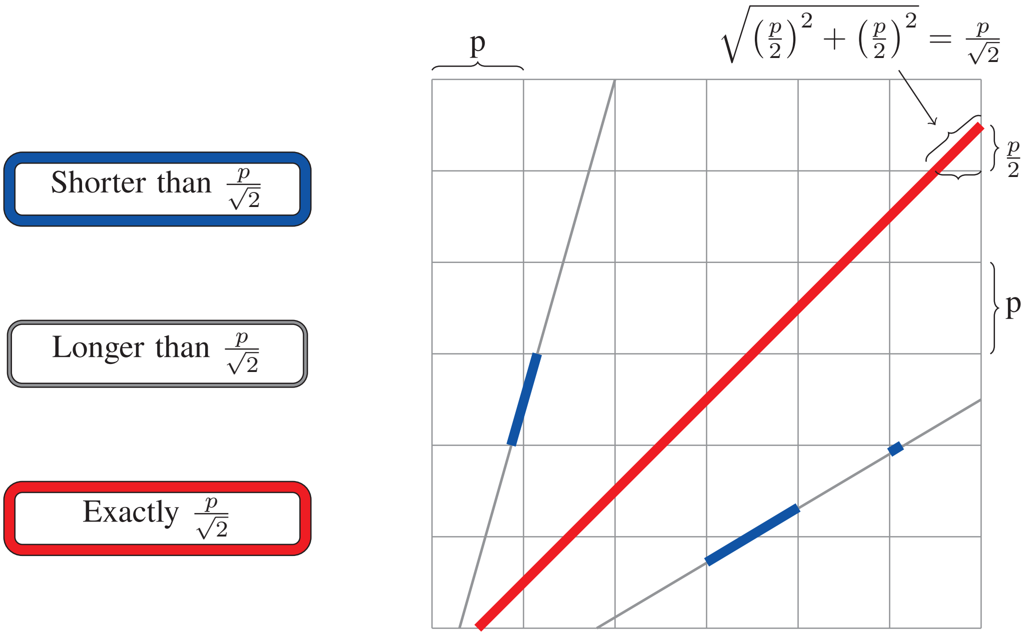

Figure 5.2.: The minimum distance a particle can travel in two adjoining pixels is $\frac{p}{\sqrt{2}}$.

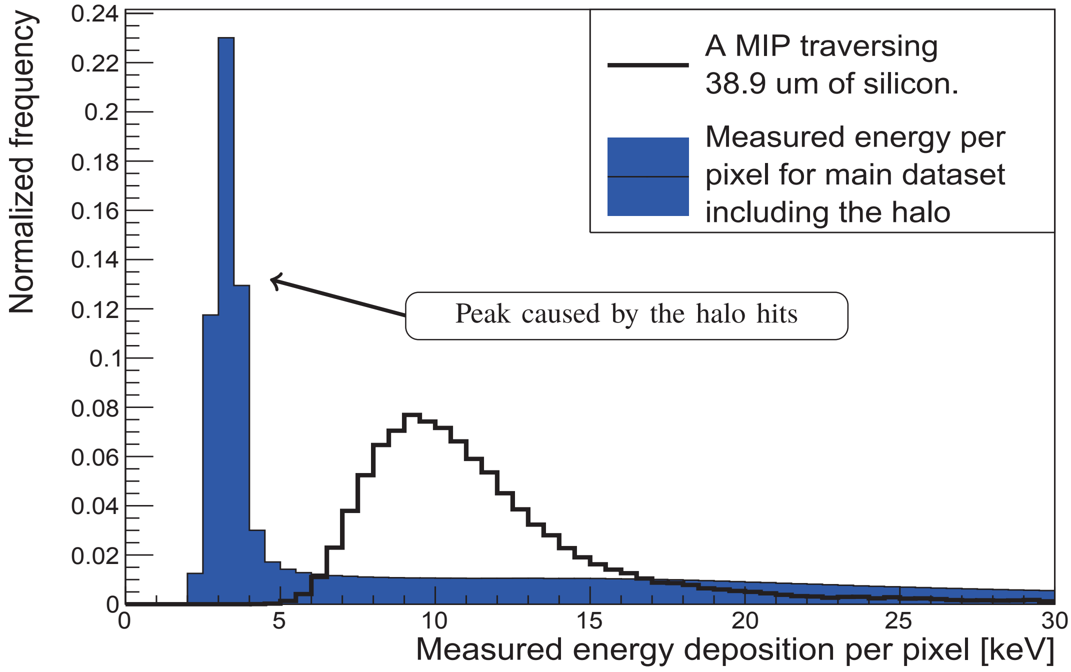

Figure 5.3.: Energy deposition of a MIP (pion of 200 MeV) when traversing 38.9 µm of silicon material, simulated by FLUKA, compared to the measured energy depositions in all the pixels in the main data sample.

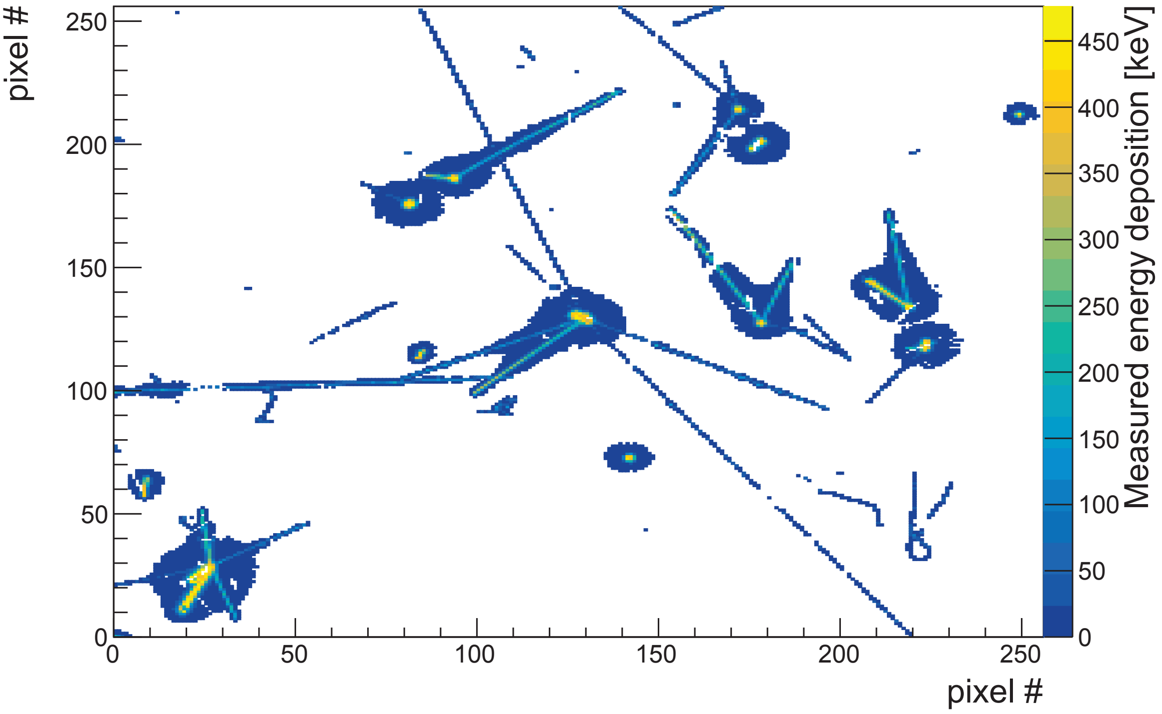

(a) Before the halo hits have been removed.

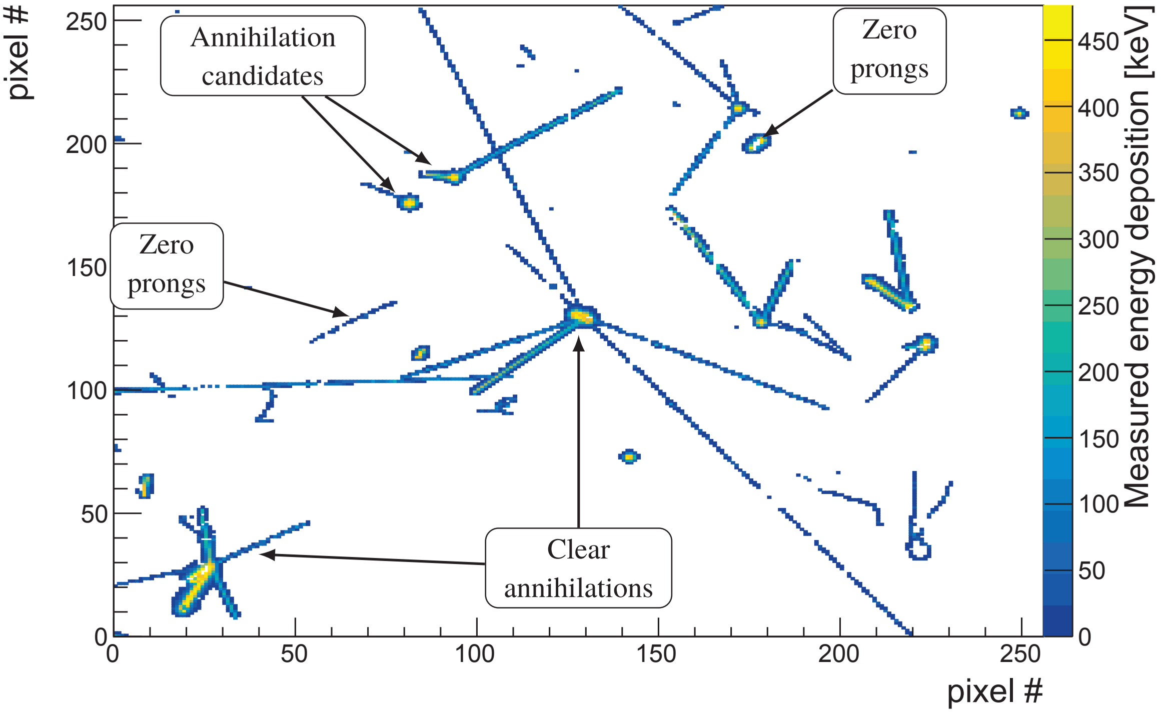

(b) After the halo hits have been removed.

Figure 5.4.: These two frames show all hits, from one antiproton spill, that are time-delayed by more than 1000 ns from the estimated arrival time into GRACE. Figure a) shows the frame before the halo hits are removed, while figure b) shows the frame after the halo hits are removed.

training data set that was excluded from the analysis. The flow of the algorithm is shown in figure 5.5, figure 5.6 shows examples of the different steps of the algorithm, while the description of the different steps follows below.

By inspecting the training data it turned out that some of the clusters where caused by particles, likely pions, entering parallel to the plane of the detector creating long tracks. These are not likely to be annihilation clusters, but an algorithm to identify prongs would characterize them as clusters having one or two prongs. Therefore, as a first step a straight line is fitted to the pixels in the cluster by the least square method. The spatial center of each pixel is used as the point for fitting. A low χ^2 value on this fit identifies clusters that are just a single track, and an example of such a cluster is found in figure 5.6a. For this reason any cluster that has a χ^2 value normalized to its degrees of freedom below 1.0 is assumed to have zero prongs. Figure 5.6b shows a cluster where the χ^2 is well above 1.0.

The second step is to estimate the spatial coordinates of the center of the cluster. For each pixel in the cluster the total deposited energy E_{center} in a circular region with a radius of 275 µm from the center of that pixel is calculated. The mass center of the region with the largest E_{center} is used as an estimate for the center of the cluster (x_0,y_0). The estimated center is indicated in figure 5.6c. The circular region with the highest energy deposition is then removed for the algorithm to more easily find the prongs. This region is from here on called the central region, and figure 5.6d shows the cluster after the central region has been removed.

The next step is to use Hough transformations [50] to identify the straight lines of the prongs extending from the center of the clusters with (x_0,y_0) as a fixed point along the path. The number of hit pixels within each circular segment with opening angle 3.6° radiating from the center of the cluster are counted. The segment with the maximum number of pixels gives the direction of the most evident prong. The pixels belonging to a prong are defined as all pixels within $\pm 20^\circ$ of the prong direction. Pixels belonging to the identified prong are then removed, and the subsequent most evident prong is identified in the same manner. This procedure is repeated until no more prongs consisting of at least 4 pixels are found. Figure 5.6f shows the cluster when the center and all prongs has been removed and no more prongs can be identified.

This algorithm makes it possible to collect the following observables for each cluster: The cluster size given by the number of pixels with energy deposition above 5 keV, the number of prongs, the total deposited energy in the cluster and the total energy deposited in the central region.

5.5. Difference between reference sample and main sample

In figure 5.7 the distributions of the four different observables is compared between the main data sample and the reference data sample. From the histograms it is evident that the main data sample has more large clusters, the clusters has more prongs, and the deposited energy is higher. Both samples seem to have a large proportion of small clusters with zero prongs and low energy depositions, and they are likely to be secondary clusters. It can also be seen that no characteristic seem to be exclusive to the main sample.

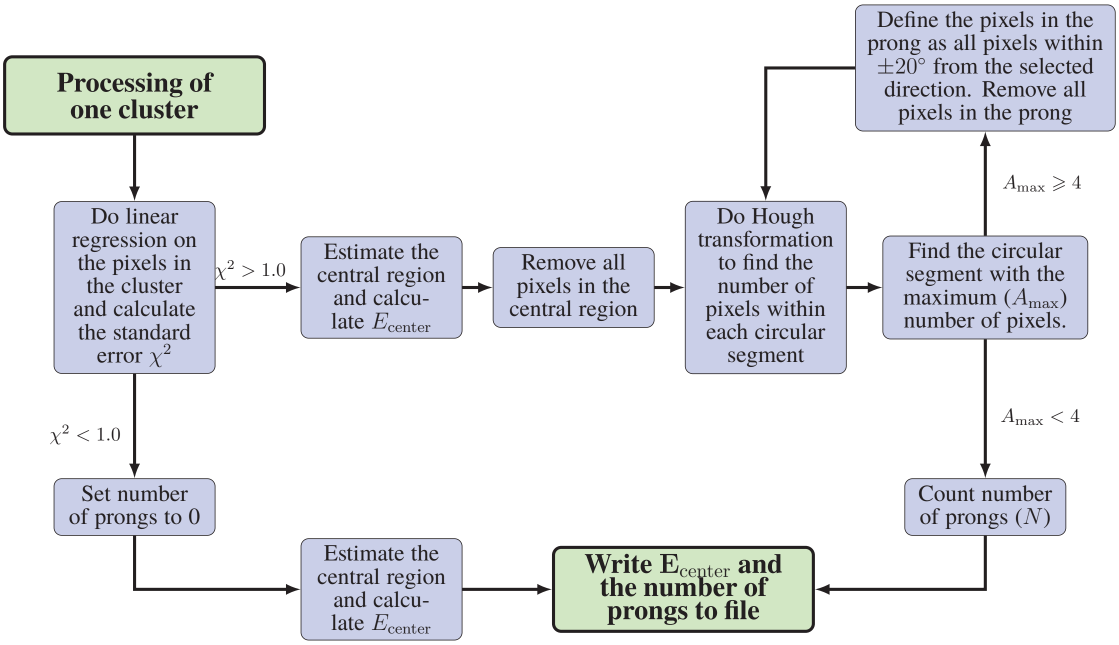

Figure 5.5.: Flow chart for the algorithm developed to characterize the clusters.

5.6. Conclusion

In this chapter the method to clean the data, do the clustering and characterize the clusters in therms of their size, total energy deposition, central energy deposition, and number of prongs was presented. Comparison between the main data sample and the reference data sample shows that annihilation clusters in general are larger, have more prongs and the deposited energy is higher. From the comparison it also seems likely that the main data sample contains a large amount of secondary clusters. In the next chapter these observables will be used to set clear tagging criteria for separating annihilation clusters from secondary clusters.

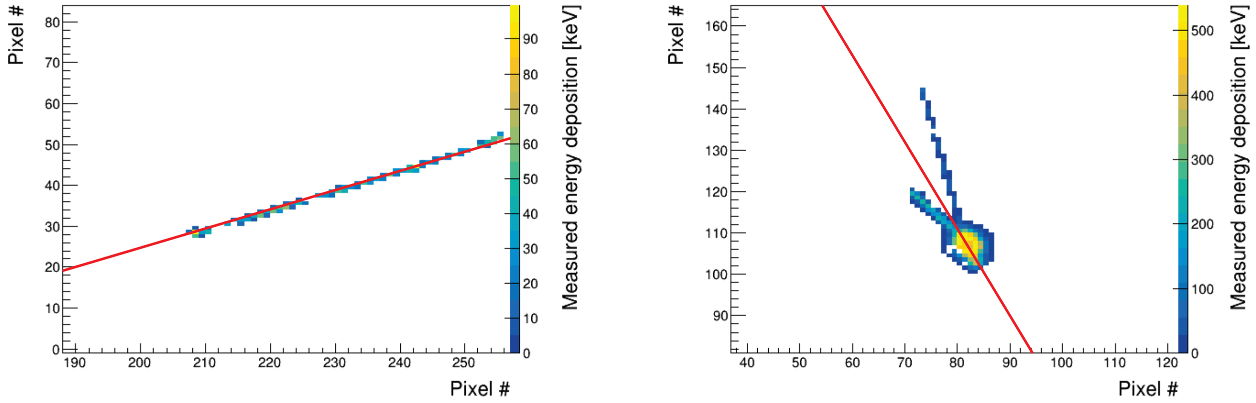

(a) This is an example of a cluster with a χ^2 value below 1.0, and this cluster is therefore characterized to have zero prongs.

(b) For this cluster the normalized χ^2 value is above 1, and the algorithm starts looking for prongs in the cluster.

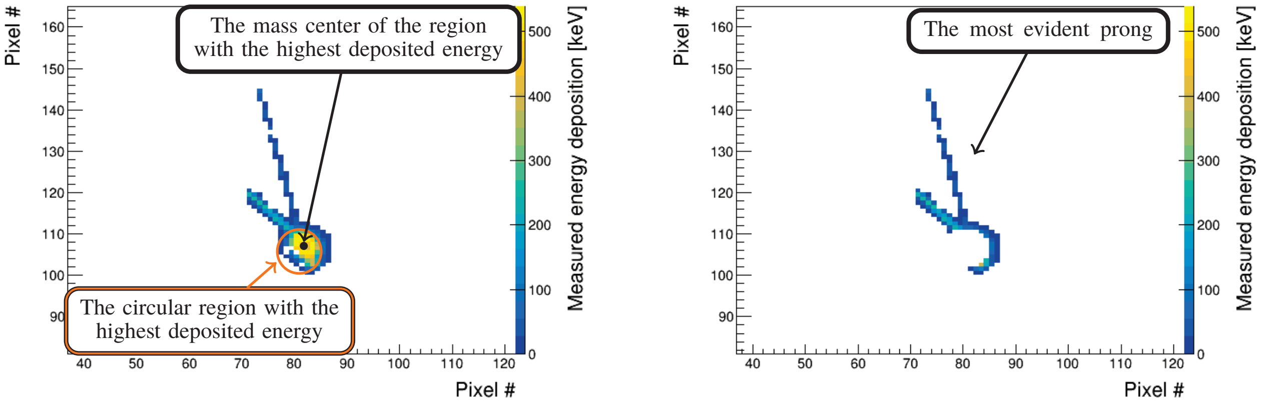

(c) The algorithm finds the circular region of radius 275 µm with the highest energy deposition. The mass center of this region is the estimated center of the cluster.

(d) The center of the cluster has now been removed and the algorithm uses Hough transformation to identify the most evident prong.

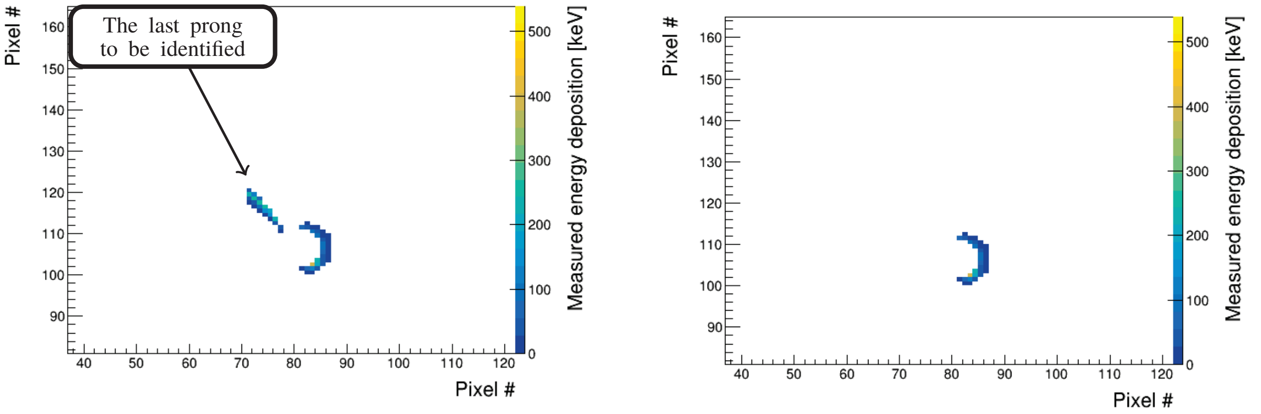

(e) One prong was found and is then removed before the algorithm looks for new prongs

(f) The second prong was removed and then no more prongs could be identified.

Figure 5.6.: Example of how the characterization algorithm analysis a cluster where zero or two prongs are identified.

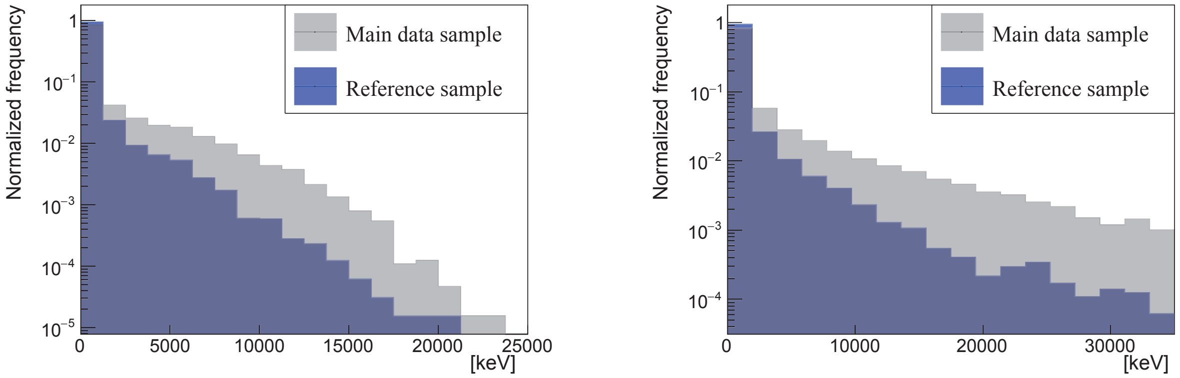

(a) Deposited energy in the central region.

(b) Deposited energy in the whole cluster.

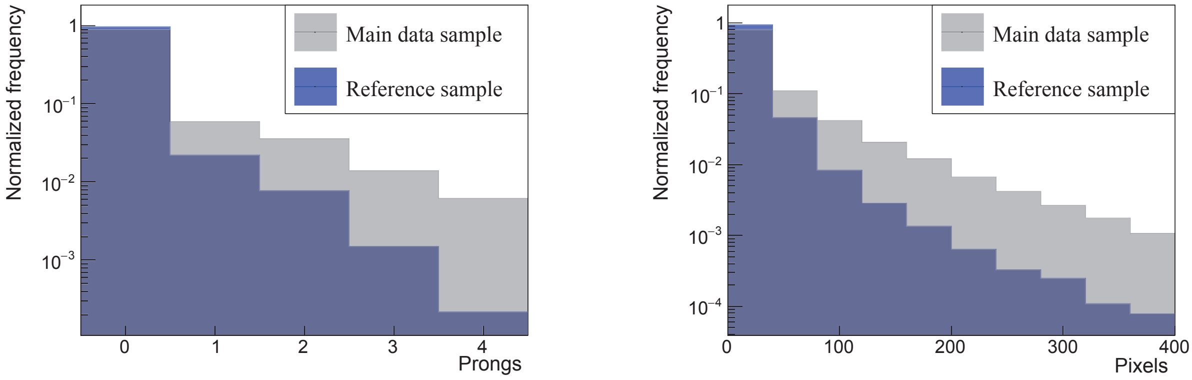

(c) Number of prongs.

(d) Cluster size.

Figure 5.7.: Comparison between the reference data sample and the main data sample for different observables of the clusters.

6. Developing and verification of a detector response model for antiproton annihilations in the Timepix3 detector

In this chapter first the detector response model and the verification of it are presented. Then the detector response model and the data are used to find the tagging efficiency and false tagging rate as a function of cuts on the observables discussed in the previous chapter. A discussion of possible systematic uncertainties and the effect of these on the tagging efficiency and false tagging rate is also included. Due to uncertainties coming from the annihilation model itself, as discussed in section 3.2, effort is made to support conclusions from the simulations by data driven methods. Therefore the tagging efficiency is also calculated by a mainly data driven method, this is presented in section 6.3.1. In section 6.4 a method depending only upon the data is used to calculate a minimum value for the purity of a sample tagged as annihilation clusters.

Technical documentation describing how to run the simulations is found in appendix D.

6.1. The detector response model

The detector response model is based on FLUKA [23]. FLUKA provides the energy deposited in chosen voxels in the detector; for this study the voxels are set to $5.5\times5.5\times225$ µm^3 (x × y × depth). Voxels much smaller than the pixel size is chosen in order to take into account the position of the energy deposition within the pixel. This section describes how these raw energy depositions are processed to simulate the detector response. Using the detector response model described here a sample of 10 000 simulated annihilation clusters was produced.

6.1.1. Modeling charge sharing between pixels

Charges liberated by the energy depositions will diffuse as they drift towards the collecting electrodes, causing charge sharing between pixels. In the simulation this is modeled by spreading out the deposited charge on the read out electrodes by a Gaussian blur. Assuming a Gaussian shape of the charge cloud, its size in terms of the standard deviation at the readout electrodes is

$$\sigma = \sqrt{2Dt_d} \, , \tag{6.1}$$

where the amount of diffusion depends on the collection time t_d, and the diffusion constant D [14].

As explained in section 3.4.2 antiproton annihilations causes large enough energy depositions for the plasma effect [37] to be a concern, and the collection time depends upon the magnitude of the energy deposition. Consequently TCAD is used to make a parameterized model for the collection time. The collection time is simulated for different energy depositions at three different depths, corresponding to the three different depths of the center of the voxels. The results from this simulations are found in table 6.1. For comparison the collection time from the simple model in equation (2.6) is also indicated. There is good agreement between the collection time given by the two models for energy depositions of 1 keV and 10 keV, giving evidence that the plasma effect is not present here. For larger energy depositions, the collection time clearly differs, as expected due to the plasma effect.

The diffusion constant for holes in silicon at room temperature is 12 cm^2/s [17], and this value is used to calculate the charge spread in equation (6.1) when the plasma effect is not present. When the plasma effect is present, the effective diffusion coefficient is found to be 18.0 cm^2/s in silicon at room temperature [37]. This value is used for energy depositions above 10 keV since table 6.1 shows that the collection time found by TCAD starts deviating from the simple model for energy depositions larger than 10 keV, indicating that the plasma effect starts to be significant here.

The standard deviation σ used to spread out the charges liberated in a voxel is found by first collecting the energy depositions in the neighborhood of that voxel. The neighborhood has to be taken into consideration as a continuous energy deposition from one particle is discretized in several voxels, and it is defined by all voxels with their center within a radius of 25 µm. Then table 6.1 is used as a lookup table to find the σ that corresponds to the energy deposition in the neighborhood. Since deposited energy can take on continuous values, linear interpolation is used between the values in table 6.1.

6.1.2. Modeling front-end electronics effects

In the simulation two front-end electronic effects are taken into account; the volcano effect and suppressed pixels due to the dead time of the pixels. The volcano effect, as described in section 3.4.3, causes the pixels receiving high-energy depositions to saturate around 500 keV. In the simulation this effect is taken into account by setting all pixels with an energy deposition above 500 keV to a random value following a Gaussian distribution with mean 500 keV and standard deviation 50 keV.

The majority of the pixels in the main data set have a dead time of approximately 550 ns after being hit. The dead time is taken into account by, for each simulated cluster, choosing one random bunch from the experimental main data sample. The pixels in that bunch which are time-delayed between 1350 ns and 1900 ns are set as suppressed in the simulated cluster. This time interval is chosen because the center of the second peak in the ToA distribution in figure 5.1 is at 1900 ns, indicating the most likely time delay for an antiproton. An antiproton arriving at the most likely time will see all pixels triggered in the chosen time interval as suppressed.

6.2. Verification of the detector response model

The detector response model is verified by comparing the distributions of the cluster observables discussed in the previous chapter between data and simulation. The simulated clusters are analyzed in exactly the same way as the real data, the low energy hits are removed, the clustering uses the same parameters and the same method for characterization is used.

Table 6.1.: Lookup table to find the amount of charge sharing from the energy deposited around the charge that is transported.

Energy deposited	Depth [µm]	Collection time t$_c$ from eq. (2.6) [ns]	Collection time t$_c$ from TCAD [ns]	Calculated σ from TCAD [µm]
1 keV	562.5	45	30	8.5
	337.5	17	14	5.8
	112.5	5	6	3.9
10 keV	562.5	45	36	9.3
	337.5	17	17	6.4
	112.5	5	7	4.1
100 keV	562.5	45	79	16.8
	337.5	17	26	9.6
	112.5	5	16	7.5
1 MeV	562.5	45	349	34.5
	337.5	17	98	18.8
	112.5	5	48	13.0
10 MeV	562.5	45	1780	80.0
	337.5	17	494	42.2
	112.5	5	243	29.6
50 MeV	562.5	45	4584	128.4
	337.5	17	1534	74.3
	112.5	5	760	52.3

The cluster observables used for comparison between data and simulation is the cluster size, the number of prongs, the energy deposited in the center of the cluster, and the energy deposited in the whole cluster. As already discussed in section 5.1 the main data sample contains an unknown mixture of secondary clusters and annihilation clusters, while the reference sample contains only secondary clusters. Therefore the main data sample is compared to a weighted combination of the reference data sample and the sample of simulated annihilation clusters. This combined sample of reference data and simulated annihilation clusters is normalized to the total number of clusters in the main data sample.

The fraction of the reference data sample in the combined sample, from here on referred to as r, is a free parameter that is optimized to minimize the χ^2 value of the difference between the histogram bins. The minimum value of χ^2 is found when $r = 0.83$, and figure 6.1 shows the comparison between the main data sample and the combined sample using this value for r. For observables relating to the shape of the cluster the agreement between data and simulation is good. There is some discrepancy in the deposited energy, especially in the center of the cluster, as seen in figure 6.1d. This discrepancy may be caused by inaccuracy in how FLUKA models antiproton annihilations, or how the volcano effect is modeled.

The optimization can also be done on each histogram individually, and the values for r minimizing the χ^2 value of the histograms of the cluster size, number of prongs, deposited energy in the center of the cluster, and deposited energy in the whole cluster are 0.81, 0.85, 0.87 and 0.8, respectively.

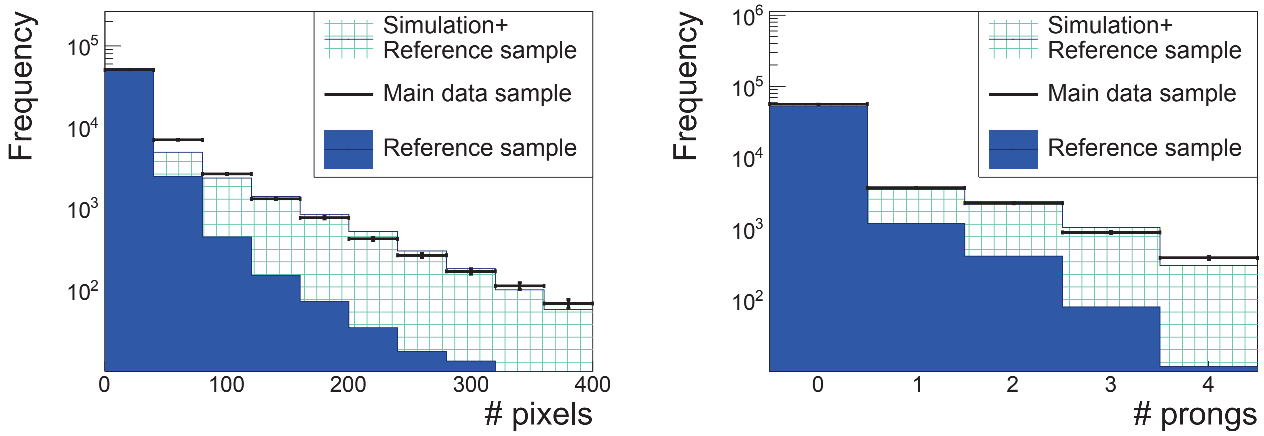

(a) Cluster size in terms of pixels.

(b) Number of prongs detected in the clusters.

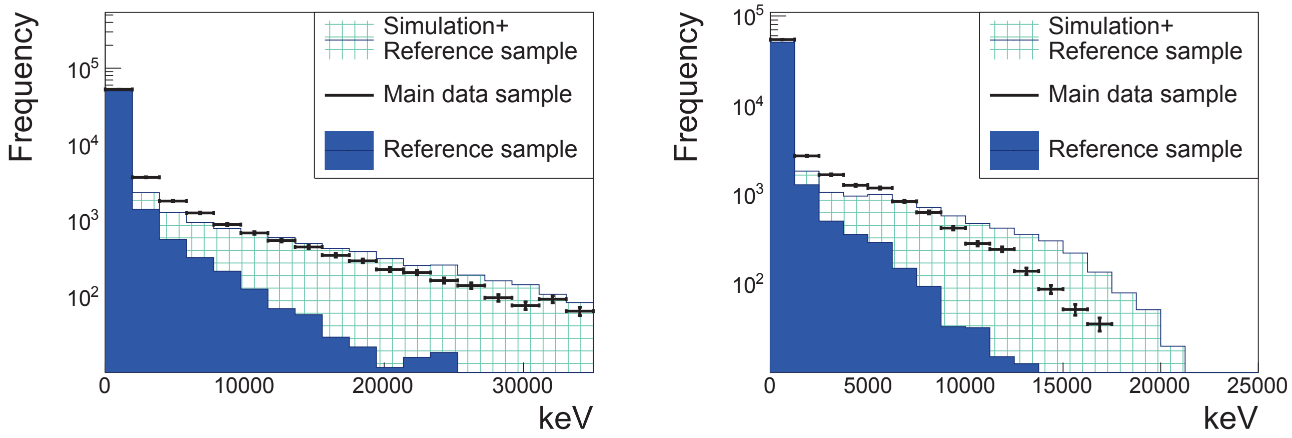

(c) Measured energy deposition in the clusters.

(d) Measured energy deposition in the center of the clusters.

Figure 6.1.: Histograms comparing the cluster observables in data and simulations. Observables relating to the shape of the clusters seem to be modeled better. The fraction of secondary clusters is estimated to be $r = 0.83$.

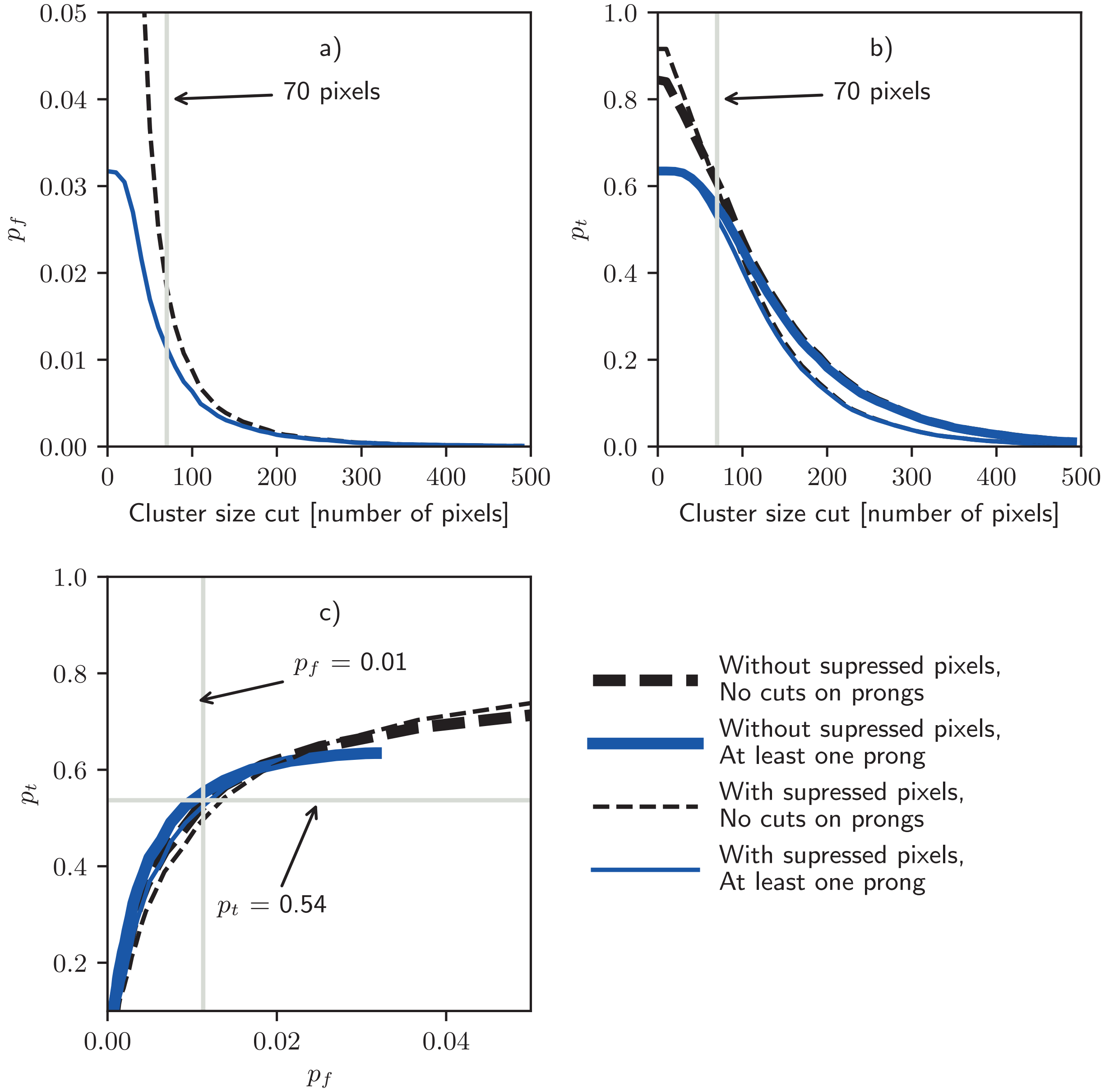

Figure 6.2.: Plots showing the relationship between tagging efficiency (p_t), false tagging rate (p_f) and the cuts. **a)** The false tagging rate as a function of the cuts. **b)** The tagging efficiency as a function of the cuts. **c)** The tagging efficiency as a function of the false tagging rate.

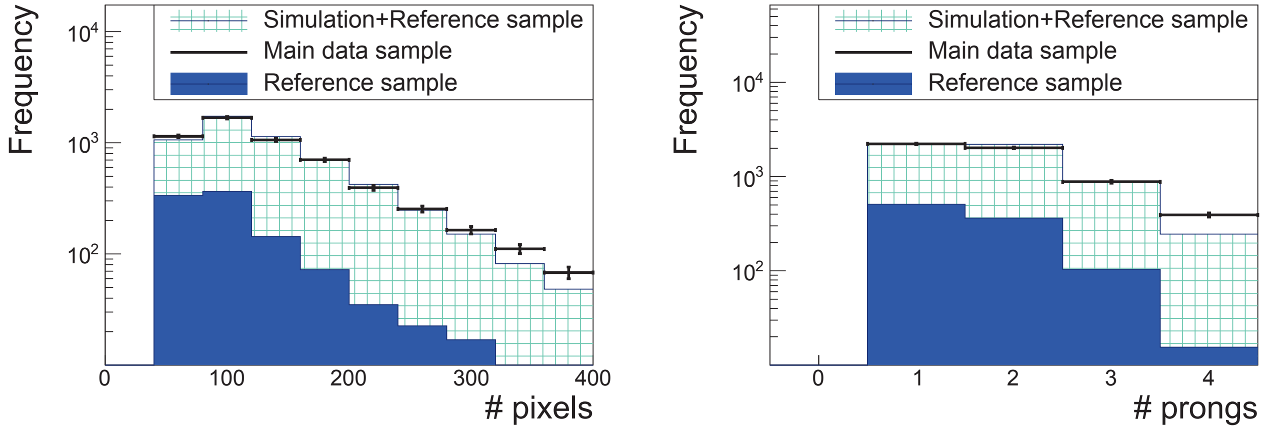

(a) Cluster size in terms of pixels after selection.

(b) Number of prongs detected in clusters after selection.

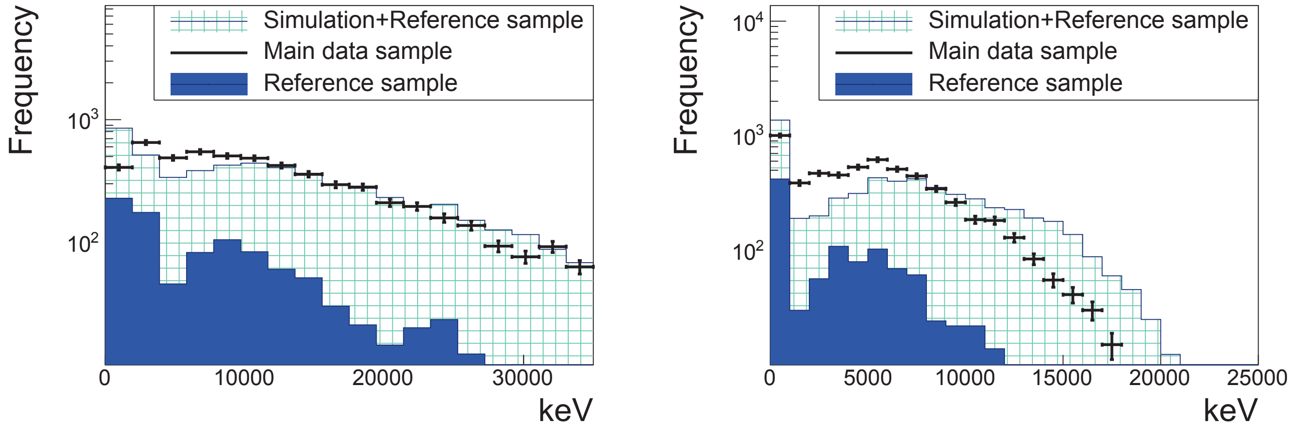

(c) Measured energy deposition in the clusters after selection.

(d) Measured energy in center of the clusters after selection.

Figure 6.3.: Comparison between data and simulation for clusters passing the cut of at least 70 pixels and at least one prong. As in figure 6.1 observables related to the shape of the clusters are better modeled. The fraction of secondary clusters is estimated to be 0.16.

6.3. Estimate of the tagging efficiency and the false tagging rate

This section shows how cuts on cluster size and number of prongs are set in order to tag the antiprotons. These two cluster observables are chosen because the observables relating to the shape of the clusters are more accurately modeled than the ones depending upon the deposited energies.

The tagging efficency, from here on referred to as p_t, is estimated by the fraction of clusters that passes the cuts in the sample of simulated clusters. The false tagging rate, from here on referred to as p_f, is defined as the probability of mistagging a secondary cluster as an annihilation cluster. The value of the false tagging rate is estimated by applying the cuts on reference data sample.

Figure 6.2 shows p_t and p_f as functions of the cuts. The results are shown with and without considering the suppressed pixels in the simulation, as further experiments might be able to reduce the flux of secondary clusters and hence avoid suppressed pixels due to dead time. The estimate of p_f always includes suppressed pixels as it is estimated from experimental data. A cut of at least 70 pixels and at least one prong in the cluster gives a tagging efficiency of p_t = 52 %. The corresponding value of p_f is then 1.1%, making this cut a good compromise between high tagging efficiency and low false tagging rate. The comparison of the cluster observables after such a cuts is shown in figure 6.3, and the value for r minimizing the χ^2 of the differences between the histogram bins is 0.16.

6.3.1. The uncertainty of the tagging efficiency and the false tagging rate

The statistical uncertainty on the tagging efficiency and the false tagging rate depends only on the sample size n and is given by

$$\sigma = \sqrt{\frac{p(1-p)}{n}} \,, \tag{6.2}$$

where p is the estimated rate. This gives a statistical uncertainty of ± 0.5 % and ± 0.2 % for the tagging efficiency and the false tagging rate respectively. However, as seen in figure 6.1 the simulation does not completely reproduce the data, leaving some discrepancy between data and simulation. This is caused by systematic effects, and two sources of systematic effects are identified.

The first being that the reference sample might not completely represent the secondary clusters in the main data sample. The secondary clusters in the main data sample can be caused by annihilations happening anywhere, although solid angle considerations and the time cut makes it more likely for them to happen close to the detector. In the reference sample the clusters are only caused by annihilations happening upstream of the detector. Therefore secondary clusters in the main sample might be caused by pions and nuclear fragments impinging more orthogonal to the detector compared to the reference sample. This could cause slightly larger clusters in the reference sample, and therefore the false tagging rate might be overestimated.

The second systematic error concerns how well the simulated clusters reproduce the annihilation clusters in the main sample. As mentioned in section 3.2 the simulation of the antiproton annihilations process has some uncertainty to it as it is based upon theoretical models and sparse data, and it has never been possible to fully verify it against data. To estimate this effect the tagging efficiency is also calculated by a mainly data-driven method. In the main data sample the number of correctly tagged annihilation clusters is given by

$$A_t = N_t - N f p_f \ , \tag{6.3}$$

where N_t is the number of tagged clusters, N is the total number of clusters, f is the fraction of secondary clusters in the sample, and p_f is again the false tagging rate. The total number of annihilation clusters is

$$A = N - fN. \tag{6.4}$$

The tagging efficiency is estimated by the number of correctly tagged annihilation clusters divided by the total number of annihilation clusters, yielding the following expression for the tagging efficiency:

$$t = \frac{A_t}{A} \ . \tag{6.5}$$

In the main data sample N = 63890, and with the applied cuts of at least 70 pixels and at least one prong N_t = 5233. The value of f is unknown, but in section 6.2 the fraction of secondary clusters is estimated to be in the range of 0.81–0.87. From equation (6.5) this corresponds to a tagging efficiency between 38% and 56%.

This method of calculating the tagging efficiency includes the false tagging rate that might be overestimated. However, the effect is not severe. Setting the tagging false rate to half of its estimated value would shift the tagging efficiency to lie between 40% and 60%.

In conclusion the systematic effects points to the tagging efficiency and the tagging false rate not being known to high precision, but supports that the tagging efficiency is in the range of $50 \ \pm 10\%$, while the tagging false rate is below 1.1%.

6.4. Estimating the minimum purity of a sample of tagged annihilation clusters.

It is beneficial to be able to estimate the purity of a sample of tagged clusters. That requires knowing the probability that a cluster is indeed an annihilation cluster given that it is tagged as such. From here on this probability is refereed to as p_p. The value of p_p depends upon the ratio of annihilation clusters to secondary clusters, therefore p_p is estimated specifically for the main data sample. The value of p_t is given as:

$$p_p = 1 - \frac{f p_f}{p_t} \tag{6.6}$$

where f is the fraction of secondary clusters in the sample, p_f is as usual the false tagging rate and p_t is the probability to tag a cluster in the sample. For derivation of this expression see InfoBox 6.1 at the end of this chapter.

The probability distributions of p_f and p_t as estimated from data are given by the beta distribution with parameters $\alpha = y + 1$ and $\beta = N - y + 1$ [51], where N and y is the total number of cluster and the number of tagged clusters in the respective samples. For explanation of why they follow the beta distribution see InfoBox 6.2 at the end of this chapter.

As seen in equation 6.6 the resulting probability distribution for p_p depends upon f. The value of f is not known, however it can not be larger than 1.0, since the amount of secondary clusters in a sample can not be larger than the total amount of clusters.

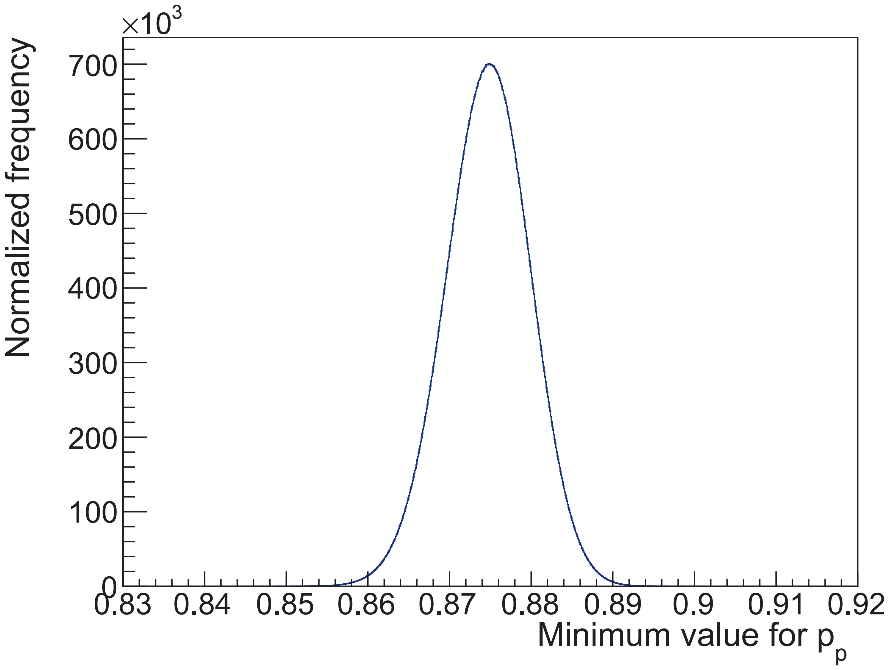

Figure 6.4.: The distribution of the minimum possible value of p_p (the probability that an annihilation cluster is correctly tagged) in the main data sample.

Figure 6.4 shows the distribution for p_p when $f = 1.0$. The mean of this distribution is 0.876, and by integrating the distribution it can be concluded with 97.5% confidence that the minimum possible value (p_p when $f = 1$) is above 0.866.

6.5. Conclusion

In this chapter the detector response model has been presented, and verified against experimental data. In particular it was discussed how the different peculiar effects of large energy depositions that were presented in chapter 3 were incorporated into the model. The comparison between data and simulation was quite good for the cluster size and number of prongs in the cluster, and therefore these two features where used for tagging. Using the detector response model and the data the tagging efficiency was evaluated to be 50%±10% with a cut at 70 pixels and at least one prong, while the false tagging rate was estimated to be below 1.1%. It was also concluded that the minimum possible value for the probability of correctly tagging a cluster in the main sample is with a confidence of 97.5% higher than 86.6%.

The probability to correctly tag an annihilation cluster is the same as the fraction of correctly tagged annihilation clusters in an infinity large sample. By expressing the number of correctly tagged clusters as the total amount of tagged clusters subtracted the falsely tagged the following expression is obtained

$$p_p = \frac{N_t - fp_f N p_f}{N_t}. \tag{6.7}$$

Here N is the total number of clusters, N_t is the number of tagged cluster, f is the proportion of secondary clusters in the sample and p_f is the false tagging rate. For the infinite sample $\frac{N_t}{N} = p_t$, and by substituting this into the equation 6.7 the same expression as in equation 6.6 is obtained.

$$p_p = 1 - \frac{fp_f}{p_t} \tag{6.8}$$

InfoBox 6.1.: Derivation of the expression found in equation 6.6 giving the probability that an annihilation cluster is tagged correctly.

Tagging antiprotons in a data sample can be considered as drawing from a binomial distribution $P(y|p) = B(N,p)$, where p is the probability to tag a cluster as an annihilation cluster, N is total number of clusters, and y is the number of tagged cluster . The estimate of interest is the probability distribution of p given the data, in mathematical terms this can be written as P(p|y). Using Bayes rule one obtain:

$$P(p|y) = \frac{P(y|p)P(p)}{P(y)} \tag{6.9}$$

Inserting the binomial distribution for P(y|p) gives

$$P(p|y) = \frac{\binom{N}{y} p^y (1-p)^{n-y} P(p)}{P(y)} \tag{6.10}$$

The values of y and N is know. Assuming there is no prior knowledge of $P(p)$ it is reasonable to assume it follows a uniform distribution in the range [0,1], and is therefore also a constant. Then the probability distribution for $P(p|y)$ can be written as

$$P(p|y) = \frac{p^y (1-p)^{n-y}}{K} \tag{6.11}$$

where K is a proportionality constant such that the integral of $P(p|y)$ is 1 in the range [0,1]. This can be recognize as the beta distribution

$$P(p|y) = \beta(y+1, n-y+1)$$

with parameters $\alpha = y + 1$ and $\beta = n - y + 1$.

InfoBox 6.2.: Derivation of the probability distribution for p_t and p_f.

7. Reconstruction of the annihilation point

In this chapter a sample of simulated clusters will be used to evaluate two methods for reconstructing the annihilation point; the mass center method and the vertex fitting method. Experiments for measuring the gravitational fall are expected to have low flux and therefore the pixels will in general have time to recover between being hit by different particles. For this reason the modeling of the suppressed pixels is excluded from the simulation here. It is also assumed that the annihilation occurs in the central 5×5 mm^2 of the detector such that prongs are not cut off by the edges of the detector. Except from these two changes the simulated clusters are produced as described in chapter 6.

The relevant measurement for AEgIS is the vertical shift of the fringe pattern created by antihydrogen passing through the moiré deflectometer. Therefore the position resolution is calculated only in the vertical direction y. Since the analysis is done on simulated clusters the exact annihilation position is known, and the residuals are defined as the distance between the estimated annihilation point and the true annihilation point in the vertical direction. The metric chosen for position resolution is the symmetrical 68% confidence interval around 0 for the residuals, corresponding to 1.0 σ for a Gaussian distribution. This method of calculating the position resolution suppresses the effect of outliers.

Technical documentation for the program developed to reconstruct the annihilation point is found in appendix D.

7.1. Mass center method

A possible method for reconstructing the annihilation position is to estimate it as the weighted relative position of the energy depositions in the central region. The definition of the central region is found in section 5.4. This method is from here on refereed to as the mass center method. Figure 7.1a shows the residuals of the reconstructed annihilation points using the mass center method, while figure 7.1b shows the projection of this plot in the vertical direction which is the measurement of interest. The position resolution is estimated to be 93 µm. This method can be applied to all clusters, as it does not require the presence of prongs. Usually it would only be applied to the clusters tagged as annihilation clusters. Using the tagging criteria of at least one prong and at least 70 pixels, a tagging efficiency of 68% is achieved when suppressed pixels are not considered and the annihilation happens in the center of the detector.

7.2. Vertex fitting method

The vertex fitting method fits straight lines to the prongs, and the annihilation point is taken as the intersection between two of these lines. The lines are fitted by the orthogonal-least-squares method [52]. The vertex fitting method requires at least two prongs, and 45% of the

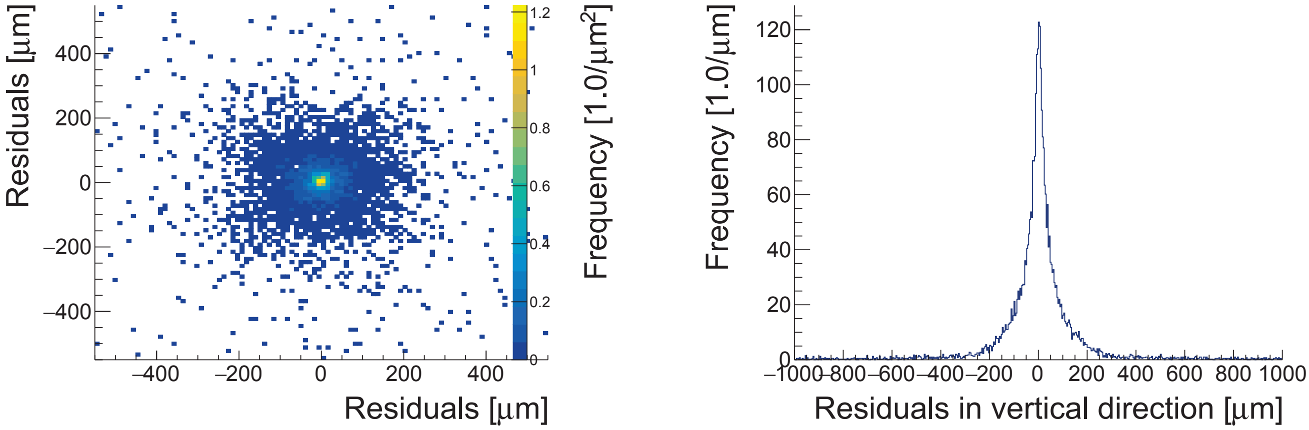

(a) Reconstructed annihilation point for antiprotons using the mass center method.

(b) Vertical distance between the fitted value and the true annihilation point using the mass center method. Estimated position resolution by 68% center is 93 µm.

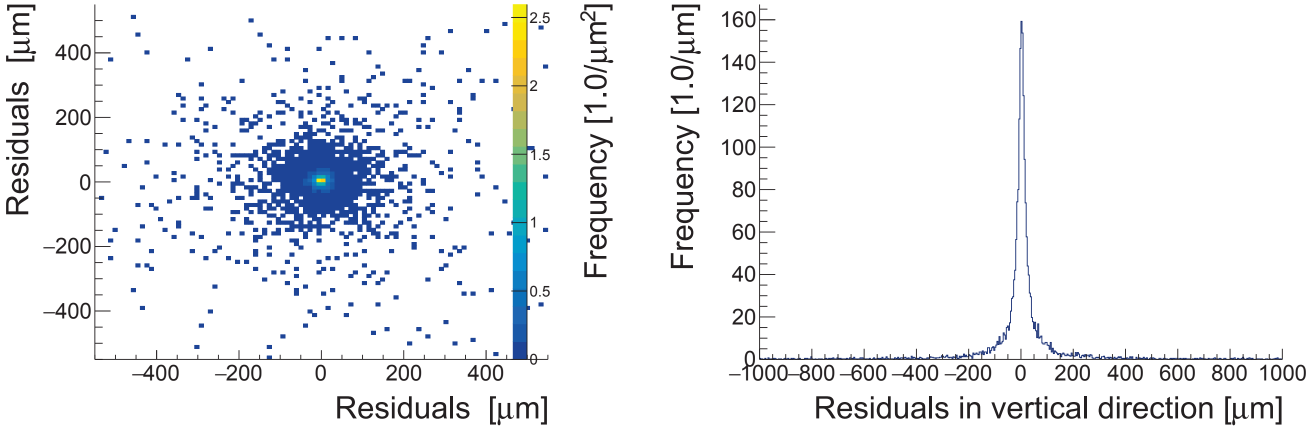

(c) Reconstructed annihilation point for antiprotons using the vertex fitting method.

(d) Vertical distance between the fitted value and the true annihilation point using the vertex fitting method. Estimated position resolution by 68% center is 48 µm.

Figure 7.1.: Position resolution using the mass center method and the vertex fitting method.

clusters pass the standard tagging criteria of at least 70 pixels and in addition have two or more prongs.

Figure 7.2 shows how the residuals of the vertex fitting method correlate with the average number of pixels in the two prongs, the average length of the prongs, the crossing angle α between the two prongs, and the discrepancy of the estimates yielded by the two methods.

According to figures 7.2a and 7.2b, the residuals are independent of the length of the prongs and the number of pixels in the prongs. One possible explanation why these two factors does not contribute to a better fit is that the same two factors also increases the probability that the prong undergoes scattering. Figure 7.2c show how the crossing angle between the two prongs correlates with the residuals. The y-axis is in units of the absolute value of 90° minus the crossing angle, $|(90 - \theta)|$. In other words, the y-axis shows the deviation of the crossing angle from a 90 degree angle. The correlation seen in figure 7.2c therefore shows that a crossing angle approaching parallel correlates with a bad fit, however the correlation is very weak and almost not visible in the scatter plot.

Figure 7.2d shows the correlation between the discrepancy of the estimates from the two reconstruction methods and the residuals, and a strong correlation is evident for large residuals. The correlation is very clear when the discrepancy between the two methods is above 100 µm. This figure indicates that if the two methods disagree, the vertex fitting method is likely to give a bad estimate. The reason is that two distinct methods are unlikely to estimate the same annihilation vertex if one of the estimates are wrong. Consequently the difference between the two methods is large if the vertex fitting method fails at reconstructing the annihilation point accurately.

The following procedure is applied if there are more than two prongs yielding more than one candidate for the annihilation point. If two or more of the candidates are within a distance of ± 55 µm to each other, the average of this cluster of candidates is taken as the estimate. If all candidates are separated by more than 55 µm, the one with its crossing angle closest to 90° is chosen since a crossing angle close to 90° correlates with a good fit. This method proved to be more robust than reconstructing to a common vertex since, in cases where there are more than two prongs, it is likely to exclude prongs that does not contributing to a good estimate. The residuals found from the vertex fitting method is shown in figure 7.1c and 7.1d, and the vertical position resolution is improved from 93 µm to 48 µm compared to the mass center method.

In some situations it might be beneficial to select a smaller sub-sample of clusters that are known to yield better reconstructed values. The disagreement between the two methods indicates a bad fit, and therefore excluding clusters where the two methods don't agree can provide such a sub-sample of clusters that are more accurately reconstructed. Requiring the difference between the estimates from the two methods to be less than 110 µm, a sub-sample consisting of 22% of the clusters is selected, and in this sample a position resolution of 22 µm is obtained.

By re-sampling the MC data the statistical uncertainty on the position resolution is found to be only $\pm$ 0.5 µm. However, the achieved position resolution might be subject to systematic errors caused by the simulation not fully reproducing experimental data. Assuming that this manifests itself in a different spectrum of annihilation products it is relevant to check how a change in annihilation products affects the position resolution. Therefore the simulation of the annihilations and the vertex reconstruction is also ran with a geometry where the metalized layer has been replaced by carbon and calcium, instead of the aluminum layer of the Timepix3 detector. According to FLUKA this respectively gives a higher and lower ratio of pions to nuclear fragments. The resulting position resolutions are 21.3 µm for annihilation in carbon and 21.8 µm for annihilation in calcium. This indicates that this systematic effect does not influence the position resolution to a large extent.

7.3. Conclusion

In this chapter two different methods for reconstructing the annihilation point were studied, the mass center method and the vertex fitting method. The vertex fitting method gave the best result with a position resolution of 48 µm. However, this method can only be used on the clusters that had at least two prongs. By selecting a subset of 22% of all the annihilation clusters, it was possible to obtain a position resolution of 22 µm on this subset. As discussed in section 1.4 an absolute requirement for the position resolution is to be below the proposed 60-80 µm periodicity of the moiré deflectometer, and this requirement is met. However, the resolution of 10-13 µm required to measure the gravitation acceleration with a precision of ± 1% is not met. Even though this requirement is not met, the achieved position resolution should be good enough to perform a proof of principle measurement where a shift in the fringe pattern is observed.

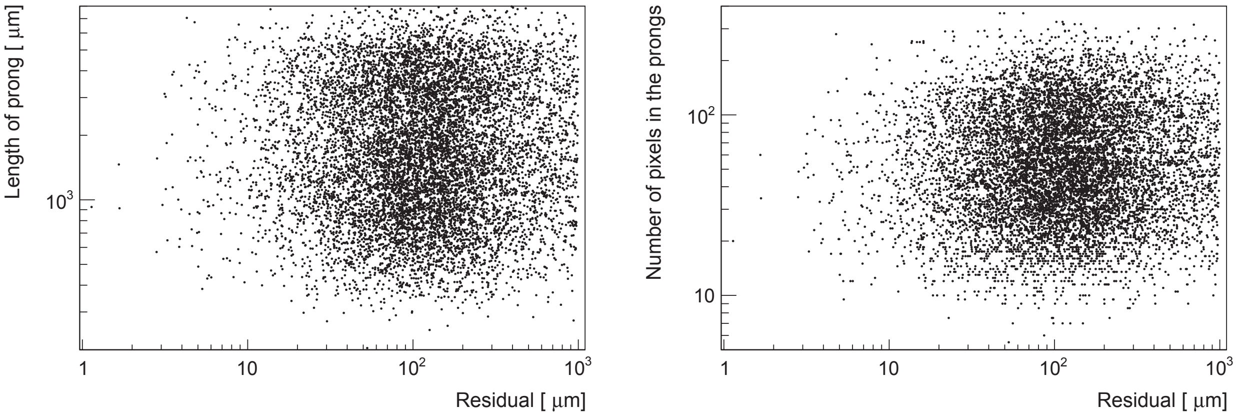

(a) Correlation between the length of the prongs and the residuals. The correlation coefficient is -0.007.

(b) Correlation between the number of pixels in the prongs and the residuals. The correlation coefficient is -0.015.

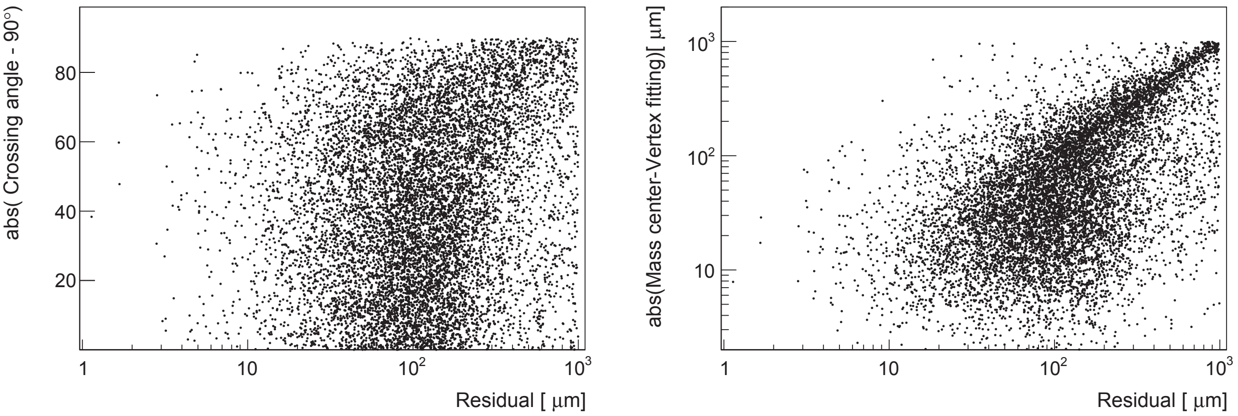

(c) Correlation between the angle between the prongs and the residuals. The correlation coefficient is 0.23.

(d) Correlation of the discrepancy between the two presented reconstruction methods and the residuals. The correlation coefficient is 0.64.

Figure 7.2.: Plots showing the correlation between prong parameters and the accuracy of the fit when estimating the annihilation point by the vertex fitting method.

8. Summary and conclusion

The motivation for the work of this thesis was to evaluate the usability of a pixel detector, in particular the Timepix3 detector, as a position sensitive detector for antihydrogen in the AEgIS experiment. Such a detector must be able tag the antiprotons, measure their time of arrival and reconstruct their annihilation point to a high presision.

The work started with initial studies of data from a 3D pixel detector placed inside the AEgIS apparatus together with data from a Timepix3 detector placed in a simple vacuum chamber on the secondary beam line of the AEgIS experiment. These studies provided the first good observations of antiproton annihilations in silicon pixel detectors. It was observed that a typical annihilation cluster had a center with large energy deposition, and possibly prongs originating from this center. In both of these studies the annihilation depth was higher than what is expected from the final gravity experiment. Furthermore, when data was collected in the simple vacuum chamber, the detector quickly saturated, and therefore a lot of data was lost.

To avoid these two problems the GRACE beam line was built, providing at maximum a flux of around 15 low energy antiprotons per spill from the AD. A full simulation of this beam line was also developed, and provides the expected flux and energy distribution of the antiprotons for different settings. GRACE was a success and provided a large data set of antiproton annihilations in a 675 µm thick Timepix3 detector. The analysis of these data, and the development and testing of the full detector response model for the Timepix3 detector are the main subject of this thesis.

The data analysis showed as expected that the annihilation clusters could be recognized by a central high energy deposition, and prongs originating from this center. An algorithm to identify the center and prongs of a cluster was developed, and used to characterize the clusters in both data and simulation. The data analysis also showed that the Timepix3 detector handles the low energy hits well, while high energy depositions that are common for antiproton annihilations gave rise to three peculiar detector effects; the halo hits, the volcano effect, and the plasma effect. A full detector response model, that took all these three effects into consideration, was developed and tested against data. Comparison between data and simulation showed that the shape of the clusters was well reproduced by the detector response model. The annihilation clusters was found to be larger and have more prongs than the secondary clusters, therefore these features was used as tagging criteria. A tagging efficiency of 50%±10% was estimated with cuts of at least 70 pixel and at least one prong for the data collected in the GRACE beam line. The corresponding tagging false rate was 1.1%.

Using the detector response model methods for reconstructing the annihilation point was investigated. The best results were found with the vertex fitting method, and provided a position resolution of 22 µm on a subset of the clusters. The analysis and simulation of the Timepix3 detector data lead to the publication *Antiproton tagging and vertex fitting in a Timepix3 detector*, found in appendix G.

In order to achieve the scientific goal of the AEgIS collaboration, which is to measure the gravitational acceleration on antimatter to a precision of 1%, a position resolution of around 10 µm would be needed. Preliminary simulation studies estimates that position resolutions up to 17.5 µm would also give reasonable results [9]. The absolute requirement for seeing a fringe pattern is a position resolution below the period of the moiré deflectometer, and currently a period in the range of 60–80 µm is planned. This means that the found position resolution, although it is not good enough for the optimal 1% measurement, it is approaching values where it can be very useful. The time resolution of the Timepix3 detector is 1–2 ns, and this is so six orders of magnitude smaller than the total travel time of the antihydrogen through the moiré deflectometer, the time resolution should be more than good enough.

The required position resolutions for different scenario are based upon estimated of parameters that are not exactly known today, for instance the exact geometry of the moiré deflectometer and the velocity, temperature, and flux of the antihydrogen beam. When the antihydrogen beam has been demonstrated, and its parameters are exactly known, an important next step would be to repeat the simulation effort to see what can be achieved in terms of accuracy on $\bar{g}$ with the 22 µm position resolution.

Based on the current knowledge of how the final gravity experiment will be built, the achieved position resolution needs to be improved by at least 5 µm. This can be done by improving the detector construction, and by improving the reconstruction methods. It was shown in chapter 7 that longer prongs did not provide better vertex reconstruction. This was counter intuitive, but is likely because longer tracks also gives more scattering. This is something that should be studied further. If this turns out to be the explanation, it would be good to look into the possibility to build a telescope detector with many thin layers to reduce the interaction between the annihilation fragments and the detector material.

Another important outcome of the Timepix3 study is that it provides the whole pipeline for a detector study of antiproton annihilation in a pixel detector. It starts with the data collection, data cleaning, and preprocessing. Then the detector response model is developed and tested against data, and eventually it is used to predict the performance of the detector in terms of tagging efficiency and annihilation point reconstruction. There are possibilities for improvements and changes in many of these steps. With the full pipeline in place it should be possible to insert any change in the individual steps and then run the whole pipeline to see the effect of these changes on the final parameters like the tagging efficiency and position resolution. To help achieve this outcome the source code, technical documentation, and user manuals for all software developed are provided such that anyone can reproduce the pipeline.

A. Simulation of the incoming beam to GRACE.

The simulation program documented here is called **DegraderSimu** and it simulates the interaction of the antiprotons in the degrader foil, air gap, and vacuum windows between the AD and GRACE.

The **DegraderSimu** program uses the Geant4 framework [22], and for the work in this thesis version Geant4.10.4 was used. It is important to use this version or newer version, since the energy loss model in older versions had a bug in the energy loss model that only revealed itself when using the single scattering model at low energies [48]. The bug was found and resolved in collaboration with the Geant4 team when data was compared to simulations for the flux on the end plate as described in chapter 4.

The Geant4 framework is commonly used in high energy physics to simulate the interaction of particles with matter. By providing the geometry, material, physics list, and the definition of the particles of interest, Geant4 can simulate the passage of these particles through the geometry. Interactions between the particle and the material such as energy loss, scattering, and annihilations, are simulated using the Monte Carlo method. Information about the state of the particle can be obtained at any point of the geometry.

The **DegraderSimu** simulates antiprotons of energy 5.3 MeV coming from the AD, this energy corresponds to the energy of the AD-beam, and tracks them through the three foils and the air that separates the vacuum of AD and GRACE. This geometry is described in section 4.2. The antiprotons are scattered, loses energy and is possibly annihilated in the foils and the air gap. The output of the simulation is the energy, position and momentum direction right after the particles have entered GRACE through the circular window with a diameter of 4 cm. For the **GraceBeam** simulation these parameters has to be known, and therefore this simulation provides the input to the **GraceBeam** simulations documented in appendix B. The degrader thickness is an input parameter to the simulation and can therefore easily be altered.

A.1. How to run the simulation

This section shows step by step how **DegraderSimu** can be installed and ran. As a prerequisite Geant4 needs to be installed. Geant4 can be downloaded from `http://geant4.cern.ch` and installed according to the instructions found there.

A.1.1. Installing the simulation package

Before we start the Geant4 environment has to be set.

```
source <path>/geant4.sh
```

Then make a folder to run all the simulations in and make a build directory in this folder.

```
mkdir DegraderSimulation
cd DegraderSimulation
mkdir build-GraceDegrader
```

Clone your own version of the code from github, checkout the tag `v1.2` and see that the files and folders are there:

```
git clone https://github.com/helgaholmestad/GraceDegrader.git
git checkout v1.2
cd GraceDegrader
ls
AntiPcells.cc  CMakeLists.txt  include  instructions  makefile  src  vis.mac
```

The simulation can then be configured in the build-GraceDegrader folder using cmake:

```
cd ../build-GraceDegrader
cmake ../GraceDegrader
```

A successful cmake build should show an output similar to this:

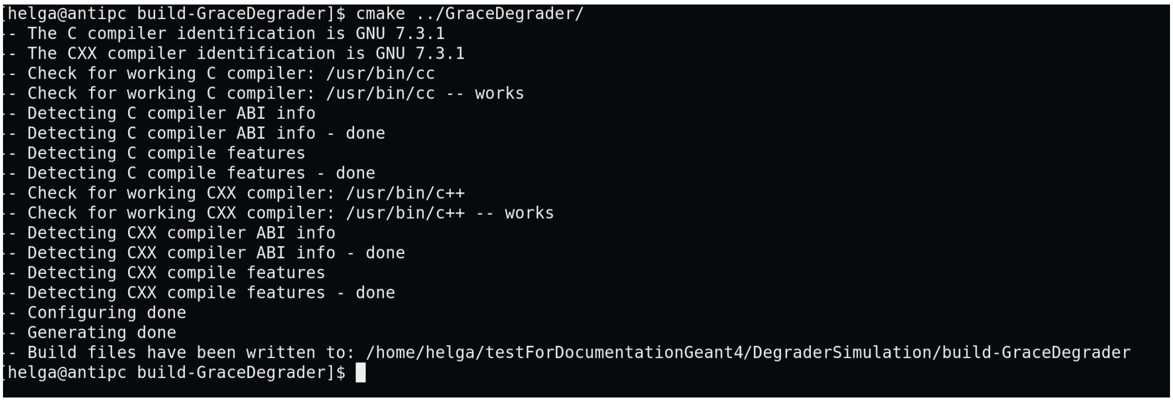

```
[helga@antipc build-GraceDegrader]$ cmake ../GraceDegrader/
- The C compiler identification is GNU 7.3.1
- The CXX compiler identification is GNU 7.3.1
- Check for working C compiler: /usr/bin/cc
- Check for working C compiler: /usr/bin/cc -- works
- Detecting C compiler ABI info
- Detecting C compiler ABI info - done
- Detecting C compile features
- Detecting C compile features - done
- Check for working CXX compiler: /usr/bin/c++
- Check for working CXX compiler: /usr/bin/c++ -- works
- Detecting CXX compiler ABI info
- Detecting CXX compiler ABI info - done
- Detecting CXX compile features
- Detecting CXX compile features - done
- Configuring done
- Generating done
- Build files have been written to: /home/helga/testForDocumentationGeant4/DegraderSimulation/build-GraceDegrader
[helga@antipc build-GraceDegrader]$ 
```

The simulation program can now be compiled:

```
make
```

You will see some warnings about unused variables, but this causes no problems. If the compilation ends with the following lines the simulation should be properly installed.

```
                        ^~~~~~~~~~~
[ 90%] Building CXX object CMakeFiles/AntiPcells.dir/src/analysis.cc.o
[100%] Linking CXX executable AntiPcells
[100%] Built target AntiPcells
[helga@antipc build-GraceDegrader]$ ls
AntiPcells  CMakeCache.txt  CMakeFiles  cmake_install.cmake  Makefile  vis.mac
[helga@antipc build-GraceDegrader]$ 
```

A.1.2. Running the simulation

The program is run in the build-GraceDegrader folder, and can be run in interactive or batch mode. To run it in the interactive mode do:

```
./AntiPcells <degraderThickness>
```

The unit of the degrader thickness is µm, and for the experimental setup where the majority of the data was taken the degrader thickness was 33 µm. This corresponds to running the command:

```
./AntiPcells 33
```

This mode will show a an interactive window with the geometry:

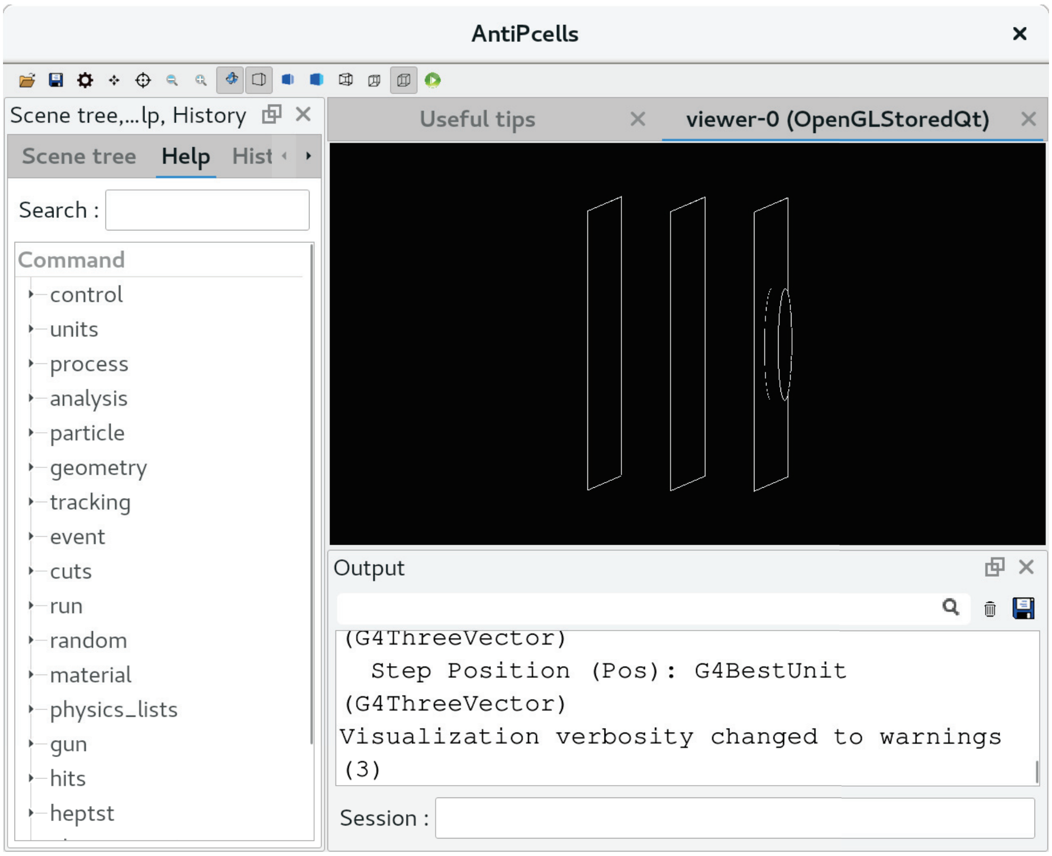

```
(G4ThreeVector)
  Step Position (Pos): G4BestUnit
(G4ThreeVector)
Visualization verbosity changed to warnings
(3)
```

Here the three different foils are clearly seen, and the circular geometry corresponds to the window into grace and has a diameter of 4 cm. In the simulation the GRACE window is a sensitive detector, and we retrieve information about the antiprotons as they exit this volume.

The commands are written in the Session box. To simulate the tracking of 100 particles through the geometry do:

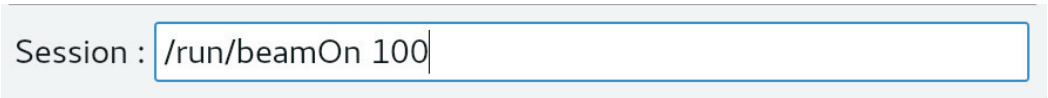

Session : /run/beamOn 100

Then the tracks of the antiprotons will appear:

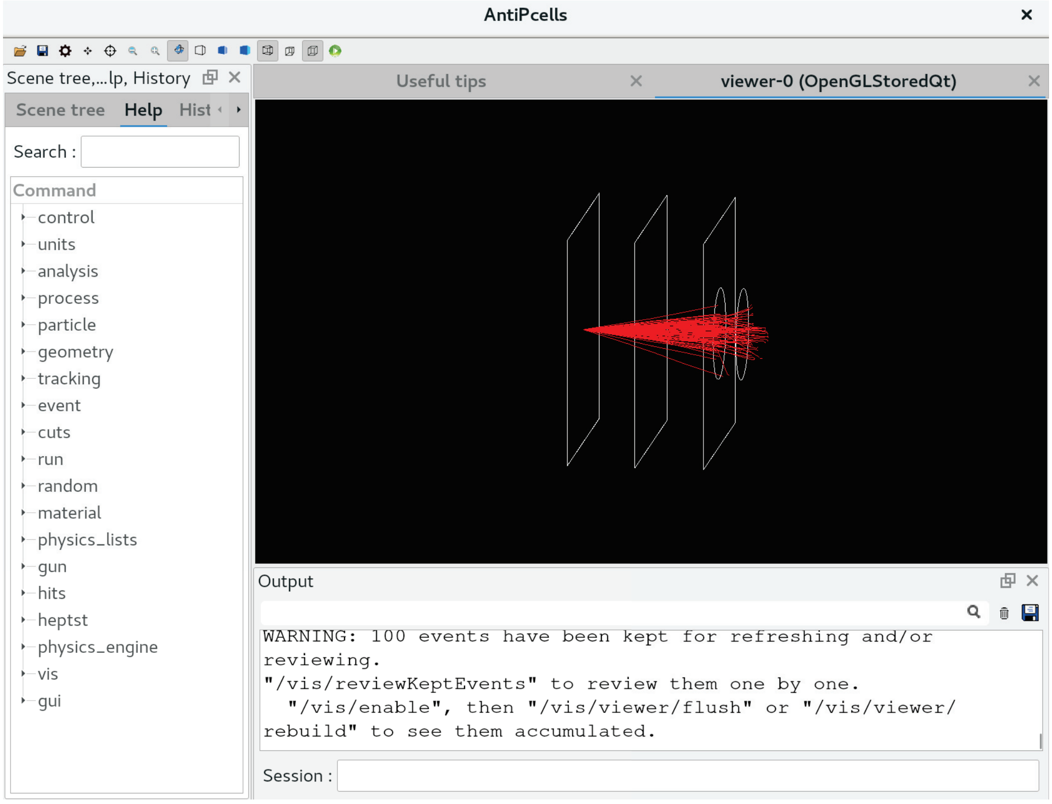

```
WARNING: 100 events have been kept for refreshing and/or
reviewing.
"/vis/reviewKeptEvents" to review them one by one.
  "/vis/enable", then "/vis/viewer/flush" or "/vis/viewer/
rebuild" to see them accumulated.
```

For simulations with many particles it is better to do it in the batch mode as the graphics is computationally heavy. To run in batch mode insert the commands that you would write in the SessionBox into a text file. Then the simulation can be run from the command line:

```
./AntiPcells <degrader thickness> <name of input file>
```

An example of an input file is included in the repository and the example can be run as:

```
./AntiPcells 33 ../GraceDegrader/input.mac
```

The output of the simulations in both modes is a file called textttDegrader.tex. This file has eight space separated columns and here is a sample of this file:

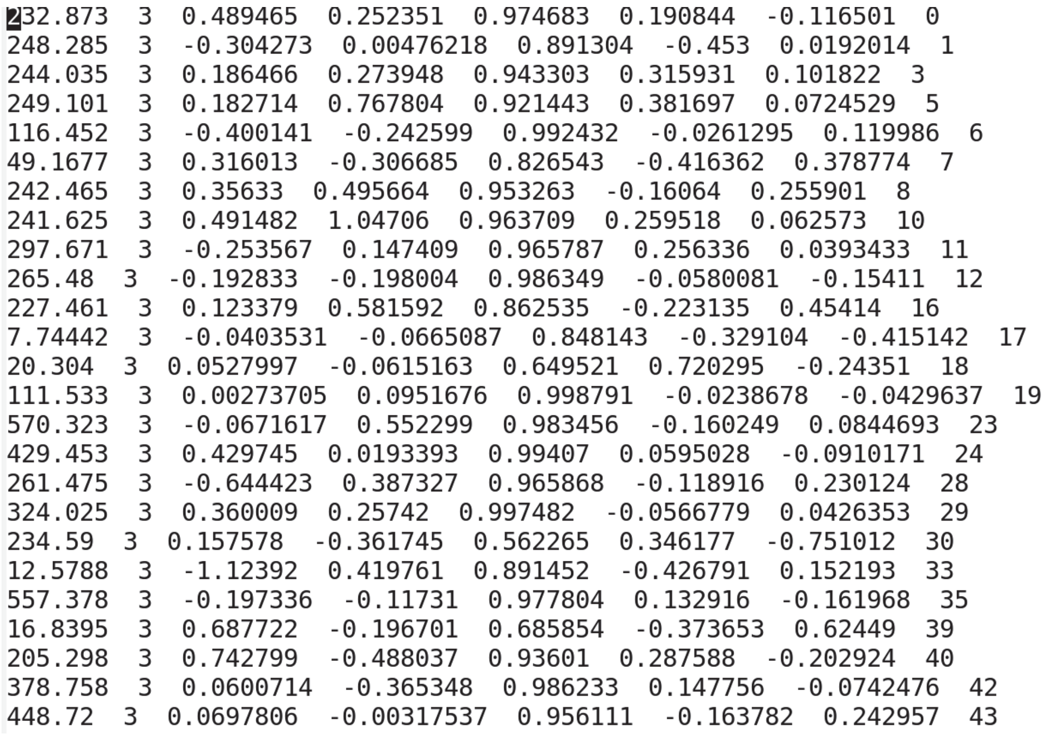

```
232.873  3  0.489465  0.252351  0.974683  0.190844  -0.116501  0
248.285  3  -0.304273  0.00476218  0.891304  -0.453  0.0192014  1
244.035  3  0.186466  0.273948  0.943303  0.315931  0.101822  3
249.101  3  0.182714  0.767804  0.921443  0.381697  0.0724529  5
116.452  3  -0.400141  -0.242599  0.992432  -0.0261295  0.119986  6
49.1677  3  0.316013  -0.306685  0.826543  -0.416362  0.378774  7
242.465  3  0.35633  0.495664  0.953263  -0.16064  0.255901  8
241.625  3  0.491482  1.04706  0.963709  0.259518  0.062573  10
297.671  3  -0.253567  0.147409  0.965787  0.256336  0.0393433  11
265.48  3  -0.192833  -0.198004  0.986349  -0.0580081  -0.15411  12
227.461  3  0.123379  0.581592  0.862535  -0.223135  0.45414  16
7.74442  3  -0.0403531  -0.0665087  0.848143  -0.329104  -0.415142  17
20.304  3  0.0527997  -0.0615163  0.649521  0.720295  -0.24351  18
111.533  3  0.00273705  0.0951676  0.998791  -0.0238678  -0.0429637  19
570.323  3  -0.0671617  0.552299  0.983456  -0.160249  0.0844693  23
429.453  3  0.429745  0.0193393  0.99407  0.0595028  -0.0910171  24
261.475  3  -0.644423  0.387327  0.965868  -0.118916  0.230124  28
324.025  3  0.360009  0.25742  0.997482  -0.0566779  0.0426353  29
234.59  3  0.157578  -0.361745  0.562265  0.346177  -0.751012  30
12.5788  3  -1.12392  0.419761  0.891452  -0.426791  0.152193  33
557.378  3  -0.197336  -0.11731  0.977804  0.132916  -0.161968  35
16.8395  3  0.687722  -0.196701  0.685854  -0.373653  0.62449  39
205.298  3  0.742799  -0.488037  0.93601  0.287588  -0.202924  40
378.758  3  0.0600714  -0.365348  0.986233  0.147756  -0.0742476  42
448.72  3  0.0697806  -0.00317537  0.956111  -0.163782  0.242957  43
```

The different columns is described in table A.1. The x position will always be at 3.0025 cm, since this is where the detector is placed. The momentum is given as the proportion of a unit vector, such that the length of the momentum vector is always 1.

Column number	Description
1	Energy of the particle [keV]
2	x-position [cm]
3	y-position [cm]
4	z-position [cm]
5	x-momentum direction
6	y-momentum direction
7	z-momentum direction
8	Event number

Table A.1.: Description of the different columns in the output file texttDegrader.tex.

A.2. Description of the main features of the simulation

This section is meant to describe what the different classes do in the program. The overview is meant to help the reader to understand the the work flow of the simulation and be able to customize it if necessary.

A Geant4 program is a framework written in C++. It therefore contains a main function steering the program, which is found in the file `AntiPcells.cc`. From this function different instances of classes are called at different points of the simulation. Table A.2 contains all user defined classes that are called during the simulation, together with a brief description of what they do and when they are called. All special considerations that had to be taken into account because we were working with a low energies, thin foils, and antiprotons are mentioned.

DetectorConstruction	Called at the start of the program. Defines the geometry. Usually also defines on or more sensitive detector. A sensitive detector is the area of the geometry where the user is interested in retrieving information from. In this program the sensitive detector is a circular area with diameter 4 cm right after the GRACE foil.

PhysicsList	An instance of this class is called as the program starts to define the interaction processes between the material and the particles. Since we are using a pre-made physics list this is done directly in the main function by:
	`G4PhysListFactory factory;`
	`G4VModularPhysicsList* phys = factory.GetReferencePhysList("FTFP_BERT");`
	`phys->ReplacePhysics(new G4EmStandardPhysicsSS());`
	`phys->RegisterPhysics(new G4EmUserPhysics());`
	`runManager->SetUserInitialization(phys);`
	The list FTFP-BERT is used as this contains annihilation of antiprotons. We are also forcing the use of single scattering instead of multiple scattering, because multiple scattering is not accurate enough for the very thin foils.

G4EmUserPhysics	As default the antiprotons annihilate when they reach an energy below 1 keV. This user implementation sets this threshold down to 10^{-6} eV.
RunAction	A run is defined as the set of particles that are simulated, and functions in this class are called at the start and end of the run. The file `Degrader.tex` is created at the start of the run and closed at the end.
PrimaryGeneratorAction	Defines the incident particles. In our setup this is a simple 5.3 MeV point beam at position (-3 cm,0,0) with momentum vector (1,0,0).
EventAction	An event is defined as the simulation of one particle trough the geometry. An event always starts with generating a particle as defined in the PrimaryGeneratorAction class. It is implemented that at the end of each event information about the antiprotons as they go out of the Grace window is written to file.
SteppingAction	The particles iterate through the material in steps, and at each step a stochastic process such as energy loss or multiple scattering can happen. In the program it is implemented that an event is aborted when the antiproton annihilates. This saves large amount of computation time since we avoid tracking all the annihilation products.
AntiPSD	An instance of this class is called every time a particles makes a step in the sensitive detector. Information about the energy, momentum and position of the particle is here added to the hit collection.

AntiPHit	The AntiPSD class calls functions in this class to add information to a hit collection. There is one hit collection for every event.
analysis	Singelton class that takes care of writing the interesting information from the hit collection to file. Here the actual implementation of writing to file is found, and functions in this class is called from the classes runAction and EventAction.

Table A.2.: Description of the different classes in the simulation program. Information about when functions in the classes are called, what they do and how they are customized to low energy antiprotons in thin foils.

B. Simulation of the GRACE beam line

The simulation program **GRACESimu** simulates the track of the particles inside of GRACE. It is built using the library IonBeam simulator (`IBSimu`) [46], which is a C++ library for for doing 3D simulation of electrostatic optics for charged particles.

The general setup of a simulation using `IBSimu` is the following: First the geometry of the experimental setup and the electric potential applied to each component is defined by the user. The user also defines the particles that should be tracked by giving their position, momentum, energy, charge, and mass at the starting point. Then `IBSimu` calculates the electric field in the defined experimental setup by numerically solving the Poisson equation using a finite difference method. At the end the particles are tracked trough the experimental setup using the Runge-Kutta method to solve the equation of motions. At any point along the track the state of the particle can be extracted.

The program **GRACESimu** implements this procedure for the geometry of GRACE. The input is the beam as it enters GRACE, meaning the input is the output from the **DegraderSimu** program. The output is the state of the particles as they hit any hard surface of GRACE. The geometry of the simulation is made such that the detector plane is at the end of the extraction line, and in this way information about the particles in the detector plane can be collected.

To download the IBSimu library go here: `http://ibsimu.sourceforge.net/download.html`. Instruction for installing the program with all its prerequisites is here: `http://ibsimu.sourceforge.net/installation.html`. For this example and the work of this thesis `ibsimu-1.0.6` was used.

B.1. Running the program

The **GRACESimu** program can be downloaded from Github in the repository named `GRACEbeamline`. Clone this repository and checkout tag `v1.1`, navigate to the `simulation` folder and check that all files are there.

```
git clone https://github.com/helgaholmestad/GRACEbeamline.git
git checkout v1.1
cd GRACEbeamline/simulations
ls
analysis.cpp                   inputfiles     loopVoltages.sh
findHitsInDetectorPlane.py     loopScan.sh    Makefile  simu.cpp
README.md
```

If another version of IBSimu is used, one needs to change the IBSimu version in the Makefile. The file `simu.cpp` contains the code that implements the geometry and the tracking of the particles. The simulation is compiled and run by the following command:

```
make
./simu D1 D2 E1 E2 inputfil outputfolder outputname
```

The explanation of the input variables is found in table B.1.

Name	Description
D1	Potential on D1 in V
D2	Potential on D2 in V
E1	Potential on E1 in V
E2	Potential on E2 in V
inputfile	The definition of the particles as they enter GRACE, this is the output from the **DegraderSimu** program
outputfolder	A folder where the output file will be written to. This folder has to exist before the program is run
outputname	An extension that is added to name of the outputfile.

Table B.1.: Explanation of the input variables to the **DegraderSimu** program.

A test inputfile consisting of 5000 antiprotons is found in the folder `inputfiles`. To run the simulation in the setting D_1=0, D_1=4 kV, E_1=4 kV, E_2=4 kV with the example inputfile do:

```
make
mkdir output
./simu 0 4000 4000 4000 inputfiles/testData.txt output test
```

This will result in the file `D1_0D2_4000E1_4000E2_4000_scanningtest.txt` in the folder `output`. As seen the file name contains information about the voltages applied to the electrodes. The output file has the following format:

```
-0.0646884  -0.00635098     0.216698  8.16357  216.203  initial 7.984790  3.000000  0.165374  0.160135  0.958666  -0.282619  -0.032947
-0.0471698    0.0497768 -7.82461e-07  11.1211  49.3167  initial 11.178900  3.000000  0.008536  -0.361915  0.167904  -0.653226  0.738312
 0.0648033  -0.00503579     0.243682  4.28857  385.444  initial 4.264250  3.000000  -0.303774  -0.123173  0.953798  0.299578  -0.022840
-0.0419013   -0.0496913    0.0105694  12.4184  42.9533  initial 12.496000  3.000000  -0.309322  -0.024272  0.334651  -0.581608  -0.741445
-0.0378919    0.0528027    0.0234933  1.99433  120.581  initial 2.148260  3.000000  -0.055215  0.208186  0.634056  -0.459914  0.621652
```

The three first columns is the position (x,y,z) in cm of the particles as they are stopped by any of the hard surfaces inside of GRACE. Column 4 is the kinetic energy in keV and column 5 is the time in ns that it takes for the particles to travel from the entrance of GRACE to the surface where they are stopped. The parameters after the column named `inital` is just a repetition of the line defining the particle in the inputfile.

Usually it is interesting to find the particles that actually end up in the detector plane. In the simulation the detector plane is at the end of the extraction line, so the particles are stopped here and written to file. A small python script was written to filter out the particles that ends up in the detector plane. This program is called `findHitsInDetectorPlane.py` and can be run as:

```
python findHitsInDetectorPlane.py inputfile outputfile
```

For the example simulation this program is run as:

```
python findHitsInDetectorPlane.py output/D1_0D2_4000E1_4000E2
_4000_scanningtest.txt particlesOnDetector.txt
```

In the file `particlesOnDetector.txt` now consist of only the three particles that makes it to the detector plane:

```
0.614458    0.0294305     1.18336  4.26177  1992.46  initial 4.264250  3.000000  -0.303774  -0.123173  0.953798  0.299578  -0.022840
0.605777   -0.0210164     1.19063  4.29489  1904.75  initial 4.302420  3.000000  0.040214  -0.308617  0.989834  -0.029629  0.139108
0.598242    0.0449757     1.19698  4.25528  1920.13  initial 4.259040  3.000000  -0.064945  0.161956  0.981463  0.074944  -0.176392
```

This file has exactly the same format as the output from the **GRACESimu** program, but contains only the lines corresponding to the particles that made it to the detector plane.

The program `analysis.cpp` provides a graphical display of the geometry and the tracks of the particles. The program is run by the command

```
./analysis geom.dat epot.dat pdb.dat
```

Figure B.1a shows the GUI in the default setting where the geometry is shown in the xy view, and only 1 out of every 11 tracks are drawn. The fraction of tracks to be shown can be changed by clicking Edit->Preference->Geometry->Trajectory division. As default the trajectory division is set to 11, and by setting this to 1 all tracks are drawn. As shown in figure B.1a the projection can also be changed. Figure B.1b shows the GUI in the zx view and with all tracks drawn.

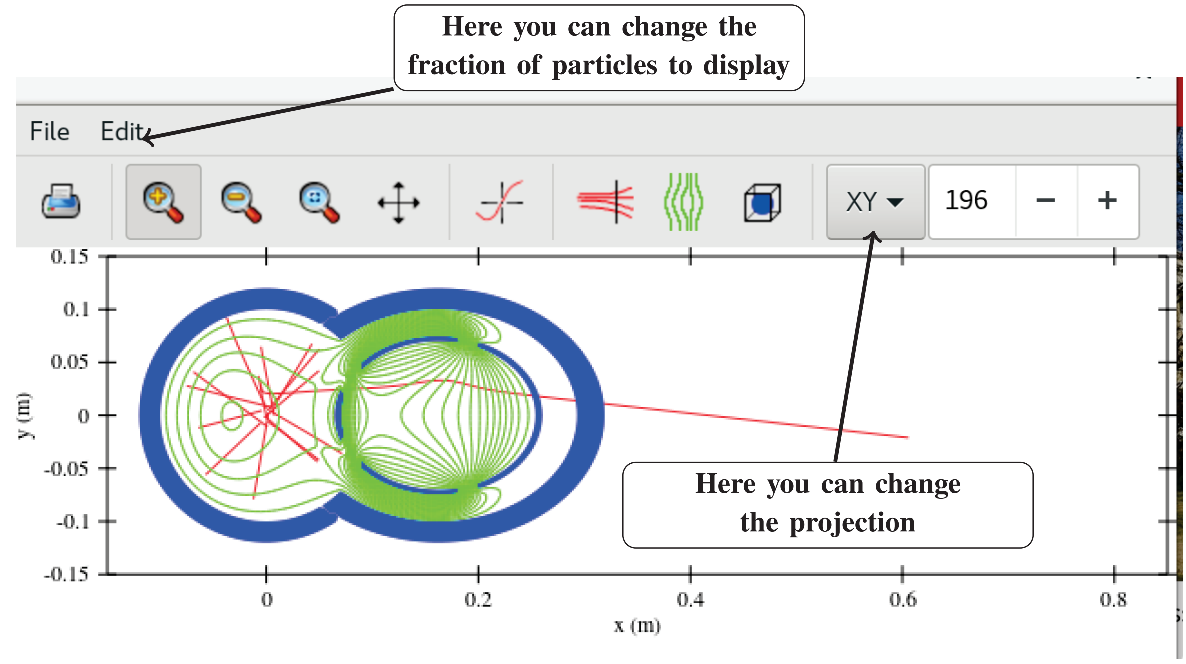

Here you can change the fraction of particles to display

Here you can change the projection

(a) The GUI in the default setting

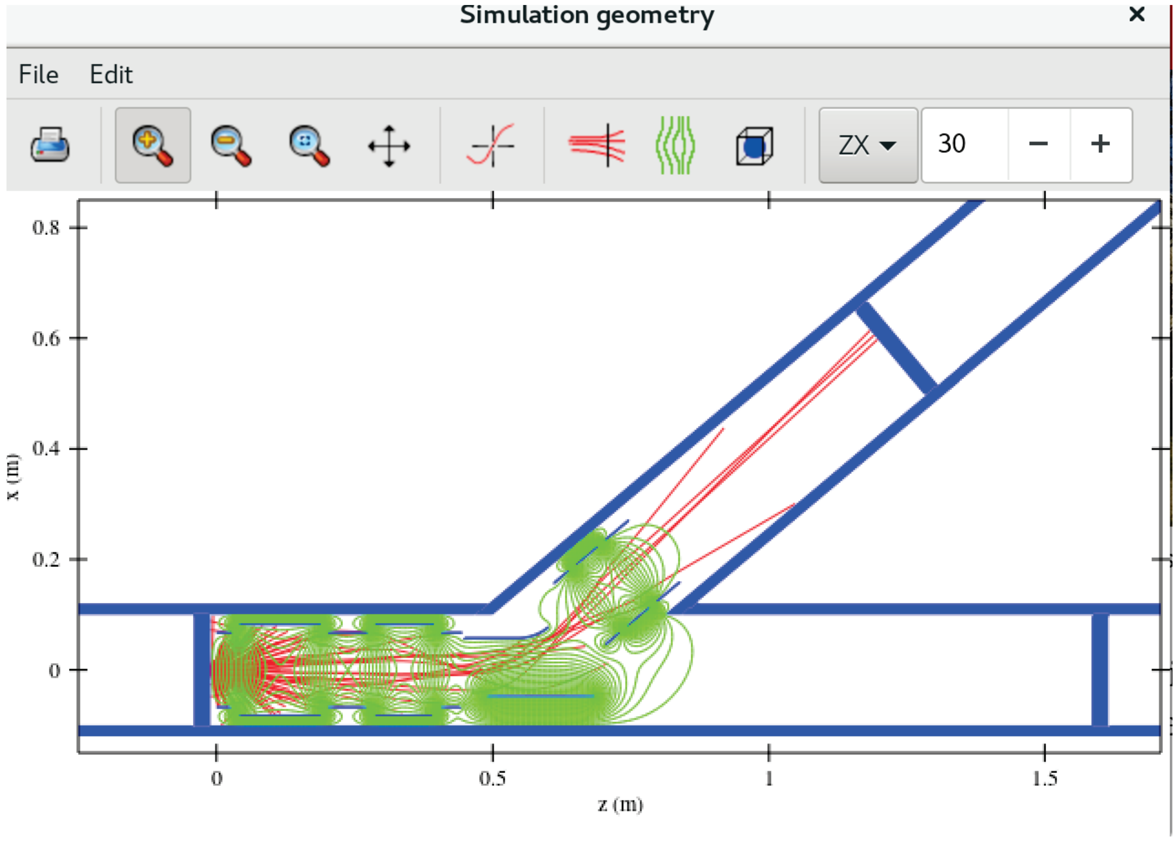

(b) Better setting to understand what is going on

Figure B.1.: The graphical interface for **GRACESimu**.

C. Characterization of the clusters

This appendix documents how the code for doing the preprocessing, clustering and characterization of the Timepix3 data can be executed by walking through the procedure on a small test data set. The code is written in Python with ROOT, therefore both Python and ROOT needs to be installed. ROOT can be downloaded from `https://root.cern.ch/`. The code was run with Python verison 2.7.14 and root version 6.10.

The input to the analysis is the raw data from the Timepix3 detector in ascii files, and the analysis is done in three steps. The first step is the energy cut and the clustering, the second step is to write the clusters to ROOT files, and the third step is to do the characterization of the clusters.

The output of the whole analysis is a file containing the following information for each cluster: cluster size, number of prongs, the χ^2 square value of the linear fit, deposited energy in the whole cluster, and deposited energy in the center of the cluster.

The code for the data analysis is found in the git repository `finalTimepix`, where a small data set is included for test purpose. To execute the code clone the repository and checkout tag `v1.1`, navigate to the `dataAnalsyis` folder, and check that all files are there:

```
git clone https://github.com/helgaholmestad/finalTimepix.git
git checkout v1.1
cd finalTimepix/dataAnalysis
ls
checksSimularity.py      compareReferenceMain.py
hough1D.pyc              loopClusters.py
loopReversed.py          preprocess.py
runReversed.sh           clusterinNotParalell.py
hough1D.py               illustrateCharaterization.py
loopHough.py             makeStatistics.py
runHough.sh              testData
```

The folder `testData` contains a small part of the full data set from the Timepix3 detector. The data files from the Timepix3 detector are ascii files named `data_<i>.dat`, where `<i>` is the file number, and a single file corresponds to one spill of antiprotons. A data file has in total 8 columns, and the relevant fields are explained in table C.1.

Step one is to do the halo cut and the clustering. This can be done with the Python script `preprocess.py` and the path of the folder containing the data as the input parameter.

```
python preprocess.py testData
```

This script makes a new file named `clustering<i>.dat` for each input data file and

Column	Description
1	Pixel number in x
2	Pixel number in y
5	Deposited energy in keV
6	Time of arrival in ns

Table C.1.: Description of the relevant fields in the Timepix3 raw data files.

places it in the same sub folder as the input data file[1]. In the clustered data there is one one row for each pixel, only the relevant fields are kept and the data is sorted by the clusters. Each cluster starts with the line `new cluster <T>`. The variable T gives the time of arrival in ns of the first peak in the time of arrival distribution of the relevant spill, therefore this number is the same for all clusters from the same spill. The definition and explanation of the two different peaks in the time of arrival distribution is found in section 4.4.1. Below is an excerpt from a clustered data file:

```
new cluster 146585.0
0 226  8.006  148387.6047
1 224  26.936  148390.1047
1 223  22.975  148392.7246
0 224  19.661  148389.1008
2 223  28.243  148393.1605
0 225  53.921  148390.6601
2 222  41.897  148393.2563
new cluster 146585.0
55 30  8.618  148418.4401
55 31  47.854  148421.9326
54 31  7.68  148419.93
new cluster 146585.0
52 90  35.473  147191.5262
52 88  59.896  147192.2093
52 91  40.387  147194.8193
51 93  23.513  147198.4682
52 89  53.334  147191.9703
```

Step two is to put the clustered data into ROOT files using the Python script `loopClusters.py`, also with the name of the folder containing the data as the input parameter. Here also the time cut described in section 5.2 is performed, as only the clusters passing the time cut is written to file.

```
python loopClusters.py testData
```

Storing the data in ROOT files is beneficial because they are faster to read from than ascii, and one can inspect them visually by using a TBrowser. In the ROOT files there is one histogram per cluster, and one example of a cluster is seen in figure C.1.

---

[1] The program takes quite some time, and the script paralellClustering.py shows an example how how the process can be parallelized using the Python library parallel python. However, this script only runs with Python2 as this specific library is not available in Python 3.

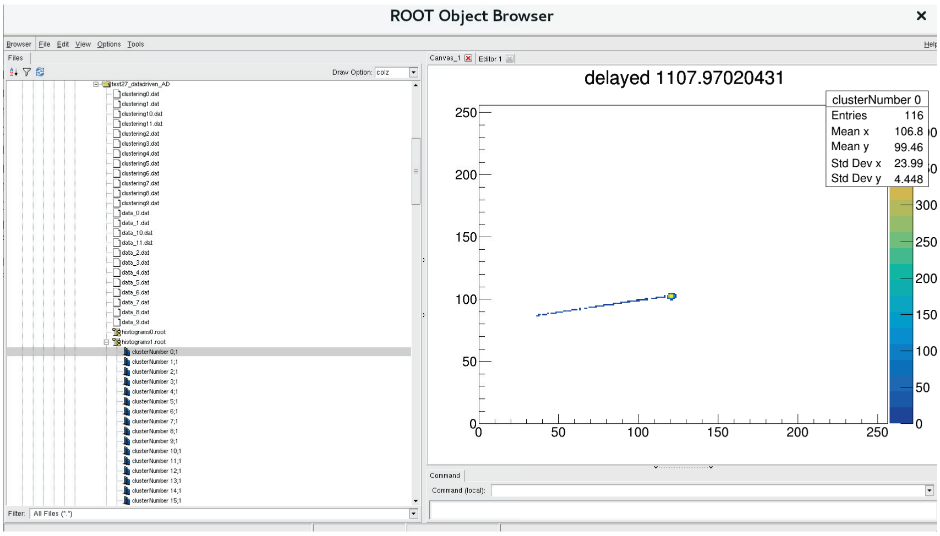

Figure C.1.: Example of how the clusters can be inspected using a TBrowser.

Step three is to do the characterization as described in section 5.4. The information about the clusters is written to a text file placed in the folder `datafiles`. This folder must be made before the program is executed, and the program is excecuted as:[2]

```
mkdir datafiles
python loopHough.py testData
```

The outputfile is found in the folder `datafiles` and has the name `meta<dataFolder>.txt`, in this example the name of the file will then be `metatestData.txt`. This means there is one output file per folder of input data. Since one folder of input data often contains all data from one experimental setup, this is a convenient way naming the output data. Below is an excerpt from the file `metatestData.txt`:

```
newCluster
energy 456.977
pixels 88.0
prong 2
prongLenght 1784.74788135  1311.95464861
clusterCharge 2097.256
error 1.08688638309
trough
newCluster
energy 1318.362
pixels 26.0
prong 0
prongLenght
clusterCharge 1871.285
```

---

[2] There will be some warnings from the Python library polyfit, claiming that the data is not good for a linear fit. These warning is not an actual problem since they might appear when the pixels making up the cluster is not appropriate for making a linear fit. For the majority of the clusters the pixels don't make up something close to a straight line, the linear fit is made to tag the cluststers where this indeed is the case since those clusters are unlikely to be annihilation clusters. This is described in section 5.4.

```
error 0.737368342684
notTrough
newFile
newCluster
```

The line `newCluster` marks that there is a new cluster, and then follows all the information about that clusters. The line `newFile` indicates that also a new file is processed, and in the current data structure this corresponds to a new spill from AD. The explanation for all the cluster variables is found in table C.2.

Variable name	Description
energy	Energy deposited in the center of the cluster [keV]
pixels	Number of pixels in the cluster
prong	Number of prongs in the cluster
clusterCharge	Energy deposited in the whole cluster
error	The χ^2 value of the linear fit of the cluster
trough/notTrough	Indicates if the cluster got through the 70 pixel and 1 prong cut

Table C.2.: Explanation of the output variables in the metaTestdata.txt file.

D. Simulation of the annihilation events

This appendix walks trough how an ensemble of 100 simulated clusters is made. The simulation software FLUKA is used to generate the raw energy depositions that will be post processed, and is therefore a prerequisite. FLUKA can be downloaded from `http://www.fluka.org/fluka.php`, and installed according to the instructions on the web page. For this example and the in the work presented in this thesis, the FLUKA version fluka-2011.2x-1.x86_64 installed via RPM was used. The code for post processing is written in Python with ROOT, therefore both Python and ROOT needs to be installed. ROOT can be downloaded from `https://root.cern.ch/`. The code was run with Python version 2.7.14 and ROOT version 6.10.

D.1. Creating the simulated clusters

The first step is to use FLUKA to simulate the raw energy depositions. Start by cloning the `finalTimepix` repository if it is not done, checkout the tag `v1.1` and navigate to the `runningFLUKA` folder:

```
git clone https://github.com/helgaholmestad/finalTimepix.git
git checkout v1.1
cd finalTimepix/simu/runningFluka
ls
instructionsTruth.txt  supersimpelTimepixCenterCa.inp
instructions.txt       supersimpelTimepixCenterCalium.inp
makeTruth.py           supersimpelTimepixCenterGold.inp
mgdraw-pix.f           supersimpelTimepixCenter.inp
testPion.inp           supersimpelTimepixLayers.inp
timepixExample.inp
```

The file `timepixExample.inp` defines the detector, the impinging antiprotons and the voxels where the energy depositions is recorded. To run the FLUKA simulation do:

```
$FLUPRO/flutil/rfluka -N0 -M1 timepixExample.inp
```

This will create a file named timepixExample001_fort.22 This file contains information about the energy deposited in the voxels for each annihilation event, and is the file that will be post processed.

The first step of the post processing is to simulate the charge sharing by doing a Gaussian blur. The folder for the processed files is named `datafiles` and should be created before the post processing starts. Navigate one folder up to the `simu` folder, create the `datafiles` folder and run the Gaussian blur with the FLUKA output as the first input parameter. The second input parameter just makes an extension to the name of the output file and is used when running many files in parallel.

```
cd ..
pwd
/pathToRepo/finalTimepix/simu
mkdir datafiles
python GaussianBlurTCAD.py runningFLUKA/timepixExample001_fort.22 1
```

This program creates a ROOT file `histogramsTCADRaw1.root` in the folder `datafiles`. The ROOT file contains histograms of the simulated annihilation clusters. There is one histogram per cluster, one bin per pixel and the content of the bin is the deposited energy in that pixel. These histograms can be inspected by using ROOT's `TBrowser`, and one example is shown in figure D.1

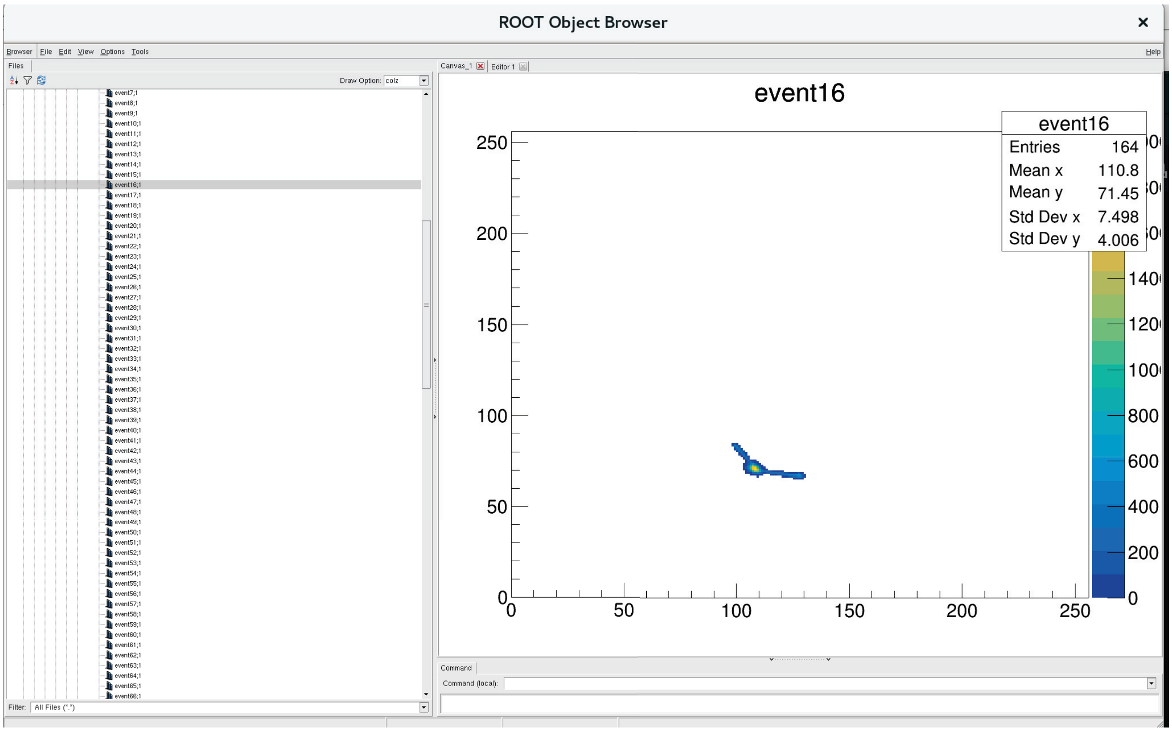
Draw Option: colz

event16
Entries 164
Mean x 110.8
Mean y 71.45
Std Dev x 7.498
Std Dev y 4.006

Figure D.1.: Example of one simulated cluster

The next step is to take the volcano effect and the suppressed pixels into account as explained in section 6.1.2. For this example the data used for sampling the suppressed pixels is taken from the test data set. Therefore the clustering of the test data should be done before this step can be carried out. This is first step of the characterization as discussed in appendix C. The step is done by running the command `python preprocess.py testData` in the `dataAnalysis` folder, and if it is not done the program `reCluster.py` will be stuck in an infinite loop.

The code for simulating the volcano effect and the suppressed pixels is in the file `reCluster.py`. The input parameter is the extension to the file name used for the Gaussian blur. Since the suppressed pixels might divide one cluster into two or more, this code includes doing the same clustering as was done in appendix C for the real data.

```
python reCluster.py 1
```

The output of this code is the file `histograms1TCADFinal.root` in the `datafiles` folder. This file contains the histograms of the simulated clusters when the charge sharing, the volcano effect and the suppressed pixels has been taken into account.

To do the analysis to find the cluster variables the program `hough1D.py` is ran. The input parameter to this program is the ROOT file containing the clusters and a unique name to identify the output files.

```
pwd
pathToRepo/finalTimepix/simu
python hough1D.py datafiles/histograms1TCADFinal.root datafiles/meta
```

The `meta.txt` file has exactly the same format as the output file of the analysis of the real data as shown in appendix C. In addition a file named `metaprong.txt` is produced in the folder `datafiles`. This file contains information about the detected prongs in the cluster. The format is the following:

```
new cluster
center 198.311141025  172.796297525
pixel  198  178  56.37972298
pixel  198  179  118.889035307
pixel  198  180  188.773777375
pixel  198  181  215.906299437
  |     |    |     |
  |     |    |     |
pixel  208  206  5.21709037617
pixel  208  207  8.67553626524
pixelsInProng  103
pixel  197  166  27.1936264799
pixel  197  167  136.187449646
  |     |    |     |
  |     |    |     |
pixelsInProng  41
numberOfProngs 2
done
new cluster
```

The first line that starts with `center` gives the mass center. The positions is given as the pixel number such that the center of the pixel in the lower left corner is at position (1,1). Then follows information about the pixels making up the prong, first the position and then the deposited energy in keV in the pixel. Each prong ends with information about the number of pixels making up this prong, and each cluster ends with information about the number of prongs in the cluster. This output file will later be used to reconstruct the annihilation point by the vertex fitting method.

D.2. Extracting truth information

In order to access the truth information about the annihilation point the user routine MGDRAW needs to be compiled, and then FLUKA should be ran with this user routine.

```
cd /pathToRepo/finalTimepix/simu/runningFluka
$FLUPRO/flutil/ldpmqmd -o exe mgdraw-pix.f
$FLUPRO/flutil/rfluka -e exe -N0 -M1 timepixExample.inp
```

The truth information is written to the `timepixExample001.log` file. A small Python script writes the truth information to a nicely formatted text file taking the log file and name of the output file as input parameters

```
python makeTruthExample.py timepixExample001.log truth.txt
```

The output file `truth.txt` has the format:

```
0 191.171365694  158.393974362
1 191.348774523  230.587351091
2 194.776192675  222.238588834
3 35.756368491  195.160570002
4 20.8085729225  189.538836243
5 245.867519133  33.5219841569
6 235.849257887  97.9953209373
```

The first column is the event number and then follows the x and y position of the annihilation point. The positions is again given as the pixel number such that the center of the pixel in the lower left corner is at position (1.0,1.0).

D.3. Reconstructing the annihilation point

A small example of how the do the vertex reconstruction on the simulated data is included. Navigate to the vertex fitting folder and run the program `vertexFittingExample.py` with the file containing the prong data and a chosen name for the output file as input parameters.

```
cd /pathToRepo/finalTimepix/simu/vertexFitting
python vertexFittingExample.py ../datafiles/metaprong.txt results.txt
```

The output file has the following format: For each cluster it contains information about the mass center, and then the reconstructed annihilation point for each possible combination of two prongs is given. The positions is as before the pixel number such that the center of the pixel in the lower left corner is at position (1.0,1.0). The fourth column is the angle in degrees between the two prongs that are used to reconstruct the relevant annihilation point.

```
new cluster
massCenter  22.0000646174  190.061284111
vertex 29.1588593286  187.624872797  85.0049825179
vertex 21.6411245815  190.748511311  59.0369651056
vertex 21.3641502937  190.863594854  71.2237611531
vertex 23.7976664964  189.852462486  26.0654535817
vertex 22.3587103983  189.777827138  54.0419476235
vertex 18.2857278167  191.06734971  76.2187786352
vertex 23.3548393875  189.462448717  31.0604710639
vertex 21.5659208194  190.850240052  40.2607262587
vertex 22.8927309522  189.055453191  4.89758131267
vertex 24.6953758855  190.643107447  44.8416924286
new cluster
```

```
massCenter  246.148465667  34.4935013328
vertex 246.917680894  34.4842538631  8.63975752901
vertex 246.145371006  33.9513295562  52.6518560015
vertex 246.558949037  35.2208249113  45.9879015275
new cluster
```

Bibliography

[1] Carl D. Anderson. The positive electron. *Phys. Rev.*, 43:491–494, Mar 1933.

[2] P.A.M.Dirac. The quantim theory of the electron,. *Proceedings of the Royal Society of London*, vol. 177:610–624, 1928.

[3] David J Griffiths. *Introduction to elementary particles; 2nd rev. version*. Physics textbook. Wiley, New York, NY, 2008.

[4] G. B Andresen et al. Confinement of antihydrogen for 1,000 seconds. *Nat. Phys.*, 8, 2011.

[5] M. Hori and J. Walz. Physics at cern's antiproton decelerator. *Progress in Particle and Nuclear Physics*, 72:206 – 253, 2013.

[6] P. Belochitskii, T. Eriksson, and S. Maury. The cern antiproton decelerator (ad) in 2002: status, progress and machine development results. *Nuclear Instruments and Methods in Physics Research Section B: Beam Interactions with Materials and Atoms*, 214:176 – 180, 2004. Low Energy Antiproton Physics (LEAP'03).

[7] Esma Anais Mobs. The CERN accelerator complex. Complexe des accélérateurs du CERN. Oct 2016. General Photo.

[8] Clifford M. Will. The confrontation between general relativity and experiment. *Living Reviews in Relativity*, 17(1):4, Jun 2014.

[9] G. Dobrychev et al. Proposal for the AEGIS experiment at the CERN Antiproton Decelerator (Antimatter Experiment: Gravity, Interferometry, Spectroscopy). 2007.

[10] Markus K. Oberthaler, Stefan Bernet, Ernst M. Rasel, Jörg Schmiedmayer, and Anton Zeilinger. Inertial sensing with classical atomic beams. *Phys. Rev. A*, 54:3165–3176, Oct 1996.

[11] S Aghion, O Ahlen, C Amsler, A Ariga, T Ariga, A S Belov, K Berggren, G Bonomi, P Braunig, J Bremer, R S Brusa, L Cabaret, C Canali, R Caravita, F Castelli, G Cerchiari, S Cialdi, D Comparat, G Consolati, H Derking, S Di Domizio, L Di Noto, M Doser, A Dudarev, A Ereditato, R Ferragut, A Fontana, P Genova, M Giammarchi, A Gligorova, S N Gninenko, S Haider, T Huse, E Jordan, L V Jørgensen, T Kaltenbacher, J Kawada, A Kellerbauer, M Kimura, A Knecht, D Krasnicky, V Lagomarsino, S Lehner, A Magnani, C Malbrunot, S Mariazzi, V A Matveev, F Moia, G Nebbia, P Nedelec, M K Oberthaler, N Pacifico, V Petracek, C Pistillo, F Prelz, M Prevedelli, C Regenfus, C Riccardi, O Røhne, A Rotondi, H Sandaker, P Scampoli, J Storey, M A Subieta Vasquez, M Spacek, G Testera, R Vaccarone, E Widmann, S Zavatarelli, and J Zmeskal. A moiré deflectometer for antimatter. *Nature Commun.*, 5:4538. 6 p, 2014.

[12] M. Kimura, S. Aghion, O. Ahlén, C. Amsler, A. Ariga, T. Ariga, A.S. Belov, G. Bonomi, P. Bräunig, J. Bremer, R.S. Brusa, G. Burghart, L. Cabaret, C. Canali, R. Caravita, F. Castelli, G. Cerchiari, S. Cialdi, D. Comparat, G. Consolati, S. Di Domizio, L. Di Noto, M. Doser, A. Dudarev, A. Ereditato, R. Ferragut, A. Fontana, P. Genova, M. Giammarchi, A. Gligorova, S.N. Gninenko, S. Haider, S.D. Hogan, T. Huse, E. Jordan, L.V. Jørgensen, T. Kaltenbacher, J. Kawada, A. Kellerbauer, A. Knecht, D. Krasnický, V. Lagomarsino, S. Mariazzi, V.A. Matveev, F. Merkt, F. Moia, G. Nebbia, P. Nédélec, M.K. Oberthaler, N. Pacifico, V. Petráček, C. Pistillo, F. Prelz, M. Prevedelli, C. Regenfus, C. Riccardi, O. Røhne, A. Rotondi, H. Sandaker, P. Scampoli, J. Storey, M.A. Subieta Vasquez, M. Špaček, G. Testera, D. Trezzi, R. Vaccarone, and S. Zavatarelli. Development of nuclear emulsions with 1 μm spatial resolution for the aegis experiment. *Nuclear Instruments and Methods in Physics Research Section A: Accelerators, Spectrometers, Detectors and Associated Equipment*, 732(Supplement C):325 – 329, 2013. Vienna Conference on Instrumentation 2013.

[13] K.A. Olive et al. (Particle Data Group). Review of particle physics. *Chin. Phys. C*, 38:090001, 2014.

[14] T. Rohe L. Rossi, P. Fischer and N. Wermes. *Pixel Detectors: From Fundamentals to Applications*. Springer, 2006.

[15] G. Lutz. *Semiconductor radiation detectors*. Springer, 1999.

[16] et al S. Parker, C DaVia. Speed: 3d sensors, current amplifiers.

[17] C. H. Wang, K. Misiakos, and A. Neugroschel. Minority-carrier transport parameters in n-type silicon. *IEEE Transactions on Electron Devices*, 37(5):1314–1322, May 1990.

[18] Kyrre Sjobak. Full simulation of a testbeam experiment including modeling of the Bonn Atlas Telescope and Atlas 3D pixel silicon sensors. Master's thesis, University of Oslo, Norway, 2010.

[19] W. Shockley. Currents to conductors induced by a moving point charge. *Journal of Applied Physics*, 9(10):635–636, 1938.

[20] T Poikela, J Plosila, T Westerlund, M Campbell, M De Gaspari, X Llopart, V Gromov, R Kluit, M van Beuzekom, F Zappon, V Zivkovic, C Brezina, K Desch, Y Fu, and A Kruth. Timepix3: a 65k channel hybrid pixel readout chip with simultaneous toa/tot and sparse readout. *Journal of Instrumentation*, 9(05):C05013, 2014.

[21] `https://www.synopsys.com/silicon/tcad.html`. Accessed: 2017-09-13.

[22] S. Agostinelli, J. Allison, K. Amako, J. Apostolakis, H. Araujo, P. Arce, M. Asai, D. Axen, S. Banerjee, G. Barrand, F. Behner, L. Bellagamba, J. Boudreau, L. Broglia, A. Brunengo, H. Burkhardt, S. Chauvie, J. Chuma, R. Chytracek, G. Cooperman, G. Cosmo, P. Degtyarenko, A. Dell'Acqua, G. Depaola, D. Dietrich, R. Enami, A. Feliciello, C. Ferguson, H. Fesefeldt, G. Folger, F. Foppiano, A. Forti, S. Garelli, S. Giani, R. Giannitrapani, D. Gibin, J.J. Gómez Cadenas, I. González, G. Gracia Abril, G. Greeniaus, W. Greiner, V. Grichine, A. Grossheim, S. Guatelli, P. Gumplinger, R. Hamatsu, K. Hashimoto, H. Hasui, A. Heikkinen, A. Howard, V. Ivanchenko, A. Johnson, F.W.

Jones, J. Kallenbach, N. Kanaya, M. Kawabata, Y. Kawabata, M. Kawaguti, S. Kelner, P. Kent, A. Kimura, T. Kodama, R. Kokoulin, M. Kossov, H. Kurashige, E. Lamanna, T. Lampén, V. Lara, V. Lefebure, F. Lei, M. Liendl, W. Lockman, F. Longo, S. Magni, M. Maire, E. Medernach, K. Minamimoto, P. Mora de Freitas, Y. Morita, K. Murakami, M. Nagamatu, R. Nartallo, P. Nieminen, T. Nishimura, K. Ohtsubo, M. Okamura, S. O'Neale, Y. Oohata, K. Paech, J. Perl, A. Pfeiffer, M.G. Pia, F. Ranjard, A. Rybin, S. Sadilov, E. Di Salvo, G. Santin, T. Sasaki, N. Savvas, Y. Sawada, S. Scherer, S. Sei, V. Sirotenko, D. Smith, N. Starkov, H. Stoecker, J. Sulkimo, M. Takahata, S. Tanaka, E. Tcherniaev, E. Safai Tehrani, M. Tropeano, P. Truscott, H. Uno, L. Urban, P. Urban, M. Verderi, A. Walkden, W. Wander, H. Weber, J.P. Wellisch, T. Wenaus, D.C. Williams, D. Wright, T. Yamada, H. Yoshida, and D. Zschiesche. Geant4—a simulation toolkit. *Nuclear Instruments and Methods in Physics Research Section A: Accelerators, Spectrometers, Detectors and Associated Equipment*, 506(3):250 – 303, 2003.

[23] T.T. Böhlen, F. Cerutti, M.P.W. Chin, A. Fassò, A. Ferrari, P.G. Ortega, A. Mairani, P.R. Sala, G. Smirnov, and V. Vlachoudis. The fluka code: Developments and challenges for high energy and medical applications. *Nuclear Data Sheets*, 120(Supplement C):211 – 214, 2014.

[24] T. von Egidy. Interaction and annihilation of antiprotons and nuclei. *Nature*, 328, 1987.

[25] Eberhard Klempt, Chris Batty, and Jean-Marc Richard. The antinucleon–nucleon interaction at low energy: Annihilation dynamics. *Physics Reports*, 413(4):197 – 317, 2005.

[26] C. Amsler, A.V. Anisovich, C.A. Baker, B.M. Barnett, C.J. Batty, M. Benayoun, P. Blüm, K. Braune, D.V. Bugg, T. Case, V. Credé, K.M. Crowe, M. Doser, W. Dünnweber, D. Engelhardt, M.A. Faessler, R.P. Haddock, F.H. Heinsius, M. Heinzelmann, N.P. Hessey, P. Hidas, D. Jamnik, H. Kalinowsky, P. Kammel, J. Kisiel, E. Klempt, H. Koch, M. Kunze, U. Kurilla, R. Landua, H. Matthäy, C.A. Meyer, F. Meyer-Wildhagen, L. Montanet, R. Ouared, K. Peters, B. Pick, W. Popkov, M. Ratajczak, C. Regenfus, J. Reinnarth, W. Roethel, A.V. Sarantsev, S. Spanier, U. Strohbusch, M. Suffert, J.S. Suh, U. Thoma, I. Uman, S. Wallis-Plachner, D. Walther, U. Wiedner, K. Wittmack, and B.S. Zou. Annihilation at rest of antiprotons and protons into neutral particles. *Nuclear Physics A*, 720(3):357 – 367, 2003.

[27] C. Baltay, P. Franzini, G. Lutjens, J. C. Severiens, D. Tycko, and D. Zanello. Annihilations of Antiprotons at Rest in Hydrogen. 5. Multipion Annihilations. *Phys. Rev.*, 145:1103–1111, 1966.

[28] P. Hofmann, F.J. Hartmann, H. Daniel, T. Von Egidy, W. Kanert, W. Markiel, H.S. Plendl, H. Machner, G. Riepe, D. Protić, K. Ziock, R. Marshall, and J.J. Reidy. Charged-particle spectra from antiproton annihilation at rest in a = 12–238 nuclei. *Nuclear Physics A*, 512(4):669 – 683, 1990.

[29] W. Markiel, H. Daniel, T. Von Egidy, F.J. Hartmann, P. Hofmann, W. Kanert, H.S. Plendl, K. Ziock, R. Marshall, H. Machner, G. Riepe, and J.J. Reidy. Emission of

helium ions after antiproton annihilation in nuclei. *Nuclear Physics A*, 485(3):445 – 460, 1988.

[30] S. Aghion, C. Amsler, A. Ariga, T. Ariga, G. Bonomi, P. Bräunig, R.S. Brusa, L. Cabaret, M. Caccia, R. Caravita, F. Castelli, G. Cerchiari, D. Comparat, G. Consolati, A. Demetrio, L. Di Noto, M. Doser, A. Ereditato, C. Evans, R. Ferragut, J. Fesel, A. Fontana, S. Gerber, M. Giammarchi, A. Gligorova, F. Guatieri, S. Haider, A. Hinterberger, H. Holmestad, T. Huse, J. Kawada, A. Kellerbauer, M. Kimura, D. Krasnický, V. Lagomarsino, P. Lansonneur, P. Lebrun, C. Malbrunot, S. Mariazzi, V. Matveev, Z. Mazzotta, S.R. Müller, G. Nebbia, P. Nedelec, M. Oberthaler, N. Pacifico, D. Pagano, L. Penasa, V. Petracek, C. Pistillo, F. Prelz, M. Prevedelli, L. Ravelli, B. Rienaecker, O.M. RØhne, A. Rotondi, M. Sacerdoti, H. Sandaker, R. Santoro, P. Scampoli, M. Simon, L. Smestad, F. Sorrentino, G. Testera, I.C. Tietje, S. Vamosi, M. Vladymyrov, E. Widmann, P. Yzombard, C. Zimmer, J. Zmeskal, and N. Zurlo. Measurement of antiproton annihilation on cu, ag and au with emulsion films. *Journal of Instrumentation*, 12(04):P04021, 2017.

[31] Paola Sala. Private communication by e-mail and fluka discussion forum.

[32] A.Fassò et al. The physics models of fluka: status and recent developments. *Conf. on Computing in High Energy and Nuclear Physics*, 2003.

[33] A. Gligorova, S. Aghion, A. S. Belov, G. Bonomi, P. Bräunig, J. Bremer, R. S. Brusa, L. Cabaret, M. Caccia, R. Caravita, F. Castelli, G. Cerchiari, S. Cialdi, D. Comparat, G. Consolati, J. H. Derking, C. Da Via, S. Di Domizio, L. Di Noto, M. Doser, A. Dudarev, R. Ferragut, A. Fontana, P. Genova, M. Giammarchi, S. N. Gninenko, S. Haider, H. Holmestad, T. Huse, E. Jordan, T. Kaltenbacher, A. Kellerbauer, A. Knecht, D. Krasnický, V. Lagomarsino, S. Lehner, A. Magnani, C. Malbrunot, S. Mariazzi, V. A. Matveev, F. Moia, C. Nellist, G. Nebbia, P. Nédélec, M. Oberthaler, N. Pacifico, V. Petráček, F. Prelz, M. Prevedelli, C. Riccardi, O. Røhne, A. Rotondi, H. Sandaker, M. A. Subieta Vasquez, M. Špaček, G. Testera, E. Widmann, P. Yzombard, S. Zavatarelli, and J. Zmeskal. Comparison of planar and 3d silicon pixel sensors used for detection of low energy antiprotons. *IEEE Transactions on Nuclear Science*, 61(6):3747–3753, Dec 2014.

[34] Michael H. Holzscheiter, Niels Bassler, Nzhde Agazaryan, Gerd Beyer, Ewart Blackmore, John J. DeMarco, Michael Doser, Ralph E. Durand, Oliver Hartley, Keisuke S. Iwamoto, Helge V. Knudsen, Rolf Landua, Carl Maggiore, William H. McBride, Søren Pape Møller, Jørgen Petersen, Lloyd D. Skarsgard, James B. Smathers, Timothy D. Solberg, Ulrik I. Uggerhøj, Sanja Vranjes, H. Rodney Withers, Michelle Wong, and Bradly G. Wouters. The biological effectiveness of antiproton irradiation. *Radiotherapy and Oncology*, 81(3):233 – 242, 2006.

[35] N Pacifico, S Aghion, J Alozy, Claude Amsler, A Ariga, T Ariga, Germano Bonomi, P Bräunig, J Bremer, R.S. Brusa, L Cabaret, Massimo Caccia, Michael Campbell, Ruggero Caravita, Fabrizio Castelli, Giovanni Cerchiari, K Chlouba, Simone Cialdi, Daniel Comparat, and Nicola Zurlo. Direct detection of antiprotons with the timepix3 in a new electrostatic selection beamline. *Nuclear Instruments and Methods in Physics Research Section A: Accelerators, Spectrometers, Detectors and Associated Equipment*, 03 2016.

[36] Lawrence Pinsky. Private communication by e-mail 10/10-2017.

[37] P.A. Tove and W. Seibt. Plasma effects in semiconductor detectors. *Nuclear Instruments and Methods*, 51(2):261 – 269, 1967.

[38] T.E.J. Campbell-Ricketts, M. Kroupa, and L.S. Pinsky. Spectroscopy of high-energy ions with timepix3. *Journal of Instrumentation*, 11(11):P11007, 2016.

[39] Carlos Granja, Jan Jakubek, Ulli Köster, Michal Platkevic, and Stanislav Pospisil. Response of the pixel detector timepix to heavy ions. *Nuclear Instruments and Methods in Physics Research Section A: Accelerators, Spectrometers, Detectors and Associated Equipment*, 633(Supplement 1):S198 – S202, 2011. 11th International Workshop on Radiation Imaging Detectors (IWORID).

[40] S. M. Abu Al Azm, G. Chelkov, D. Kozhevnikov, A. Guskov, A. Lapkin, A. Leyva Fabelo, P. Smolyanskiy, and A. Zhemchugov. Response of timepix detector with gaas:cr and si sensor to heavy ions. *Physics of Particles and Nuclei Letters*, 13(3):363–369, May 2016.

[41] Pierre Lansonneur. *Moiré Deflectometry with a Low-Energy Ion Beam for the AEGIS Experiment*. PhD thesis, Université de Lyon, 2017.

[42] M.J. Coursey J.S. Zucker M.A. Berger and Chang J. Estar pstar and astar: Computer programs for calculating stopping-power and range tables for electrons, protons, and helium ions., 2005.

[43] Helmut Liebl. *Applied charged particle optics*. Springer, 2007.

[44] M. Basseler et.al. Antiproton radiotherapy. *Radiotherapy and Oncology*, 86:14– 19, 2008.

[45] Alexander Sinturell. Private communication by e-mail 08/2-2016.

[46] T. Kalvas, O. Tarvainen, T. Ropponen, O. Steczkiewicz, J. Ärje, and H. Clark. Ibsimu: A three-dimensional simulation software for charged particle optics. *Review of Scientific Instruments*, 81(2):02B703, 2010.

[47] S. Aghion, C. Amsler, M. Antonello, A. Belov, G. Bonomi, R.S. Brusa, M. Caccia, A. Camper, R. Caravita, F. Castelli, G. Cerchiari, D. Comparat, G. Consolati, A. Demetrio, L. Di Noto, M. Doser, C. Evans, M. Fanì, R. Ferragut, J. Fesel, A. Fontana, S. Gerber, M. Giammarchi, A. Gligorova, F. Guatieri, Ph. Hackstock, S. Haider, A. Hinterberger, H. Holmestad, A. Kellerbauer, O. Khalidova, D. Krasnický, V. Lagomarsino, P. Lansonneur, P. Lebrun, C. Malbrunot, S. Mariazzi, J. Marton, V. Matveev, S.R. Müller, G. Nebbia, P. Nedelec, M. Oberthaler, N. Pacifico, D. Pagano, L. Penasa, V. Petracek, F. Prelz, M. Prevedelli, B. Rienaecker, J. Robert, O.M. RØhne, A. Rotondi, H. Sandaker, R. Santoro, L. Smestad, F. Sorrentino, G. Testera, I. C. Tietje, E. Widmann, P. Yzombard, C. Zimmer, J. Zmeskal, and N. Zurlo. Antiproton tagging and vertex fitting in a timepix3 detector. *Journal of Instrumentation*, 13(06):P06004, 2018.

[48] Geant4 team. Geant4 relase notes version 10.3 patch 2. `http://geant4.web.cern.ch/geant4/support/Patch4.10.3-2.txt/`. Accessed: 2018-03-11.

[49] Philippe H. M. Bräunig. *Atom Optical Tools for Antimatter Experiments*. PhD thesis, University of Heidelberg, 2014.

[50] Richard O. Duda and Peter E. Hart. Use of the hough transformation to detect lines and curves in pictures. *Commun. ACM*, 15(1):11–15, January 1972.

[51] Patrick Breheny. Lecture notes bayesian modeling in biostatistics spring 2013. `http://web.as.uky.edu/statistics/users/pbreheny/701/S13/notes/1-15.pdf`. Accessed: 2018-04-29.

[52] P. T. Boggs and J. E. Rogers. Orthogonal distance regression, 1990.

[53] H. Holmestad. Study of antiproton annihilation in silicon with a hybrid pixel detector using the timepix3 readout. In *2015 IEEE Nuclear Science Symposium and Medical Imaging Conference (NSS/MIC)*, pages 1–3, Oct 2015.

Publications

E. Comparison of planar and 3D silicon pixel sensors used for detection of low energy antiprotons

Title Comparison of planar and 3D silicon pixel sensors used for detection of low energy antiprotons

Abstract The principle aim of the AEgIS experiment at CERN is to measure the acceleration of antihydrogen due to Earth's gravitational field. This would be a test of the Weak Equivalence Principle, which states that all bodies fall with the same acceleration independently of their mass and composition. The effect of Earth's gravitational field on antimatter will be determined by measuring the deflection of the path of the anti- hydrogen from a straight line. The position of the antihydrogen will be found by detecting its annihilation on the surface of a silicon detector. The gravitational measurement in AEgIS will be performed with a gravity module, which includes the silicon detector, an emulsion detector and a scintillating fibre time-of-flight detector. As the experiment attempts to determine the gravitational acceleration with a precision of 1 %, a position resolution better than 10 μm is required. Here we present the results of a study of antiproton annihilations in a 3D silicon pixel sensor and compare the results with a previous study using a monolithic active pixel sensor. This work is part of a larger study on different silicon sensor technologies needed for the development of a silicon position detector for the AEgIS experiment. The 3D detector together with its readout electronics have been originally designed for the ATLAS detector at the LHC. The direct annihilation of low energy antiprotons (∼100 keV) takes place in the first few μm of the silicon sensor and we show that the charged products of the annihilation can be detected with the same sensor. The present study also aims to understand the signature of an antiproton annihilation event in segmented silicon detectors and compares it with a GEANT4 simulation model. These results will be used to determine the geometrical and process parameters to be adopted by the silicon annihilation detector to be installed in AEgIS.

Where IEEE Transactions on Nuclear Science

When December, 2014

Contribution Helga contributed with the Geant4 simulations for the 3D pixel detector by implementing a model of the 3D pixel detector in the full simulation of the AEgIS apparatus. The results are in figure 4, 13 and 14.

Main author Angela Gligorova

Co-authors AEgIS collaboration

Bibliography entry [33]

Location on-line
`https://ieeexplore.ieee.org/document/6971249/`

F. Study of antiproton annihilation in silicon with a hybrid pixel detector using the TimePix3 readout

Title Study of antiproton annihilation in silicon with a hybrid pixel detector using the TimePix3 readout

Abstract The main goal of the AEgIS experiments is to measure the gravitational force for anti-hydrogen, testing Ein- stein's weak equivalence principle, which states that all bodies falls with the same acceleration, independently from their mass and composition. The measurement will be done using an anti- hydrogen beam sent trough a classical moire deflectometer. To measure the deflection of the beam from a straight path a position sensitive silicon detector followed by an emulsion detector and a scintillating fiber time-of-flight detector will be used. We present here a study performed using a novel hybrid pixel detector, employing the Timepix3 readout chip to tag and spatially resolve antiproton annihilations in silicon. In autumn 2014 we performed a test-experiment on a secondary beam line to the AEgIS experiment, where a pulsed beam of anti-protons of energy 5.3 MeV was delivered from the Antiproton Decelerator of CERN accelerator complex. Taking advantage of the high spatial resolution, ToA capabilities and extended energy range of the Timepix3, this study investigates unique features of antiproton annihilation events in silicon. We are for the first time able to set clear criteria to characterize an antiproton annihilation using a silicon detector.

Where IEEE, San Diego, USA

When Oct 31th – Nov 7th, 2015

Contribution Helga contributed did the whole analysis and simulations, wrote the paper, presented it at the IEEE conference in San Diego and participated during data taking.

Main author Helga Holmestad

Co-authors AEgIS collaboration

Bibliography entry [53]

Location on-line
`https://ieeexplore.ieee.org/document/7581982/`

G. Antiproton tagging and vertex fitting in a Timepix3 detector

Title Antiproton tagging and vertex fitting in a Timepix3 detector

Abstract Studies of antimatter are important for understanding our universe at a fundamental level. There are still unsolved problems, such as the matter-antimatter asymmetry in the universe. The AEgIS experiment at CERN aims at measuring the gravitational fall of antihydrogen in order to determine the gravitational force on antimatter. The proposed method will make use of a position- sensitive detector to measure the annihilation point of antihydrogen. Such a detector must be able to tag the antiproton, measure its time of arrival and reconstruct its annihilation point with high precision in the vertical direction. This work explores a new method for tagging antiprotons and reconstructing their annihilation point. Antiprotons from the Antiproton Decelerator at CERN were used to obtain data on direct annihilations on the surface of a silicon pixel sensor with Timepix3 readout. These data were used to develop and verify a detector response model for annihilation of antiprotons in this detector. Using this model and the antiproton data it is shown that a tagging efficiency of 50 ± 10% and a vertical position resolution of 22± 0.5μ m can be obtained.

Where Journal of Instrumentation

When Submitted March 12th 2018 and accepted June 7th.

Contribution Helga did all the analysis and simulation work, wrote the whole article, and participated during data taking.

Main author Helga Holmestad

Co-authors AEgIS collaboration

Bibliography entry [47]

Location on-line

`http://iopscience.iop.org/article/10.1088/1748-0221/13/06/P06004`

Journal of Instrumentation

Antiproton tagging and vertex fitting in a Timepix3 detector

To cite this article: S. Aghion *et al* 2018 *JINST* **13** P06004

Published by IOP Publishing for Sissa Medialab

Received: *March 12, 2018*
Revised: *May 13, 2018*
Accepted: *May 19, 2018*
Published: *June 7, 2018*

Antiproton tagging and vertex fitting in a Timepix3 detector

The AEgIS collaboration

S. Aghion,[a,b] C. Amsler,[c] M. Antonello,[b,d] A. Belov,[t] G. Bonomi,[f,g] R.S. Brusa,[h,i] M. Caccia,[b,d] A. Camper,[j] R. Caravita,[j] F. Castelli,[b,k] G. Cerchiari,[l] D. Comparat,[m] G. Consolati,[n,b] A. Demetrio,[o] L. Di Noto,[p,q] M. Doser,[j] C. Evans,[a,b] M. Fanì,[p,q,j] R. Ferragut,[a,b] J. Fesel,[j] A. Fontana,[g] S. Gerber,[j] M. Giammarchi,[b] A. Gligorova,[c] F. Guatieri,[h,i] Ph. Hackstock,[c] S. Haider,[j] A. Hinterberger,[j] H. Holmestad,[r,1] A. Kellerbauer,[l] O. Khalidova,[j] D. Krasnický,[q] V. Lagomarsino,[p,q] P. Lansonneur,[s] P. Lebrun,[s] C. Malbrunot,[j,c] S. Mariazzi,[i] J. Marton,[c] V. Matveev,[t,e] S.R. Müller,[o] G. Nebbia,[u] P. Nedelec,[s] M. Oberthaler,[o] N. Pacifico,[v,j] D. Pagano,[f,g] L. Penasa,[h,i] V. Petracek,[w] F. Prelz,[b] M. Prevedelli,[x] B. Rienaecker,[j] J. Robert,[m] O.M. Røhne,[r] A. Rotondi,[g,y] H. Sandaker,[r] R. Santoro,[b,d] L. Smestad,[j,z] F. Sorrentino,[p,q] G. Testera,[q] I. C. Tietje,[j] E. Widmann,[c] P. Yzombard,[l] C. Zimmer,[j,l,aa] J. Zmeskal[c] and N. Zurlo[g,ab]

[a] *LNESS, Department of Physics, Politecnico di Milano, via Anzani 42, 22100 Como, Italy*
[b] *INFN Milano, via Celoria 16, 20133 Milano, Italy*
[c] *Stefan Meyer Institute for Subatomic Physics, Austrian Academy of Sciences, Boltzmanngasse 3, 1090 Vienna, Austria*
[d] *Department of Science, University of Insubria, Via Valleggio 11, 22100 Como, Italy*
[e] *Joint Institute for Nuclear Research, Dubna 141980, Russia*
[f] *Department of Mechanical and Industrial Engineering, University of Brescia, via Branze 38, 25123 Brescia, Italy*
[g] *INFN Pavia, via Bassi 6, 27100 Pavia, Italy*
[h] *Department of Physics, University of Trento, via Sommarive 14, 38123 Povo, Trento, Italy*
[i] *TIFPA/INFN Trento, via Sommarive 14, 38123 Povo, Trento, Italy*
[j] *Physics Department, CERN, 1211 Geneva 23, Switzerland*
[k] *Department of Physics, University of Milano, via Celoria 16, 20133 Milano, Italy*
[l] *Max Planck Institute for Nuclear Physics, Saupfercheckweg 1, 69117 Heidelberg, Germany*
[m] *Laboratoire Aimé Cotton, Université Paris-Sud, ENS Paris Saclay, CNRS, Université Paris-Saclay, 91405 Orsay Cedex, France*
[n] *Department of Aerospace Science and Technology, Politecnico di Milano, via La Masa 34, 20156 Milano, Italy*

---

[1] Corresponding author.

https://doi.org/10.1088/1748-0221/13/06/P06004

[o]Kirchhoff-Institute for Physics, Heidelberg University,
Im Neuenheimer Feld 227, 69120 Heidelberg, Germany
[p]Department of Physics, University of Genova, via Dodecaneso 33, 16146 Genova, Italy
[q]INFN Genova, via Dodecaneso 33, 16146 Genova, Italy
[r]Department of Physics, University of Oslo, Sem Sælandsvei 24, 0371 Oslo, Norway
[s]Institute of Nuclear Physics, CNRS/IN2p3, University of Lyon 1, 69622 Villeurbanne, France
[t]Institute for Nuclear Research of the Russian Academy of Science, Moscow 117312, Russia
[u]INFN Padova, via Marzolo 8, 35131 Padova, Italy
[v]Institute of Physics and Technology, University of Bergen, Allégaten 55, 5007 Bergen, Norway
[w]Czech Technical University, Prague, Brehová 7, 11519 Prague 1, Czech Republic
[x]University of Bologna, Viale Berti Pichat 6/2, 40126 Bologna, Italy
[y]Department of Physics, University of Pavia, via Bassi 6, 27100 Pavia, Italy
[z]The Research Council of Norway, P.O. Box 564, 1327 Lysaker, Norway
[aa]Department of Physics, Heidelberg University, Im Neuenheimer Feld 226, 69120 Heidelberg, Germany
[ab]Department of Civil, Environmental, Architectural Engineering and Mathematics, University of Brescia,
via Branze 43, 25123 Brescia, Italy

E-mail: helga.holmestad@cern.ch

2018 JINST 13 P06004

Abstract: Studies of antimatter are important for understanding our universe at a fundamental level. There are still unsolved problems, such as the matter-antimatter asymmetry in the universe. The AEgIS experiment at CERN aims at measuring the gravitational fall of antihydrogen in order to determine the gravitational force on antimatter. The proposed method will make use of a position-sensitive detector to measure the annihilation point of antihydrogen. Such a detector must be able to tag the antiproton, measure its time of arrival and reconstruct its annihilation point with high precision in the vertical direction.

This work explores a new method for tagging antiprotons and reconstructing their annihilation point. Antiprotons from the Antiproton Decelerator at CERN were used to obtain data on direct annihilations on the surface of a silicon pixel sensor with Timepix3 readout. These data were used to develop and verify a detector response model for annihilation of antiprotons in this detector. Using this model and the antiproton data it is shown that a tagging efficiency of 50 ± 10% and a vertical position resolution of 22 ± 0.5 μm can be obtained.

Keywords: Detector modelling and simulations I (interaction of radiation with matter, interaction of photons with matter, interaction of hadrons with matter, etc); Hybrid detectors; Particle identification methods; Simulation methods and programs

Contents

1 Introduction

The main goal of the AEgIS experiment [1, 2] is to measure the gravitational force on antihydrogen to test the weak equivalence principle for antimatter. The method proposed is to accelerate a cold, pulsed beam of antihydrogen in an inhomogenous electric field (Stark acceleration). The beam is then sent through a classical moiré deflectometer [3, 4], as seen in figure 1. The antiatoms passing through the gratings annihilate on a position-sensitive detector, forming a fringe pattern. The gravitational acceleration can be observed by measuring the downward or upward shift of this pattern compared to a path undeflected in the vertical direction. The position-sensitive detector must be able to tag antihydrogen atoms, reconstruct their annihilation point, and measure their time of flight through the moiré deflectometer. Assuming a velocity of 500 m/s for the antihydrogen and a flight path of 1.0 m, a vertical fall of $\approx 20\,\mu$m is expected [5].

Antiproton annihilations as studied here can also be used for studying antihydrogen annihilations, as the positron annihilates independently on an atomic electron, resulting in two 511 keV photons, to which a silicon detector is not sensitive. Previous studies have been able to describe and identify signatures of antiproton annihilations in detectors, and to make a comparison between data and simulations [6, 7].

This study is the first in which quantitative results are found for the tagging efficiency and the position resolution of annihilations in a silicon pixel detector equipped with the Timepix3 [8] readout. The results provide the background for evaluating the usability of such a detector in AEgIS and other antimatter experiments.

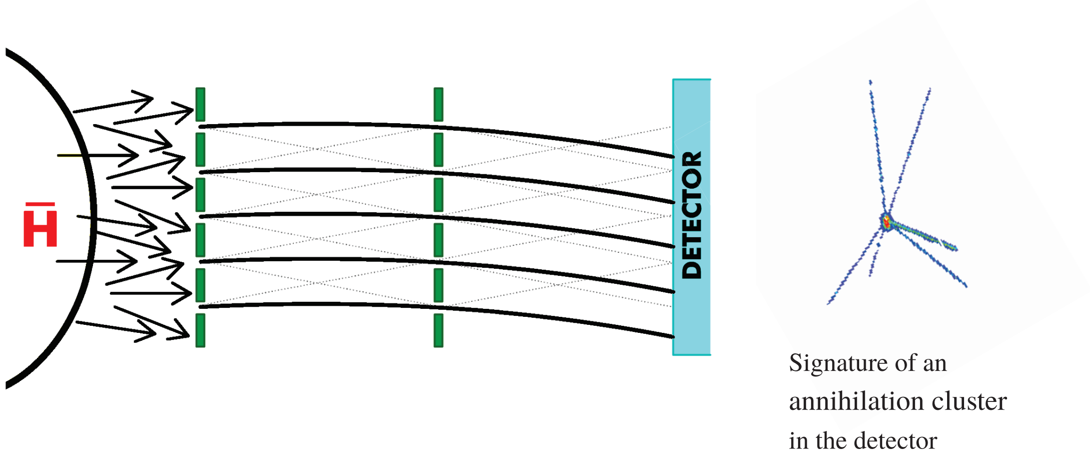

Figure 1. Illustration of the trajectories of antihydrogen passing through a classical moiré deflectometer. The antihydrogen atoms annihilate directly in the detector, and star-shaped annihilation clusters are detected. The paths of antihydrogen through the deflectometer are deflected by the gravitational field.

1.1 The GRACE beamline

The experimental setup is situated on the GRACE beamline [9] at the Antiproton Decelerator (AD) at CERN, where approximately 3×10^7 antiprotons with a kinetic energy of 5.3 MeV are delivered from the AD every ≈ 100 seconds [10]. Figures 2 and 3 show an illustration and a photo of the setup, while figure 4 shows the Timepix3 detector mounted in GRACE.

The GRACE beamline is designed to provide antiprotons with kinetic energies below 15 keV, while minimizing the background produced by antiprotons annihilating without reaching the detector. The beamline consists of a vacuum chamber with an extraction line inclined by 40° with respect to the incident beam. A 25 μm thick circular titanium window with a diameter of 40.0 mm allows the antiprotons to enter into GRACE. Einzel lenses for focusing and a pair of bending electrodes guide the low-energy antiprotons towards the detector. To further reduce the energy of the beam, an aluminum degrader of variable thickness is placed in the air gap between the AD and the GRACE beamline.

The degrader thickness and the electrode voltages were manually tuned to achieve the maximum number of star-shaped clusters on the detector. The optimum was found to be with a 33 μm thick aluminum degrader, a bending voltage between 3000 and 4000 V, and a focusing voltage between 3000 and 4000 V on each of the einzel lenses. This configuration was used for the present study.

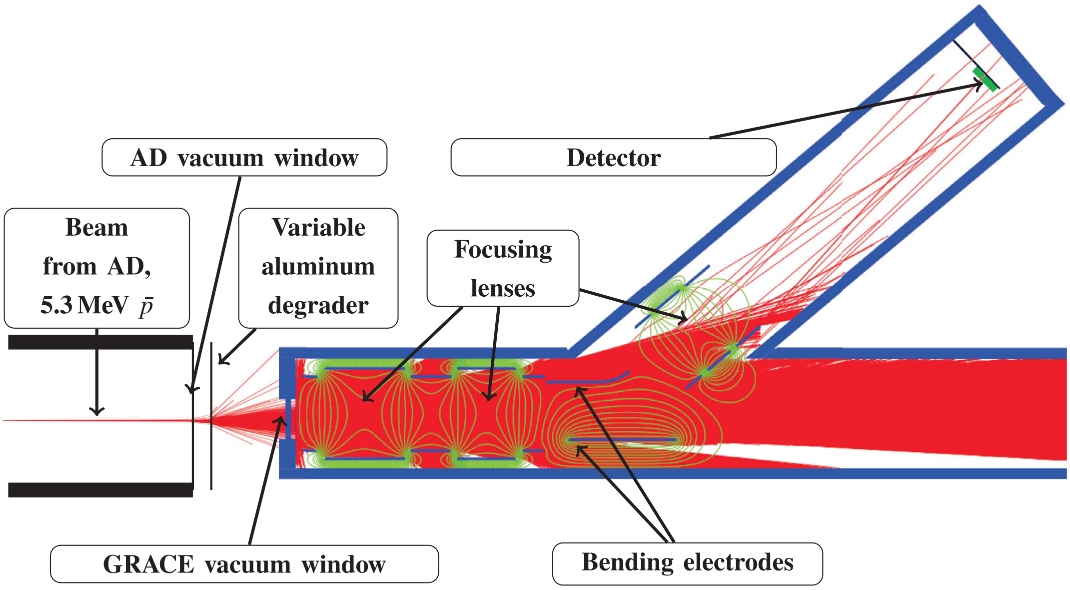

Figure 2. Sketch of the GRACE beamline. The antiproton beam of 5.3 MeV arrives from the AD, loses energy and is scattered by the vacuum windows, the variable degrader, and the air gap between the AD and GRACE. The bending electrodes are used to select antiprotons with energies below 15 keV and direct them towards the detector. The figure is not to scale.

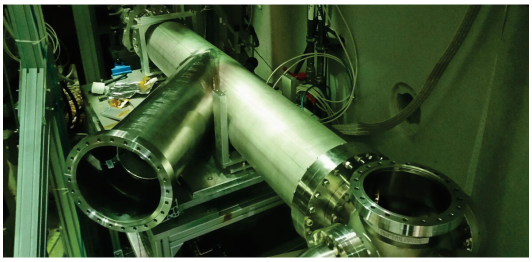

Figure 3. The GRACE beamline at the end of one of the extraction points of the AD before the detector chamber is mounted. The detector chamber is installed on the open flange on the left.

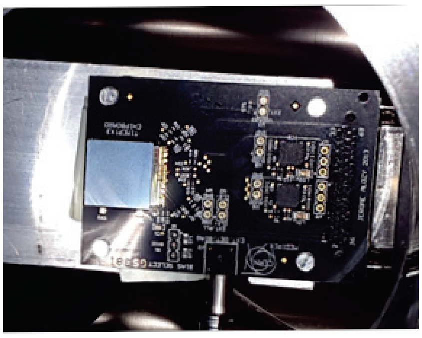

Figure 4. The Timepix3 detector mounted at the end of the GRACE beamline, with the sensor in the center left of the PCB.

1.2 Characteristics of antiproton annihilations in matter

An antiproton annihilation with an atomic nucleon creates on average in total 5 pions (charged and neutral) per annihilation [11]. Some of these pions are likely to penetrate the affected nucleus, and nuclear fragments can break off. The multiplicity and energy distribution of these annihilation products is not fully known. Since simulations are based upon theoretical models and sparse data, they are not able to completely reproduce experimental results. Studies of antiproton annihilations in copper, silver and gold [12] show that the simulation software FLUKA performs better than other available software such as Geant4, and FLUKA was therefore used for this study.

The annihilation products acquire kinetic energy from the mass-to-energy conversion of the annihilation, and travel away from the annihilation point. This gives rise to a star-shaped cluster in the detector, as seen in figure 1. Figure 5 shows the multiplicity of the charged pions and fragments when antiprotons annihilate in aluminum as simulated with FLUKA [13].

The AD delivers around 3×10^7 antiprotons per bunch, and around 20–30 of these antiprotons reach the detector. In addition to the antiprotons, fragments and pions from annihilations occurring in the vacuum window of GRACE, and on the walls and electrodes inside GRACE can also reach the detector. These particles create secondary clusters which contaminate the data. Secondary clusters are defined as clusters caused by nuclear fragments or pions originating from annihilations taking place elsewhere than in the detector itself. Annihilation clusters are defined as clusters caused by antiprotons annihilating directly on the surface of the detector. An annihilation cluster can be recognized as a region with high-energy depositions, possibly with tracks originating from its center. These tracks, from here on called prongs, are caused by pions or nuclear fragments traveling in the plane of the detector. One clear example of an annihilation cluster is shown in figure 1.

To be able to tag antiprotons, an algorithm to distinguish between annihilation clusters and secondary clusters was developed and will be described in section 5. A perfect distinction is not possible, therefore there will always be a trade-off between the tagging efficiency and the false tagging rate. The false tagging rate is defined as the probability of mistagging a secondary cluster as an annihilation cluster.

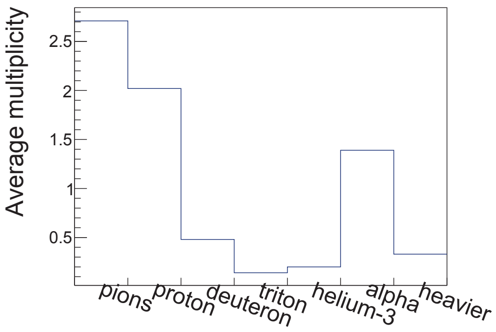

Figure 5. Multiplicity of charged nuclear fragments and pions from antiproton annihilations in aluminum, as simulated with FLUKA [13].

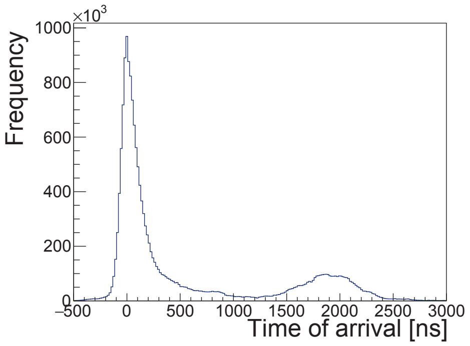

Figure 6. The Time of Arrival (ToA) for all data in the main sample. The antiprotons are found in the second peak.

1.3 The detector

The detector consists of a 675 μm thick silicon sensor with a 0.5 μm thin aluminum layer on top, bump-bonded to an ASIC with the Timepix3 [8] readout. The size of the detector is $14 \times 14\,\text{mm}^2$, with 256×256 pixels and a pixel pitch of 55 μm. Each pixel is self-triggering and able to simultaneously measure both Time of Arrival (ToA) and Time over Threshold (ToT). The time resolution is 1–2 ns. The conversion between ToT and deposited energy is found by injecting test pulses into the readout electronics and assuming 3.6 eV as the average energy required to create an electron/hole pair. The depletion voltage was measured to be around 200 V [14], and the device was operated at this bias voltage during data taking. A photo of the Timepix3 detector is shown in figure 4. The dead time of the pixels is given as the ToT pulse time +475 ns [8]. Experimentally it was observed that the majority of the pixels recover after around 550 ns.

When hit by an antiproton or a heavy nuclear fragment, the detector suffers from the volcano effect [15]. This is a disturbance in the readout when a pixel experiences a large charge readout. Instead of the actual energy deposition, a lower random energy deposition is recorded. Tests with high-energy ions impacting a silicon detector with the Timepix3 readout [16] showed that the transformation from registered ToT to deposited energy breaks down from around 450 keV deposited energy per pixel. The per-pixel highest deposited energy in each cluster seems to follow a Gaussian-like distribution with mean approximately 500 keV and standard deviation approximately 50 keV.

The settings applied to GRACE ensure that all antiprotons to be studied have a kinetic energy below 15 keV. The penetration depth in aluminum at this energy is 0.1 μm [17], therefore the annihilations occur in the top of the 0.5 μm thick aluminum layer on the surface of the sensor.

2 Analysis of experimental data

Two data samples were collected during the test beams in 2015 and 2016, and consisted of one main data sample and one reference data sample. The main sample was taken using the optimal GRACE settings described in section 1.1, and consists of 560 bunches from the AD, each containing a mixture of annihilation clusters and secondary clusters. In this data set 44 bunches are reserved as training data to develop the algorithms for clustering and characterization. The reference data sample was taken with the detector rotated such that its back was facing the beam. In this configuration no antiprotons annihilate directly on the detector. The reference data sample therefore consists of 1561 bunches only containing secondary clusters.

2.1 Time selection

The pions and nuclear fragments from an annihilation have much higher kinetic energy than the antiprotons which are bent towards the detector. According to FLUKA their average kinetic energy is 90 MeV, while the antiprotons bent towards the detector always have a kinetic energy below 15 keV. Therefore a shower of pions and nuclear fragments from annihilations upstream of the detector will hit the detector before the antiprotons. Figure 6 shows the ToA distribution in the main sample, in which two clear peaks can be identified. The first peak is caused by annihilations in the entrance window to GRACE, and consist of pions and nuclear fragments only. Within each bunch the maximum of the first peak is used as an estimate for the time the beam enters GRACE. The antiprotons arrive in the second peak, together with pions and nuclear fragments from annihilations taking place closer to the detector. Since antiprotons are primarily found within the second peak, only pixels that are time delayed by more than 1000 ns from when the beam enters GRACE were selected for analysis.

2.2 Removing the halo signal

Figure 7a shows all the raw hits from one bunch in the main data sample after time selection, where it can be seen that areas with high-energy depositions are surrounded by a halo of lower-energy depositions [18]. Figure 7b shows the same frame after a cut at 5 keV measured energy deposition has been applied to removed these halo hits. The measured energy deposition in the pixels in the halos is usually between 2 and 4 keV. The halo hits are not caused by actual charge collected in the pixel, but are the result of a detector artifact as described in ref. [19]. Therefore a threshold was set to remove all low-energy pixels, as this makes the clusters easier to analyze by reducing the chance of two distinct clusters to overlap.

In order to find a suitable threshold, the behavior of a Minimum Ionizing Particle (MIP) was considered, as any real particle would result in an energy deposition at least equivalent to a MIP. The search distance of the clustering algorithm presented in the next section is large enough to allow two missing pixels next to each other in a cluster. Geometrical considerations show that, for a pixel pitch p, a particle traveling less than $\frac{p}{\sqrt{2}}$ in one pixel it is bound to travel longer in at least one of the neighboring pixels. For a pixel pitch of 55 μm this distance is $\frac{p}{\sqrt{2}} = 38.9\,\mu$m. Figure 8 shows the simulated energy deposition from a MIP traversing 38.9 μm of silicon, compared to the distribution of the energy deposited in the pixels in the main data sample. As seen from this figure, the deposited energies from a MIP never goes below 5 keV. Setting the threshold at 5 keV will therefore remove the vast majority of the halo hits, while it will never cut off a track caused by a real particle.

2.3 Clustering and cluster characterization

Pixels that are connected to one of their neighbors by less than 20 ns in time and less than 225 μm in distance are defined as a cluster. These parameters were tuned by inspecting the training data set which was excluded from the analysis. The combination of clustering in both time and space has the advantage that clusters overlapping in space can be distinguished if they don't overlap in time. An algorithm to identify the prongs and the center of a cluster was developed and the procedure is described below. Also here reasonable values of the parameters were found by inspecting the training data set that was excluded from the analysis. The flow of the algorithm is shown in figure 9. The algorithm described here makes it possible to identify the amount of energy deposited in the estimated center of the clusters, and to determine the number of prongs in a cluster.

First, a straight line is fitted to the pixels in the cluster, taking the spatial center of the pixel as the point used for fitting. A low χ^2 value on this fit identifies clusters that are just a single track, and therefore any cluster which has a χ^2 value normalized to its degrees of freedom below 1.0 is assumed to have zero prongs. The second step is to estimate the spatial coordinates of the center of the cluster. For each pixel in the cluster the total deposited energy E_{center} in a circular region with a radius of 275 μm from the center of that pixel is calculated. The mass center of the region with the largest E_{center} is used as an estimate for the center of the cluster (x_0,y_0). Pixels within the 275 μm radius around the point (x_0,y_0) are then discarded to make it easier to recognize the prongs in the cluster.

The next step is to use Hough transformations [20] to identify the straight lines of the prongs extending from the center of the clusters with (x_0,y_0) as a fixed point along the path. The number of hit pixels within each circular segment with opening angle 3.6° radiating from the center of the cluster are counted. The segment with the maximum number of pixels gives the direction of the most evident prong. The pixels belonging to a prong are defined as all pixels within ±20° of the prong direction. The pixels belonging to the identified prong are then removed, and the subsequent most evident prong is identified in the same manner. This procedure is repeated until no more prongs consisting of at least 4 pixels are found.

2018 JINST 13 P06004

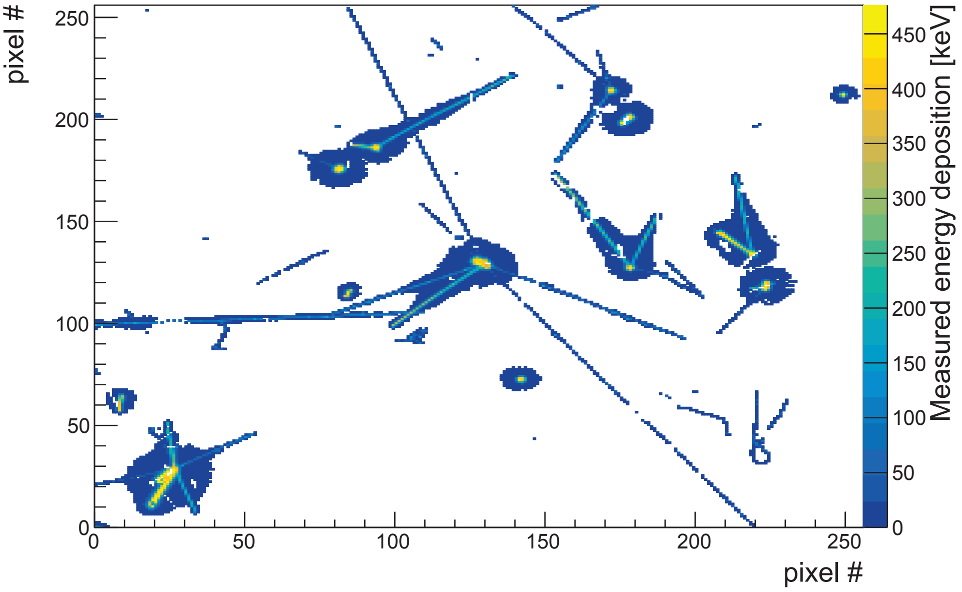

(a) Before the halo hits has been removed.

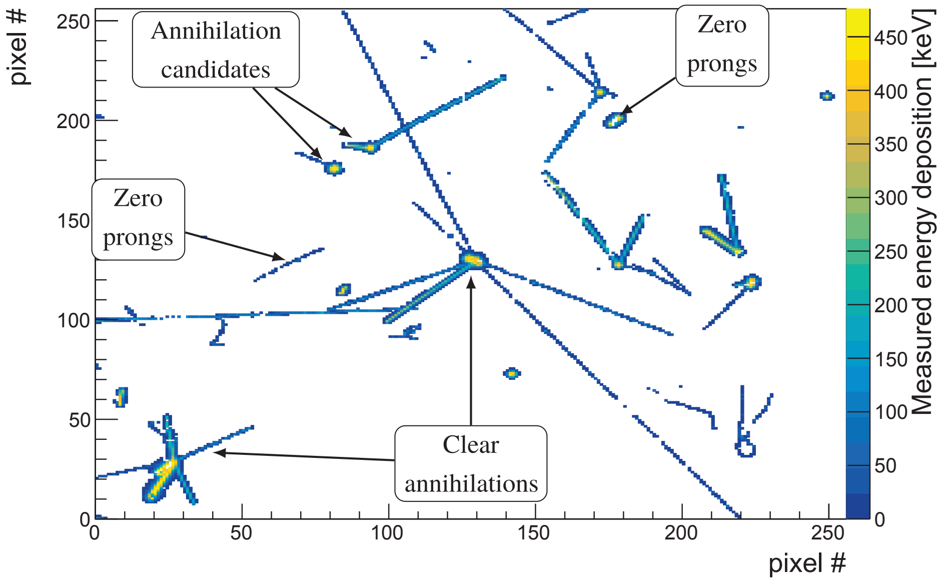

(b) After the halo hits has been removed.

Figure 7. These two frames show all hits from one bunch that are time-delayed by more than 1000 ns from the estimated arrival time into GRACE. Figure a) shows the frame before the halo hits are removed, while figure b) shows the frame after the halo hits are removed.

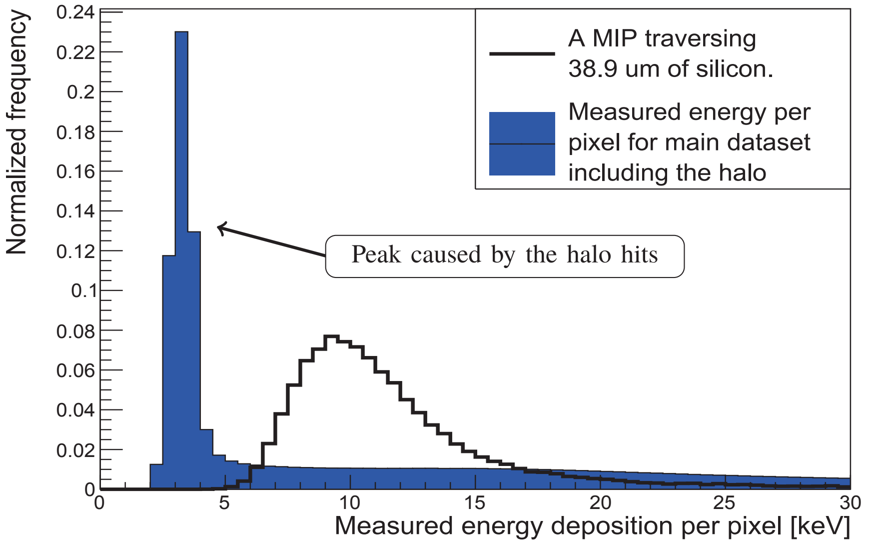

Figure 8. Energy deposition of a MIP (pion of 200 MeV) when traversing 38.9 μm of silicon material, simulated by Geant4, compared to the measured energy depositions in all the pixels in the main data sample.

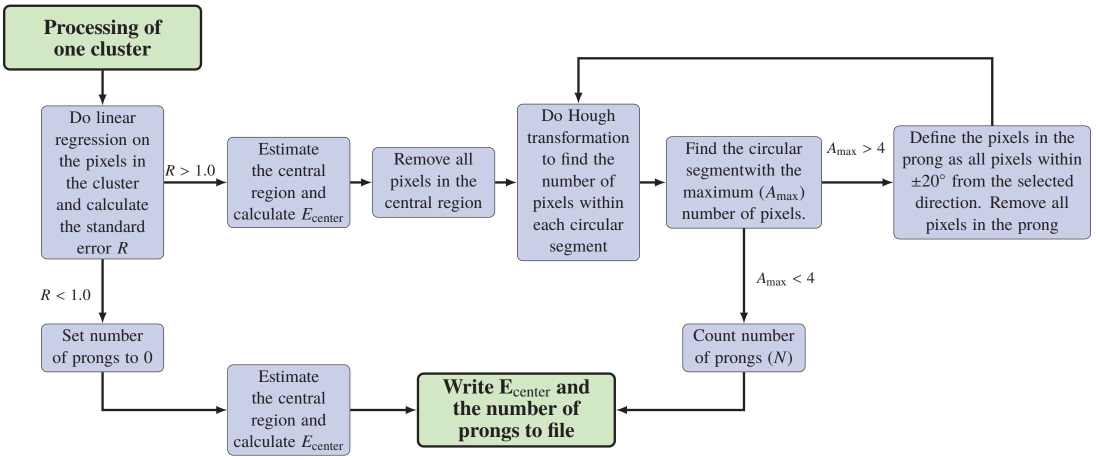

Figure 9. Flow chart for the algorithm developed to characterize the clusters.

3 Detector response model

In order to study the annihilation clusters, a full detector response model based on FLUKA [13] was developed. FLUKA provides the energy deposited in chosen voxels in the detector; for this study the voxels were set to $5.5 \times 5.5 \times 225\ \mu\text{m}^3$ (x × y × depth). Voxels much smaller than the pixel size were chosen in order to take into account the position of the energy deposition within the pixel. This section describes how these raw energy depositions are processed to simulate the detector response. Using the detector response model described here a sample of 10 000 simulated annihilation clusters was produced.

2018 JINST 13 P06004

3.1 Modeling charge sharing between pixels

Charges liberated by the energy depositions will diffuse as they drift towards the collecting electrodes, causing charge sharing between pixels. Assuming a Gaussian shape of the charge cloud, its size in terms of the standard deviation at the readout electrodes is

$$\sigma = \sqrt{2Dt_d}, \tag{3.1}$$

where the amount of diffusion depends on the collection time t_d, and the diffusion constant D [21]. A simple model for the collection time is given by

$$t_d = \frac{w^2}{2\mu V_d} \ln\left(1.0 - \frac{z}{w} \cdot \frac{2V_d}{V + V_d}\right), \tag{3.2}$$

where z is the depth of the energy deposition, w the thickness of the detector, V_d the depletion voltage, μ the carrier mobility and V the applied voltage [22, 23].

If the amount of space charge is large enough to disturb the field in the detector the collection time increases. This phenomenon is called the plasma effect [24], and its impact increases with increasing energy deposition. The simple model in equation (3.2) does not consider the plasma effect, however it is included in the device simulation software TCAD [25]. Therefore this software was used to find the collection time for different energy depositions. The simulation was done for three different depths, corresponding to the three different depths of the center of the voxels. The results from the TCAD simulations are found in table 1. For comparison the collection time from the simple model in equation (3.2) is also indicated. There is good agreement between the collection time given by the two models for energy depositions of 1 keV and 10 keV, giving evidence that the plasma effect is not present here. For larger energy depositions, the collection time clearly differs, as expected due to the plasma effect.

The diffusion constant for holes in silicon at room temperature is 12 $\mathrm{cm^2/s}$ [26], and this value was used to calculate the charge spread in equation (3.1) when the plasma effect is not present. When the plasma effect is present, the effective diffusion coefficient is found to be 18.0 $\mathrm{cm^2/s}$ in silicon at room temperature [24]; this value was therefore used for energy depositions above 10 keV.

The standard deviation σ for the charges liberated in a voxel was found by collecting the energy depositions in the neighborhood of that voxel, and table 1 was then used as a lookup table. The neighborhood is defined by all voxels with their center within a radius of 25 μm, as this is a typical size of the charge cloud. Since the energy deposited can take on continuous values, linear interpolation was used between the values in table 1.

3.2 Modeling front-end electronics effects

In the simulation two front-end electronic effects were taken into account; the volcano effect and suppressed pixels due to the dead time of the pixels. The volcano effect, as described in section 1.3, causes the pixels receiving high-energy depositions to saturate around 500 keV. This effect was taken into account in the simulation by setting all pixels with an energy deposition above 500 keV to a random value following a Gaussian distribution with mean 500 keV and standard deviation 50 keV.

The majority of the pixels in the main data set had a dead time of approximately 550 ns after being hit. The dead time was taken into account by, for each simulated cluster, choosing one

Table 1. Lookup table to find the amount of charge sharing from the energy deposited around the charge that is transported.

Energy deposited	Depth [μm]	Collection time t_c from eq. (3.2) [ns]	Collection time t_c from TCAD [ns]	Calculated σ from TCAD [μm]
1 keV	562.5	45	30	8.5
	337.5	17	14	5.8
	112.5	5	6	3.9
10 keV	562.5	45	36	9.3
	337.5	17	17	6.4
	112.5	5	7	4.1
100 keV	562.5	45	79	16.8
	337.5	17	26	9.6
	112.5	5	16	7.5
1 MeV	562.5	45	349	34.5
	337.5	17	98	18.8
	112.5	5	48	13.0
10 MeV	562.5	45	1780	80.0
	337.5	17	494	42.2
	112.5	5	243	29.6
50 MeV	562.5	45	4584	128.4
	337.5	17	1534	74.3
	112.5	5	760	52.3

random bunch from the experimental main data sample. The pixels in that bunch that are time-delayed between 1350 ns and 1900 ns were set as suppressed in the simulated cluster. This time interval was chosen because the center of the second peak in the ToA distribution in figure 6 is at 1900 ns, indicating the most likely time delay for an antiproton. An antiproton arriving at the most likely time will see all pixels triggered in the chosen time interval as suppressed.

4 Test of the detector response model

The detector response model was verified by comparing the distributions of cluster observables in data and simulation. The observables studied are the cluster size given, the number of prongs, the energy deposited in the center of the cluster and the energy deposited in the whole cluster. The cluster size is defined as the number of pixels making up the clusters after the cut at 5 keV has been applied. The main data sample contains a mixture of secondary clusters and annihilation clusters, while the reference sample contains only secondary clusters. Therefore the main data sample was compared to a weighted combination of the reference data sample and the sample of simulated annihilation clusters. This combined sample of reference data and simulated annihilation clusters was normalized to the total number of clusters in the main data sample.

The fraction of the reference data sample in the combined sample, from here on referred to as r, is a free parameter that was optimized to minimize the χ^2 value of the difference between the histogram bins. The minimum value for χ^2 was found for $r = 0.83$, and figure 10 shows the comparison between the main data sample and the combined sample using this value for r. For observables relating to the shape of the cluster the agreement between data and simulation is good. There is some discrepancy in the deposited energy, especially in the center of the cluster, as seen in figure 10d. This discrepancy may be caused by inaccuracy in how FLUKA models antiproton annihilations, or in how the volcano effect is modeled, as described in section 3.2. The optimization can also be done on each histogram individually, and the values for r are then 0.81, 0.85, 0.87 and 0.83 for the cluster size, number of prongs, center charge, and total charge, respectively.

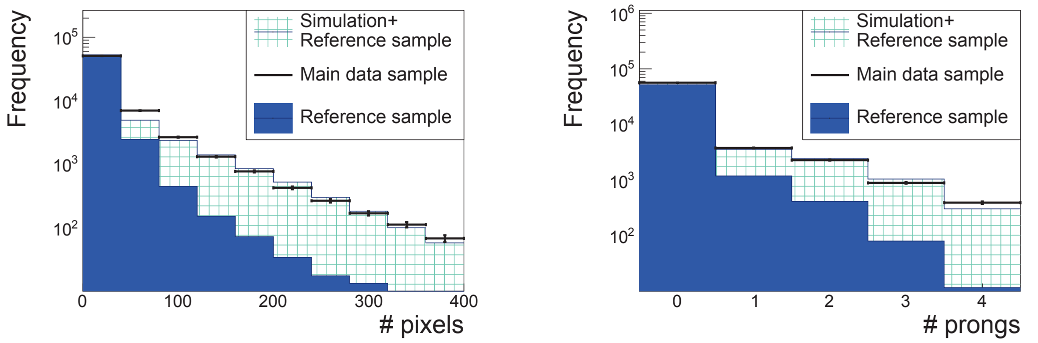

(a) Cluster size in terms of pixels.

(b) Number of prongs detected in the clusters.

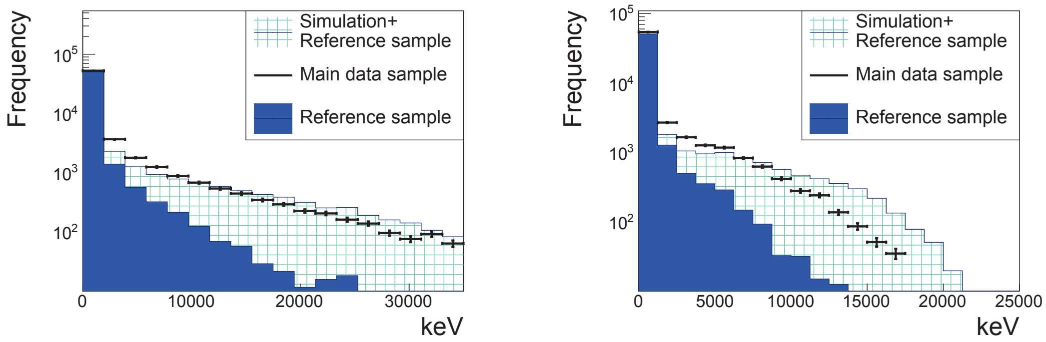

(c) Measured energy deposition in the clusters.

(d) Measured energy deposition in the center of the clusters.

Figure 10. Histograms comparing the cluster observables in data and simulations. Observables relating to the shape of the clusters seem to be modeled better. The fraction of secondary clusters is estimated to be $r = 0.83$.

5 Estimate of the tagging efficiency

This section shows how cuts on cluster size and number of prongs are set in order to tag the antiprotons. These two cluster observables were chosen because observables relating to the shape of the clusters are the most accurately modeled ones. The false tagging rate, from here on referred to as p_f, was estimated by the fraction of clusters passing the cuts in the reference data sample. The tagging efficiency, from here on referred to as p_t, was found by applying the cuts on the sample of simulated clusters.

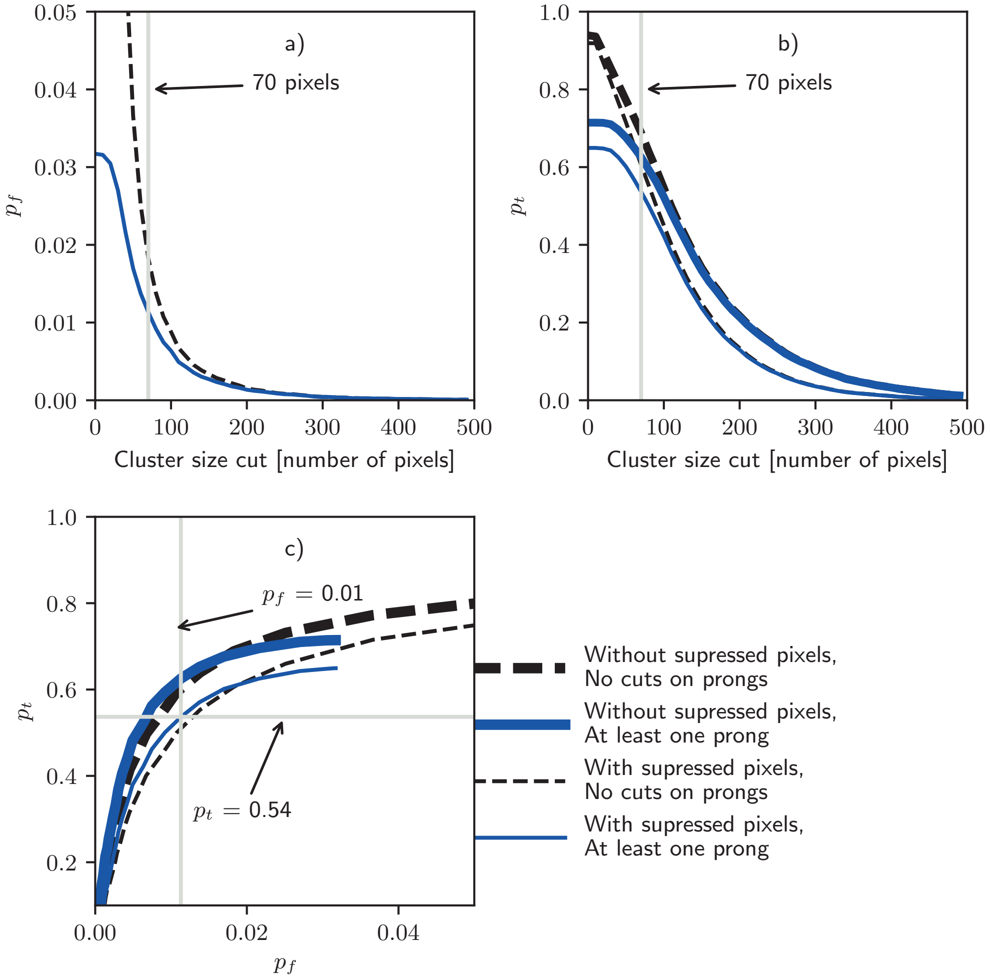

Figure 11. Plots showing the relationship between tagging efficiency (p_t), false tagging rate (p_f) and the cuts. The working cut of 70 pixels, and the resulting efficiency and false tagging rate obtained with this cut and at least one prong are also indicated. **a)** The false tagging rate as a function of the cuts. **b)** The tagging efficiency as a function of the cuts. **c)** The tagging efficiency as a function of the false tagging rate.

Figure 11 shows p_t and p_f as a function of the cuts. The results are shown with and without considering the suppressed pixels in the simulation, as further experiments might be able to reduce the flux and hence avoid suppressed pixels due to dead time. The estimate of p_f always includes suppressed pixels as it is estimated from experimental data. A cut of at least 70 pixels and at least one prong in the cluster gives a tagging efficiency of $p_t = 52\%$. The corresponding value of p_f is then 1.1%, making this cut a good compromise between high tagging efficiency and low false tagging rate. The comparison of the cluster observables after such a cuts is shown in figure 12, and the optimal value for r is then 0.16.

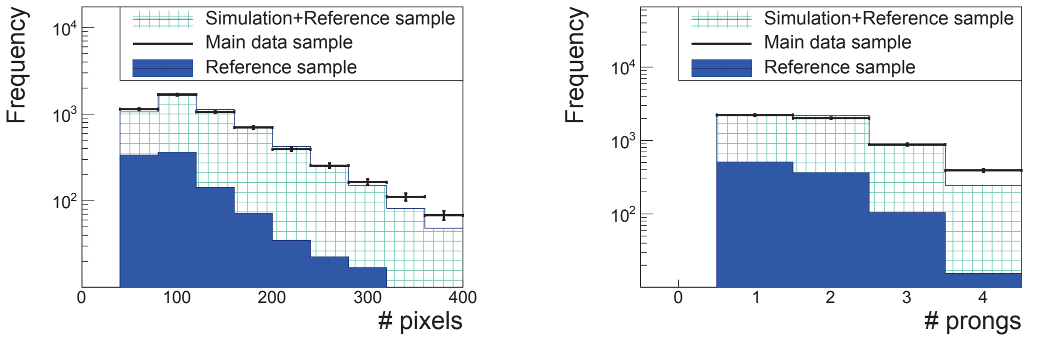

(a) Cluster size in terms of pixels after selection. **(b)** Number of prongs detected in clusters after selection.

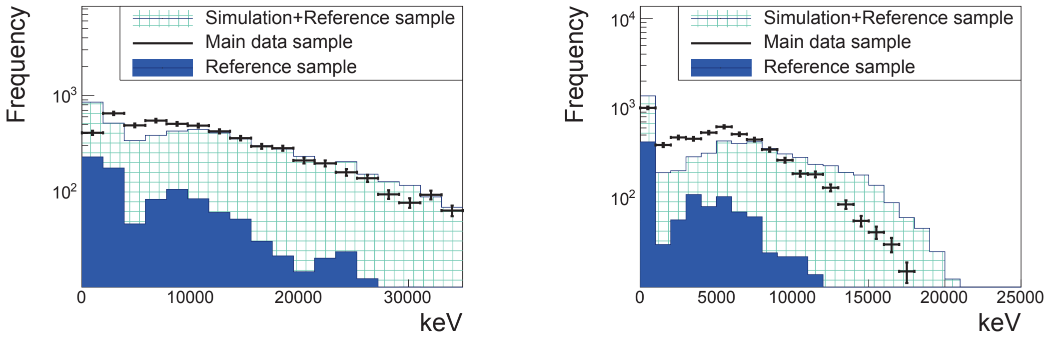

(c) Measured energy deposition in the clusters after selection. **(d)** Measured energy in center of the clusters after selection.

Figure 12. Comparison between data and simulation for clusters passing the cut of at least 70 pixels and at least one prong. As in figure 10 observables related to the shape of the clusters are better modeled. The fraction of secondary clusters is estimated to be 0.18.

5.1 The uncertainty of the tagging efficiency and the false tagging rate

The statistical uncertainty on the tagging efficiency and the false tagging rate depends only on the sample size n and is given by

$$\sigma = \sqrt{\frac{p(1-p)}{n}}, \tag{5.1}$$

where p is the estimated rate. This gives a statistical uncertainty of ±0.5% and ±0.2% for the tagging efficiency and the false tagging rate respectively. However, as seen in figure 10 the simulation does not completely reproduce the data, leaving some discrepancy between data and simulation. This is caused by systematic errors, and two sources of systematic errors were identified. The first being that the reference sample might not completely represent the secondary clusters in the main data sample. The secondary clusters in the main data sample can be caused by annihilations happening anywhere, although solid angle considerations makes it more likely for them to happen close to the detector. In the reference sample the clusters are only caused by annihilations happening downstream of the detector. Therefore secondary clusters in the main sample might be caused by

2018 JINST 13 P06004

pions and nuclear fragments impinging more orthogonal to the detector compared to the reference sample. This could cause slightly larger clusters in the reference sample, and therefore the false tagging rate might be overestimated.

The second systematic error concerns how well the simulated clusters reproduce the annihilation clusters in the main sample. To estimate this effect the tagging efficiency was also calculated by a mainly data-driven method. In the main data sample the number of correctly tagged annihilation clusters is given by

$$A_t = N_t - N f p_f\,, \tag{5.2}$$

where N_t is the number of tagged clusters, N is the total number of clusters, f is the fraction of secondary clusters in the sample, and p_f is again the false tagging rate. The total number of annihilation clusters is

$$A = N - fN. \tag{5.3}$$

The tagging efficiency is estimated by the number of correctly tagged annihilation clusters divided by the total number of annihilation clusters, yielding the following expression for the tagging efficiency:

$$t = \frac{A_t}{A}\,. \tag{5.4}$$

In the main data sample $N = 63890$, and with the applied cuts of at least 70 pixels and at least one prong $N_t = 5771$. The value of f is unknown, but in section 4 the fraction of secondary clusters was estimated to be in the range of 0.81–0.87. By equation (5.4) this corresponds to a tagging efficiency between 38% and 56%.

This method of calculating the tagging efficiency includes the false tagging rate that might be overestimated. However, the effect is not severe. Setting the tagging false rate to half of its estimated value would shift the tagging efficiency to lie between 40% and 60%.

In conclusion the systematic effects points to the tagging efficiency and the tagging false rate not being known to high precision, but supports that the tagging efficiency is in the range of 50 ± 10%, while the tagging false rate is below 1.1%.

6 Reconstruction of the annihilation point

This section uses the sample of simulated annihilation clusters to evaluate two methods for reconstructing the annihilation point: the mass center method and the vertex fitting method. Experiments for measuring the gravitational fall are expected to have low flux and therefore the pixels will in general have time to recover between being hit by different particles. For this reason the modeling of the suppressed pixels was excluded from this simulation. It was also assumed that the annihilation occurs in the central $5{\times}5\,\text{mm}^2$ of the detector such that prongs are not cut off by the edges of the detector. The relevant measurement for AEgIS is the vertical shift of the fringe pattern created by antihydrogen passing through the moiré deflectometer. Therefore the position resolution is calculated on the vertical direction y. The exact annihilation position is known from the simulation, and the residual is defined as the distance between the estimated annihilation point and the true annihilation point in the vertical direction. The metric chosen for position resolution is the symmetrical 68% confidence interval around 0 for the residuals, corresponding to $1.0\,\sigma$ for a Gaussian distribution. This method of calculating the position resolution suppresses the effect of outliers.

6.1 Mass center method

The mass center method estimates the annihilation point by the weighted relative position of the energy depositions in the central region. The definition of the central region is found in section 2.3. Figures 13a and 13b show the result using the mass center method, and the position resolution is estimated to be 93 μm. This method can be applied to all clusters, as it does not require the presence of prongs.

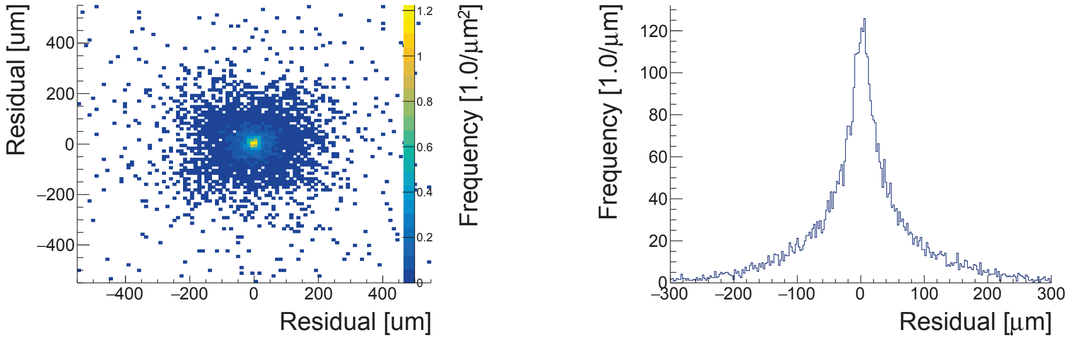

(a) Reconstructed annihilation point for antiprotons using the mass center method.

(b) Vertical distance between the fitted value and the true annihilation point using the mass center method. Estimated position resolution by 68% center is 93 μm.

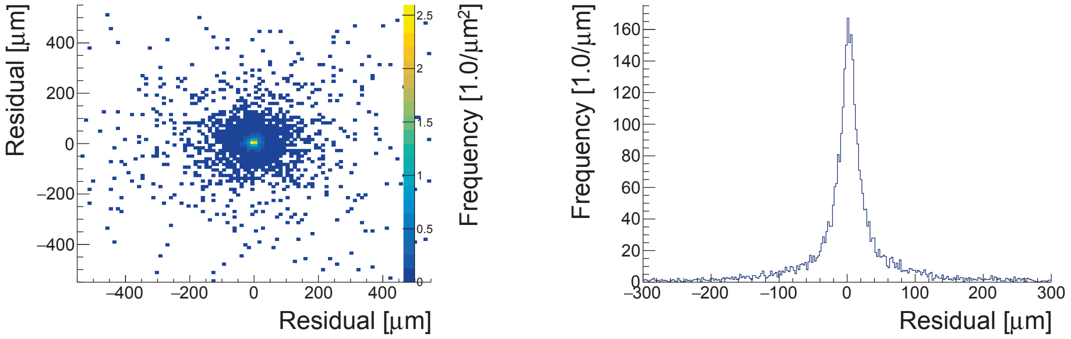

(c) Reconstructed annihilation point for antiprotons using the vertex fitting method.

(d) Vertical distance between the fitted value and the true annihilation point using the vertex fitting method. Estimated position resolution by 68% center is 48 μm.

Figure 13. Position resolution using the mass center method and the vertex fitting method.

6.2 Vertex fitting method

The vertex fitting method fits straight lines to the prongs, and the annihilation point is taken as the intersection between two of these lines. The lines were fitted by the orthogonal-least-squares method. The vertex fitting method requires at least two prongs, and 45% of the clusters have two or more prongs.

2018 JINST 13 P06004

Figure 14 shows how the residuals of the vertex fitting method correlate with the average number of pixels in the two prongs, the average length of the prongs, the crossing angle α between the two prongs, and the discrepancy of the estimates yielded by the two methods. According to figures 14a and 14b, the residuals are independent of the length of the prongs and the number of pixels in the prongs. That these two factors did not contribute to a better fit is probably because the same two factors also increases the probability that the prong undergoes scattering. The correlation between the residuals and the crossing angle shown in figure 14c shows that a crossing angle approaching parallel correlates with a bad fit, however the correlation is very weak and almost not visible in the scatter plot. Figure 14d shows the correlation between the discrepancy of the estimates from the two reconstruction methods and the residuals, and a strong correlation is evident for large residuals. This figure indicates that if the two methods disagree, the vertex fitting method is likely to give a bad estimate.

The following procedure was applied if there were more than two prongs yielding more than one candidate for the annihilation point. If two or more of the candidates are within a distance of ±55 μm to each other the average of this cluster of candidates is taken as the estimate. If all candidates are separated by more than 55 μm, the one with its crossing angle closest to 90° is chosen since a crossing angle close to 90° correlates with a good fit. This method proved to be more robust than reconstructing to a common vertex since, in cases where there are more than two prongs, it is likely to exclude prongs that are not contributing to a good estimate. The result of the vertex fitting method is shown in figure 13c and 13d, and the vertical position resolution was improved from 93 μm to 48 μm compared to the mass center method.

In some situations it might be beneficial to select a smaller sub-sample of clusters that are known to yield better reconstructed values. The disagreement between the two methods indicates a bad fit, and therefore excluding clusters where the two methods don't agree can provide such a sub-sample of clusters that are more accurately reconstructed. Requiring the difference between the estimates from the two methods to be less than 110 μm, a sub-sample consisting of 22% of the clusters was selected, and in this sample a position resolution of 22 μm was obtained.

By resampling the MC data the statistical uncertainty is found to be only ±0.5 μm. The achieved position resolution might also be subject to systematic errors caused by the simulation not fully reproducing experimental data. Assuming that this manifest itself in different spectra of annihilation products it is relevant to check how a a change in annihilation products affects the position resolution. Therefore the simulation and vertex reconstruction was also run with annihilations in carbon and calcium, as this respectively gives a higher and lower ratio of pions to nuclear fragments. The resulting position resolution is 21.3 μm for annihilation in carbon and 21.8 μm for annihilation in calcium. This gives an indication that systematic effects do not influence the position resolution to a large extent.

An absolute requirement for the position resolution is to be below the proposed 60 μm periodicity of the moiré deflectometer, and this requirement is met. Simulation studies have shown that a resolution of 10–13 μm is required to measure the gravitation acceleration with a precision of ±1%. Even though this requirement is not met, the achieved position resolution should be good enough to perform a proof of principle measurement where a shift in the fringe pattern is observed [1].

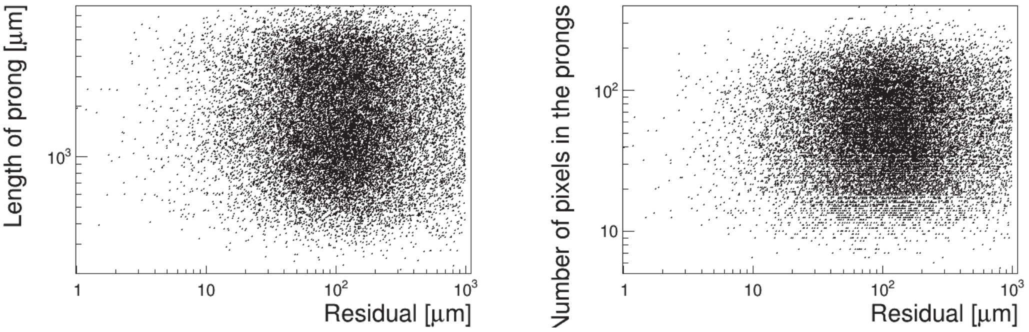

(a) Correlation between the length of the prongs and the residual. Correlation coefficient is −0.007.

(b) Correlation between the number of pixels in the prongs and the residual. Correlation coefficient is −0.015.

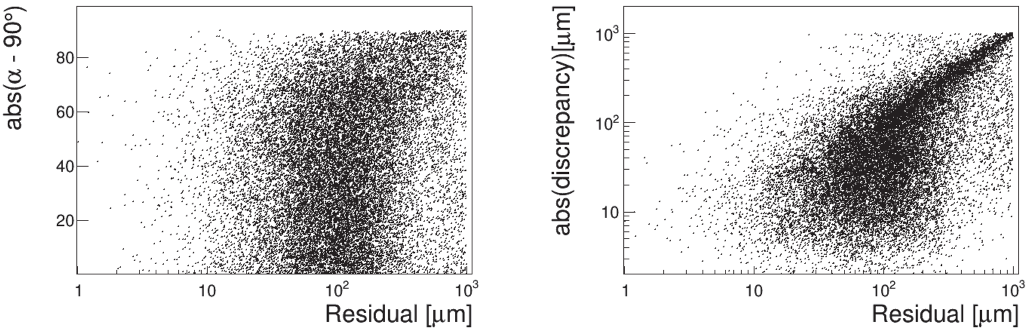

(c) Correlation between the angle between the prongs and the residual. Correlation coefficient is 0.23.

(d) Correlation of the discrepancy between the two methods and the residual. Correlation coefficient is 0.64.

Figure 14. Plots showing the correlation between prong parameters and the accuracy of the fit.

7 Conclusions

This work presents a detailed study of the annihilation of antiprotons with clear prongs in a thick Timepix3 detector. A full detector response model based on FLUKA was developed. The model was verified by comparison with experimental data, and it reproduces the geometrical variables such as cluster size and number of prongs quite well. An algorithm for characterizing and tagging the antiproton clusters was also developed. Applying this algorithm, a tagging efficiency of 50 ± 10% is estimated with cuts of at least 70 pixels and at least 1 prong, while the false tagging rate is 1% with the same cuts.

The detector response model was also used to investigate the possibility of reconstructing the annihilation point from linear fits to the prongs. With low flux, and thus few suppressed pixels, this proved to be possible for 22% of the clusters, and a vertical position resolution of 22 ± 0.5 μm was obtained. AEgIS expects to measure a vertical fall of $\approx 20\,\mu$m over the length of 1 m, given that the antihydrogen beam has a velocity of less than 500 m/s. The position resolution obtained here is low enough for such a fall to be observed.

Acknowledgments

This project was financed by the Research Council of Norway through the FRINATEK and CERN related research project. We thank the Medipix Collaboration for providing their detector at our disposal for the duration of the tests, as well as for their help and support during this work. This work was supported by the European Research Council, the European Social Fund, the Istituto Nazionale di Fisica Nucleare, the Austrian Ministry for Science, Research and Economy, the German Research Foundation, the Research Council of Norway, the Bergen Research Foundation, the Russian Ministry of Education and Science, the Russian Academy of Sciences and the John Templeton Foundation. This research project has been supported by a Marie Skłodowska-Curie Innovative Training Network Fellowship of the European Commission's Horizon 2020 Programme under contract number 721559 AVA and from the European Union's Horizon 2020 research and innovation programme under the Marie Sklodowska-Curie grant agreement ANGRAM No 748826.

References

[1] G. Drobychev et al., *Proposal for the AEGIS experiment at the CERN antiproton decelerator (Antimatter Experiment: Gravity, Interferometry, Spectroscopy)*, CERN-SPSC-2007-017 (2007).

[2] AEGIS collaboration, *Exploring the WEP with a pulsed cold beam of antihydrogen*, *Class. Quant. Grav.* **29** (2012) 184009.

[3] S. Aghion et al., *A moiré deflectometer for antimatter*, *Nature Commun.* **5** (2014) 4538.

[4] M.K. Oberthaler, S. Bernet, E.M. Rasel, J. Schmiedmayer and A. Zeilinger, *Inertial sensing with classical atomic beams*, *Phys. Rev.* **A 54** (1996) 3165.

[5] AEGIS Proto collaboration, *Proposed antimatter gravity measurement with an antihydrogen beam*, *Nucl. Instrum. Meth.* **B 266** (2008) 351.

[6] M. Kimura et al., *Development of nuclear emulsions with 1 μm spatial resolution for the AEgIS experiment*, *Nucl. Instrum. Meth.* **A 732** (2013) 325.

[7] A. Gligorova et al., *Comparison of Planar and 3D Silicon Pixel Sensors Used for Detection of Low Energy Antiprotons*, *IEEE Trans. Nucl. Sci.* **61** (2014) 3747.

[8] T. Poikela et al., *Timepix3: a 65k channel hybrid pixel readout chip with simultaneous toa/tot and sparse readout*, 2014 *JINST* **9** C05013.

[9] N. Pacifico et al., *Direct detection of antiprotons with the timepix3 in a new electrostatic selection beamline*, *Nucl. Instrum. Meth.* **A 03** (2016) 12.

[10] P. Beloshitsky, T. Eriksson and S. Maury, *The CERN antiproton decelerator (AD) in 2002: Status, progress and machine development results*, *Nucl. Instrum. Meth.* **B 214** (2004) 176.

[11] G. Bendiscioli and D. Kharzeev, *Anti-nucleon nucleon and anti-nucleon nucleus interaction: A review of experimental data*, *Riv. Nuovo Cim.* **17N6** (1994) 1.

[12] S. Aghion et al., *Measurement of antiproton annihilation on Cu, Ag and Au with emulsion films*, 2017 *JINST* **12** P04021 [`arXiv:1701.06306`].

[13] T.T. Böhlen, F. Cerutti, M.P.W. Chin, A. Fassò, A. Ferrari, P.G. Ortega et al., *The FLUKA Code: Developments and Challenges for High Energy and Medical Applications*, *Nucl. Data Sheets* **120** (2014) 211.

[14] L. Tlustos, private communication (2017).

[15] C. Granja, J. Jakubek, U. Köster, M. Platkevic and S. Pospisil, *Response of the pixel detector timepix to heavy ions*, *Nucl. Instrum. Meth.* **A 633** (2011) S198.

[16] T.E.J. Campbell-Ricketts, M. Kroupa and L.S. Pinsky, *Spectroscopy of high-energy ions with timepix3*, 2016 *JINST* **11** P11007.

[17] J.S. Coursey, M.A. Zucker, M.J. Berger and J. Chang, *Estar pstar and astar: Computer programs for calculating stopping-power and range tables for electrons, protons, and helium ions*, (2005).

[18] N. Stoffle, L. Pinsky, S. Hoang, J. Idarraga, M. Kroupa, J. Jakubek et al., *Initial results on charge and velocity discrimination for heavy ions using silicon-Timepix detectors*, 2012 *JINST* **7** C12009.

[19] L. Pinsky, *Summary of medipix technology's 3-years in space and plans for future developments*, at *The 14th Vienna Converence on Instrumentation*, Vienna Austria (2016).

[20] R.O. Duda and P.E. Hart, *Use of the hough transformation to detect lines and curves in pictures*, *Commun. ACM* **15** (1972) 11.

[21] L. Rossi, P. Fischer, T. Rohe and N. Wermes, *Pixel Detectors: From Fundamentals to Applications*, Springer, Heidelberg Germany (2006).

[22] G. Lutz, *Semiconductor radiation detectors*, Springer, Heidelberg Germany (1999).

[23] K. Sjobak, *Full simulation of a testbeam experiment including modeling of the Bonn Atlas Telescope and Atlas 3D pixel silicon sensors*, MSc. Thesis, University of Oslo, Oslo Norway (2010).

[24] P.A. Tove and W. Seibt, *Plasma effects in semiconductor detectors*, *Nucl. Instrum. Meth.* **51** (1967) 261.

[25] https://www.synopsys.com/silicon/tcad.html, (2017).

[26] C.H. Wang, K. Misiakos and A. Neugroschel, *Minority-carrier transport parameters in n-type silicon*, *IEEE Trans. Electron Dev.* **37** (1990) 1314.